ALMA MATER STUDIORUM – UNIVERSITÀ DI BOLOGNA

DOTTORATO DI RICERCA IN INGEGNERIA ELETTRONICA,
TELECOMUNICAZIONI E TECNOLOGIE
DELL'INFORMAZIONE

Ciclo XXXIII

Settore Concorsuale: 09/F1 Campi Elettromagnetici

Settore Scientifico Disciplinare: ING-INF/02 Campi Elettromagnetici

---

ANTENNAS AND PROPAGATION FOR UAV-ASSISTED WIRELESS NETWORKS TOWARDS NEXT GENERATION MOBILE SYSTEMS

Presentato da:
Ing. Maximilian James ARPAIO

Coordinatore Dottorato
Prof.ssa Alessandra COSTANZO

Supervisore
Prof. Diego MASOTTI

Co-Supervisore
Prof. Franco FUSCHINI

Esame finale anno 2021

"…rari nantes in gurgite vasto…"

Virgilio, Eneide (I, 118)

CANDIDATE'S DECLARATIONS

In full accordance with the Statute of the *Alma Mater Studiorum*, University of Bologna, I hereby certify that the research activities carried out in the frame of my PhD carrier are in no way connected to any military project and what I have studied and learnt during these three years has not been used for any military-related purpose.

Bologna, December 2020

ACKNOWLEDGMENTS

Three years ago, I decided to challenge myself.

Close to my 40s, with nearly 15 years of industrial experience behind, a full-time job and a wonderful family to take care of, I decided to apply for a PhD course in Bologna. There are many - very personal - reasons behind this "unusual" decision but there is not a single day I regret about. Despite the many difficulties and the tiredness along the way, I have never given up. So, the very first thank-you goes to ME … I am really proud of myself! I really hope my daughters can understand the importance of being curios, of school education, passions, and self-belief at any time of their lives.

Working on my research project for three years has been a real pleasure for me but at the same time it has been a period of stress and of huge personal and family sacrifices, made it even more difficult by the ongoing pandemic disease. It is no joke I have learned a lot and I had the opportunity to deepen a subject I care about while investing in myself. I honestly cannot imagine a better way to spend my personal time out of the office (aside being with my family, of course!) while learning something new and stimulating. It was a fantastic experience, for which I believe my greatest luck has been to have not only great supervisors (Diego and Franco) but an awesome team of professors and researchers at DEI (Enrico, Vittorio, Marina, Roberto, Chiara, Alessandra) that have truly welcomed me in their Department. Besides their brilliant minds and highest knowledge of all the many and different engineering aspects, I have always really enjoyed our open discussions, their critical spirit as well as their availability and flexibility anytime I was in need... I have learned a lot from them, and I will be forever grateful.

My appreciation goes also to my laboratory mates: Giacomo, Francesca, Mazen and Silvia with whom I spent nice moments and I had a lot of fun.

Finally, I wish to express my gratitude to NVIDIA Corporation for the given trust in my research activity and for the donation of the Titan Xp GPU which has been used in many parts of the simulations and research activities. With no grant to cover University taxes, transportation, material, books and all the different administrative and travel expenses, I cannot deny that this gift has been more than welcome.

I wish you all a good reading,

UNIVERSITA' DI BOLOGNA

ABSTRACT

School of Engineering and Architecture
"G. Marconi" - DEI

Dottorato di Ricerca

ANTENNAS AND PROPAGATION FOR UAV-ASSISTED WIRELESS NETWORKS TOWARDS NEXT GENERATION MOBILE SYSTEMS

Ing. Maximilian James ARPAIO

Unmanned Aerial Vehicles (UAV), also known as "drones", are attracting increasing attention as enablers for many technical applications and services, and this trend is likely to continue in the near future. UAVs are expected to be used extensively in civil and military applications where aerial surveillance and assistance in emergency situations are key factors. When compared to conventional terrestrial communications, UAVs can be more useful and flexible in reaction to specific events, like natural disasters and terrorist attacks since they are faster to deploy, easier to reconfigure and assumed to have better communication means due to their improved position in the sky, improved visibility over ground, and reduced hindrance for propagation. In this regard, UAV enabled communications emerge as one of the most promising solutions for setting-up the next-generation mobile networks, with a special focus on the extension of coverage and capacity of mobile radio networks for 5G applications and beyond. However, air-to-ground (A2G) propagation conditions are likely to be different and more challenging than those experienced by traditional piloted aircraft, where ground sites are in open areas with tall antenna towers. For this reason, knowledge of this specific propagation channel – together with the UAV antenna design and placement - is paramount for defining an efficient communication system and for evaluating its performance.

This PhD thesis tackles this challenge, and it aims at further investigating the narrowband properties of the air-to-ground propagation channel by means of GPU accelerated ray launching simulations for 5G communications and beyond. The reader is thus guided through the electromagnetic design of an antenna solution capable of covering both UAV-to-ground and UAV-to-UAV communications, while looking for agile architectures and light materials.

To support the investigations of A2G links, line of sight probability and path loss exponent– together with its sigma shadowing – are evaluated and calculated. Results and outcomes are provided for different UAV heights and in different dense urban scenarios, taking into account different 5G frequencies and types of antennas on board of the UAV.

Thanks to the flexibility of the GPU accelerated ray launching simulations, it is possible to focus on the different multipath components of the propagated signal, which give thus a new insight on the subject by breaking down its subcomponents. The speed-up achieved by the use of GPU acceleration cards is also considered in the analysis as part of this thesis, thanks to which different improvements have been evaluated by comparing professional GPU cards (Tesla series) and gaming ones (GTX series). This PhD thesis also touches possible applications in the creation of Radio Environment Maps (REMs) in the frame of trajectory optimisation and through the in-field measurements to validate data.

As a conclusion, this PhD thesis might bring deep insights into the air-to-ground channel characteristics and UAV antenna design, which can be helpful for designing UAV communication networks and evaluating or optimising their performances in a fast and reliable manner, with no need for exhausting – multiple - in-field measurement campaigns.

LIST OF ABBREVIATIONS

A2G	Air to Ground
BS	Base Station
CS	Channel Sounder
EIRP	Equivalent Isotropically Radiated Power
ER	Effective Roughness
FDTD	Finite Difference Time Domain
GTD	Geometrical Theory of Diffraction
GTP	Geometrical Theory of Propagation
HPBW	Half-Power-Beam-Width
LOS	Line-of-Sight
MIMO	Multiple-Input-Multiple-Output
NLOS	Non-LOS
PEP	Power Elevation Profiles
RCS	Radar Cross Section
RF	Radio-frequency
RL	Ray-Launching
RR	Radio Resource
RT	Ray-Tracing
RX	Receiver
TX	Transmitter
UAV	Unmanned Aerial Vehicle
UE	User Equipment
UTD	Uniform Theory of Diffraction
UWB	Ultra Wide Band
VNA	Vector Network Analyzer

INDEX

LIST OF FIGURES

LIST OF TABLES

PREFACE

The main purpose of this dissertation is to investigate the Air-to-Ground (A2G) channel for next generation mobile systems, starting from antennas and moving to propagation related matters. The novel access to portions of the spectrum (e.g. 26GHz or 70GHz) – together with traditional ones (like 700MHz or 3500MHz, coming from the previous UHF television and WiMAX generations) - is triggering the research community worldwide and different applications are driving a revolutionary progress in the telecommunications field by opening many opportunities, but raising at the same time new challenges. In particular, the properties of the A2G still need to be deeply investigated, especially for modern solutions relaying on UAV-Assisted wireless networks.

With the aim to give this thesis a logical progression, chapters have been organized as follow:

- Chapter (1) provides a simple introduction to UAV and motives the reasons behind this research activity.
- Chapter (2) outlines the antenna design, both as a single element and as an array.
- Chapter (3) focuses on the Ray Launching (RL) tool and its computation performances.
- Chapter (4) describes the narrowband study, including the loss probability, the path loss exponent, and the sigma shadowing. This Chapter also includes a deep analysis of the multipath components of the propagated signal. In particular it shows the weight of reflections, diffraction, direct rays, diffuse scattering and a combination of them out of the signal.
- Chapter (5) briefly addresses the use of REMs in trajectory optimisation, as a good application of the ray launching tool in the frame of a joint research cooperation.

- Chapter (6) shares the preliminary outcomes of the first in-field measurements carried out with a drone in a real urban environment.
- Chapter (7) draws the main conclusions and possible future works.
- Appendix includes extra simulations and results that integrate the elements provided in Chapter (4).

CHAPTER 1. INTRODUCTION

Initially conceived to strictly satisfy military needs, the Remotely Piloted Aircraft Systems (RPAS) - as defined by the International Organization of Civil Aviation (ICAO) and which assumes that the system is somehow always operated by somebody on the ground - have shown in recent years great flexibility of use and are also becoming valid tools in the civil field to meet the most varied operational requirements. The RPAS puts emphasis on the fact that the aerial system includes not only the flying vehicle but also, for example, a ground control station, data link, and antenna. In common life, it is however easier to refer to RPAS as “drones” or “UAV” (Unmanned Aerial Vehicle), as many documents, papers and books are now addressing them.

In fact, in recent years there has been a growing interest in the use of such systems – with different material available in the market and on the internet - and if this trend continues, it could open up in the future new scenarios and enhancements in civil-commercial applications, as well as in the safety and optimization of many civil aviation activities [1].

According to different business research results in 2017 the sales of UAVs will surpass 1.2 billion USD per year by 2021, which shows an annual growth rate of 7.6% from values of 2016 [2]. Deliveries of commercial drone are expected to reach 805.000 in 2021, at the growth rate of 51%. The global UAV market value (including military ones) is expected to reach 3 billion USD by 2027. From a payload perspective it is interesting to note that radar and communication equipment dominate the global UAV market (with a market share close to 80%), followed by the camera and sensor segments with around 11% share [3].

These growth figures need to be slightly revised in the following months since COVID-19 has already reshaped the ways of many businesses, but the fallout and ramifications of the pandemic that brought the global economy to a standstill are just beginning to be felt. More changes are imminent, and the drone industry will see and feel them over the coming months and years [4]. Whether in positive or negative manners, this is still not known and difficult to predict.

Decades of use in military aviation has also contributed to the improvement of their applications in the civil field. As a matter of fact, in the recent years, aviation authorities around the world have been making big progress towards integrating UAVs into their national airspaces. At the same time, private industries have been developing innovative UAV-based applications, such as drone-based package delivery, medicine delivery, pipeline monitoring systems, and disaster-area aerial surveys. However, before UAVs can become integrated into the civilian airspace - and such real-world applications become reality - there are several technical, societal, and regulatory challenges that need to be addressed by the research community.

On the one hand, the safe and definitive insertion of such systems in regulated airspace will be a long-term activity for ICAO; on the other hand, UAVs have already received within the scientific community a remarkable success for the potential applications that can be outlined and for the variety of technical problems that are already being addressed.

1.1. UAV TYPES AND PURPOSES

Many authors have already proposed various classifications for the different kinds of UAVs. One may classify UAVs by vehicle types, sizes, mass, mission range, altitude, endurance, etc. Each kind of classification is a way to point out a particular feature, but it hides another important aspect of UAV. Most lectures given on UAV start with a classification of UAVs based on some sort of conventional typology. The main drawback of such descriptions is that they are basically based on existing systems and such classification does not provide a comprehensive outlook of the various choices as applied to missions and vehicle configurations. Furthermore, it makes it very difficult to anticipate

future UAV since it is based on the existing UAV market segmentation. A more appropriate way to classify the different kinds of possible UAV would be to combine typical mission profiles and the major vehicle configurations [5].

Beside the limitation or complexity of any model, rotary-wing UAVs have attracted a good deal of attention from the scientific community. According to recent figures, among the 3000 to 4000 UAVs flying in France and currently registered by the French authorities, about 80% are rotorcraft, that is multi-rotors. A first reason for this attention is related to the fact that rotary-wing configurations provide the capability of hovering, which is essential to guarantee clear identification and specific mission critical activities. Hovering is also a way to easily take off and land without a complex procedure, such as a prepared airfield or a specific landing device. Furthermore, multi-rotors are easy to fabricate and fairly straightforward to fly and this is the reason to consider them as the baseline for the UAV activities in this dissertation.

As quad-rotors were almost the only multi-rotors available 10 years ago (Figure 1-1), more recent multi-rotor aircraft now include hexa-rotors, octo-rotors, and various combinations of coaxial multi-rotors. Increasing the number of rotors is generally considered to be a good way to enhance security since if a motor fails, the other motors can immediately compensate.

Figure 1-1: Example of a quad-rotors UAV (Aeryon Scout model, courtesy of © Aeryon)

1.2. RESEARCH ACTIVITIES AND MOTIVATIONS

Among the many and different applications – ranging from public safety surveillance and law enforcement actions to precision agriculture or search and rescue operations [6-7], many of them quite challenging [8] - the concept of one or more UAVs operating as aerial Base Stations (BSs) or flying relays (Figure 1-2) has recently received great attention in the framework of 5G systems [9-14] to expand wireless connectivity to unserved areas and/or to increase capacity in busy areas, or even to back up a damaged ground network in emergency situations for different frequencies, focusing on those assigned within the European Community (Figure 1-3).

Figure 1-2: Aerial communication platform can be deployed for several purposes including enhancement of ground network capacity.

It is understandable that the key to develop the UAV market is associated to UAVs technology and applications. This technology should be capable of satisfying the current and future requirements and create new applications. This approach is even more stressed by the need for more cost effective and flexible UAVs in the future.

The quite short flight time, up to few tens of minutes in most cases, is possibly the major drawback of this idea, in spite of the on-going advances in battery technology and

charging techniques [15]. Besides, concerns with public safety still exist and thus the deployment of flying UAV swarms for whatever commercial applications must often come to terms with strict limitations enforced by local regulations [16].

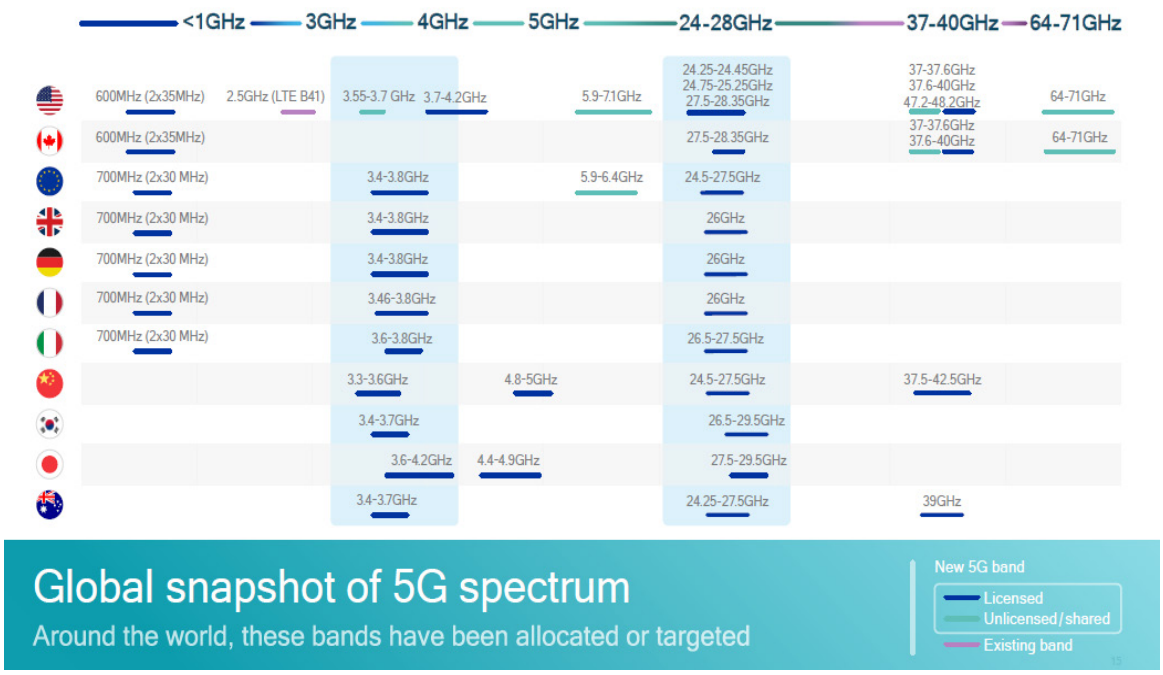

Figure 1-3: Spectrum allocated worldwide for 5G applications (courtesy of © Qualcomm)

In order to tackle these manifold issues, UAV–aided communication networks require careful and thorough design, in order to optimally set the number and the routes of the simultaneously flying BSs. To this aim, some awareness about the A2G propagation channel – together with the design of choice of the on-board antenna system - is necessary, as it may contribute to optimise the data-link and to plan the flying paths / hovering locations where the UAVs can provide the most helpful wireless access to users at street level and/or indoor.

In fact, the emerging 5G technology is demanding antennas with features and materials previously unseen on a user terminal. These requirements raise numerous design challenges in order to achieve a reasonable trade-off between technological design issues and commercial criteria - low cost, small size, light weight, radiation efficiency, antenna gain, broadband performance, and so on – at microwave as well as at millimetre wave

bands. The antennas used in UAV should be low profile, compact and directional. With the increase in data rates and a trend of miniature electronic circuits for wireless digital applications, the antennas required for these applications should be also easily mountable and have a broad bandwidth.

In urban environments, as the UAVs may well stand out against the building layer, the A2G channel may benefit from a better line of sight (LOS) occurrence compared to standard cellular networks, where the antenna visibility is instead more easily prevented even in case the terrestrial BSs are placed on tall buildings or high masts. At the same time, LOS conditions cannot be counted on always and everywhere, and multipath propagation might therefore still play an important role. This is especially true in urban environments, where infrastructural elements like buildings, bridges, overpass roads and other manmade and natural clutters can heavily affect electromagnetic signals propagation.

In [17], the authors studied several state-of-the-art path loss models applicable in the urban scenario – especially in emergency communication systems - and compared their performances. In [18], the authors extracted the main parameters of path loss model in urban environment and propose a simplified Saleh-Valenzuela (SV) model with specific parameters that describe the stochastic properties of the arrival delays and amplitudes of resolvable multipath components (MPCs) in wireless transmission systems. In [19], the researchers studied the propagation characteristics of air-to-air channels in a virtual urban scenario generated with the ITU-R model.

Although the different research activities on the subject, the reader should bear in mind that measurements campaigns for the characterization of the A2G channel represent a rather challenging task, as they undergo the aforesaid limitations about the payload UAVs can rise, the battery lifetime and the permission to fly, in addition to the common shortcomings of the experimental approach, i.e. expensive equipment and long execution time.

For these reasons, dense urban scenarios have not been primarily targeted in previous studies, and A2G propagation measurements have been mainly carried out in

rural/suburban environments, and often limited to few and quite short flying paths in clear visibility conditions to the pilot [20-22].

Because of such hindrances to extensive measurement campaigns, established path loss empirical models, often consisting of best-fit lines of the measured attenuations vs. link distance, seem also lacking, at least for the dense urban case. As a rule of a thumb, there is a trend to rely on on-the-shelf propagation models, like the simple free-space or two-ray formulas [17][23]. Nevertheless, they cannot be reliable when multipath components (besides the ground reflection) are significant. Similarly, empirical/statistical propagation models for terrestrial cellular networks (like the Okumura-Hata model [24-27] and the many "Hata-like" models) may fit the air-to-ground scenario to a limited extent, as their reliability is likely to be doubtful when the drone flight level is remarkably higher than the buildings level [28]. In conclusion, empirical/statistical models specifically conceived for the A2G channel can be hardly found in the open literature [29] and this dissertation aims at bringing innovative insights to a broader extent.

Deterministic propagation tools, either Ray Launching (RL) or Ray Tracing (RT), may represent an effective solution for A2G channel assessment. The reason is twofold: as they are inherently site specific, they can replace measurements to some extent, i.e. ray-based simulations might be run over large urban areas thus providing a large data set suitable for statistical analysis and/or the development of empirical A2G path loss models through well-known fitting procedures. Furthermore, the ray approach can provide a significant insight into the A2G propagation process, e.g. about LOS/NLOS probability or the composition of the major multipath contributions at different flight levels and/or different communication frequencies. Unfortunately, running RT/RL simulations often involves a fairly high computational effort, which turns out particularly heavy in the A2G urban scenario, as the drone might be in clear visibility with a multitude of buildings underneath, and therefore a very large number of propagation paths might be present. In order to limit the computational burden, ray-based investigation of A2G propagation has been often limited to restricted areas with few ground locations, thus downgrading the actual effect of the propagation analysis [30].

In this thesis, narrowband characterization of the A2G channel in urban environment is carried out by means of a RL model specifically conceived for fast coverage assessment over large areas [31]. With respect to previously published studies [32-34], the analysis carried out during the research period is here extended over three different urban scenarios, taking into account a broad range of altitudes and with communication frequencies spanning up to the millimetre-wave band. Besides path loss and shadowing, attention is here devoted to the role played by the different electromagnetic interactions which might take place, namely direct rays, reflection, diffraction and diffuse scattering, when multipath occurs in the A2G channel. In fact, when the ray concept is valid, it is possible to describe the electromagnetic wave propagation using several mechanisms [35].

It is not in the scope of this dissertation to provide a thorough mathematical description of propagation phenomena, but for simplicity, the reader can imagine a point source from which many rays are emanating. Considering one of the rays - and based on the behaviour of this ray – it is often classified as falling within one of the following types:

- ✓ *Direct Rays or Line of Sight propagation*: it happens when the ray goes directly from the source to the field point, i.e. rays travel in a direct path from the source to the receiver with no interactions along its way. This is often referred to line of sight (LoS) propagation mechanism.
- ✓ *Reflection*: it happens when the ray changes direction of its wavefront at a flat, smooth, interface between two different homogeneous media and thus it bounces one or more times before reaching the field point, i.e. rays travel no longer in a direct path from the source to the receiver but hit a surface along their way and are reflected. The propagation direction of a reflected ray follows the law of reflection, while the magnitude of the reflected field is determined by Fresnel's equations for different polarizations.
- ✓ *Diffraction*: This phenomenon happens when a wave encounters either an edge or a curved surface with a curvature much larger than the wavelength - or openings much smaller than it. It is defined as the bending of waves around the corners of

an obstacle into the region of geometrical shadow of the same obstacle. Diffracted rays are more complex to describe when compared to the previous two types of rays: one incident ray can give raise to many diffracted rays into a continuum cone of rays for diffraction from a wedge.

- ✓ *Scattering*: Like previous phenomena, it happens when rays are forced to deviate from a straight trajectory by surface roughness and/or volume non-uniformities in the medium through which they pass. In conventional use, this also includes deviation from the angle predicted by the law of reflection.

CHAPTER 2. LIGHTWEIGHT MICROSTRIP PATCH AND ARRAY

This chapter introduces the UAV antenna design, carried out at the beginning of the research activity. To this end, section 2.1 first provides an overview of the motivations and constraints. Then section 2.2 describes the design steps to achieve first a single element and then an array of four elements. Section 2.3 further extends the antenna design by considering the effects of body curvature when the antenna is possibly installed on a non-planar fuselage, below the UAV body or a rotor arm. Finally, section 2.4 draws some conclusions and provides some baselines assumptions used in the following chapters.

2.1. UAV AND ANTENNAS

The use of antennas embedded within the UAV has several advantages such as reducing drag, enhancing the aerodynamic profile of the UAV and boosting the communication link performance while minimising the hindrance of other parts of the fuselage. The microstrip antenna has the advantages of low cost, space-saving, and easier manufacturing. However, the design of standard microstrip antennas cannot meet the requirements of modern 5G networks – especially in terms of bandwidth - and thus specific and innovative designs must be investigated [36] [37]. During this research activity, microstrip patch antennas and arrays already proved to be excellent candidates to meet these requirements and to achieve a proper balance between performances and manufacturing complexity for 5G applications.

In the next sections it is introduced the design of a broadband antenna with a relative bandwidth of more than 10%, that can be specifically used for UAV applications over 5G networks [38]. Specifically, attention was focused on a single element and 2×2 rectangular array antennas, by aiming the research at proper materials selection: the usage of soft, light, and flexible materials leads to versatile radiating solutions, suitable to be hosted on a drone. Both antennas are centred at 3.6 GHz, which emphasises their use in the lower end of the allocated 5G spectrum (C-band).

2.2. ANTENNA DESIGN AND SIMULATION

CST Studio Suite® is a powerful and easy-to-use electromagnetic field simulation commercial software which combines a user-friendly interface with remarkable simulation performances. CST Studio Suite contains a large variety of solvers for carrying out high frequency simulations which are then all grouped as a specific High Frequency Module, also known as CST Microwave Studio®. This software simplifies the process of creating the structure by providing a powerful graphical solid modelling front end which is based on the ACIS modelling kernel. After the model has been constructed, a fully automatic meshing procedure is applied before a simulation engine is started. An advanced visualization engine and flexible post-processing allow the user to analyse and improve the design in a relevant and efficient way. Since no one method works equally well for all applications, the software contains several different simulation techniques (time domain solvers, frequency domain solvers, integral equation solver, multilayer solver, asymptotic solver, and eigenmode solver) to best suit various applications. In the frame of this research activity, mainly the time domain (TD) and the frequency domain (FD) solvers were used.

There are various important steps in designing microstrip antennas, but the most important one is the choice of the right substrate. In the frame of the research activity, a thick, low-dielectric constant layer of substrate was used to achieve a wide bandwidth and high radiation efficiency. Rogers RO4350B was first chosen for simulation purposes, and then the design criteria moved to RT Duroid 5880 for its softer mechanical properties and

its common availability on the market for fabrication. Microstrip antennas are well known to have very narrow impedance bandwidth, typically a few percent. To overcome this aspect, the design was based on a parasitic patch placed above the radiating element and spaced by a specific distance, chosen via different simulation runs, to optimise both the gain and the bandwidth.

First the single element antenna was designed as reported in section 2.2.1. The space between the radiating patch and the parasitic one was first filled in with vacuum and then with a particular and innovative foam which would have provided also mechanical support between the two layers as a sandwich gap filler: Rohacell HF series is a closed-cell rigid foam based on *polymethacrylimide* (PMI) chemistry. With its extremely low dielectric constants and particularly favourable transmission properties at high frequencies, Rohacell HF is ideal for use in antenna applications. The same layout was then replicated on a 2x2 array and its performances were evaluated, as reported in section 2.2.2.

Once the substrate was chosen, the dimensions were carefully analysed by means of different electromagnetic simulation runs. In fact, at these frequencies small changes in any dimension can cause a noticeable change in the results e.g., the frequency shifts, impedance mismatching, etc. TABLE 2-1 shows the substrate specifications for the evaluated patch antenna laminates.

TABLE 2-1: SUBSTRATE SPECIFICATIONS FOR LAMINATES, [37] © 2019 IEEE

Substrate	**Rogers, RO4350B**	**Rogers, RT Duroid 5880**
Centre Frequency	3.6 GHz	3.6 GHz
Copper Thickness	0.0347 mm	0.0347 mm
Substrate Height	1.524 mm	1.575 mm
Dielectric Constant	3.48	2.2
Loss Tangent	0.003	0.0009
Density	1.86 g/cm3	2.2 g/cm3

Please note that thicker and low-dielectric constant layers were chosen so as to increase the overall efficiency. Material samples are shown in Figure 2-1 here below.

Figure 2-1: On the left-hand side Rohacell 31HF; on the right-hand side Rogers, RT Duroid 5880

The following TABLE 2-2 shows the substrate specifications for the sandwich filler. This specific substrate was chosen to grant the closer dielectric constant to the one of air while keeping a minimum mechanical support to the layers above and below.

TABLE 2-2: SUBSTRATE SPECIFICATIONS FOR FILLER, [37] © 2019 IEEE

Gap Filler	Rohacell 31HF
Centre Frequency	3.6 GHz
Substrate Height	According to design and model
Dielectric Constant	1.050 – 1.043
Loss Tangent	< 0.0002 – 0.0016
Density	0.032 g/cm3

2.2.1 Design of a Single Element

This section describes the design of a square single element patch antenna with coaxial feed line (SMA connector) and parasitic patch for impedance matching, frequency band

increase and gain improvement. In this layout, the most important design features are the substrate size, patch and parasitic sizes and the gap distance between the two.

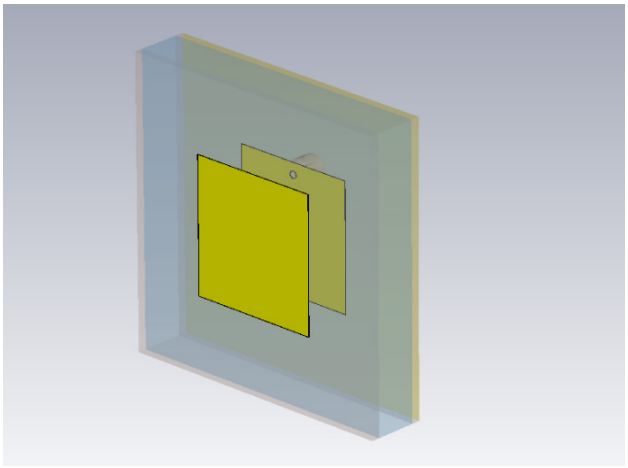

Figure 2-2: Soft transparency, showing parasitic element of the model together with the radiating patch. [37] © 2019 IEEE

These specifications are dependent on each other as well as on the working frequency. Basic microstrip antenna theory equations – as well as latest developments on the antenna substrates - were evaluated [39] and used to calculate the default rectangular patch dimensions L and W on paper. Besides, it should be noted that the effective length $L_{eff} \approx \frac{\lambda_0}{2\sqrt{\varepsilon_{r_{eff}}}}$ - where λ_0 is the wavelength in free space and ε_{reff} is the effective relative dielectric constant - shows a dependency on the multilayer stack-up. These values then formed the input for the CST MWS model, as it can be seen from Figure 2-2. The dimensions and the spacing between the two layers were further optimised via a complete set of TD simulations.

TABLE 2-3: SUBSTRATES LAMINATES AND FILLER FINAL VALUES, [37] © 2019 IEEE

Sandwich	**RO4350B/Vacuum**	**RO4350B/ Rohacell 31HF**	**RT Duroid 5880/ Rohacell 31HF**
Patch side	22 mm	22.1 mm	27.4 mm
Parasitic side	23.5 mm	23.3 mm	26 mm
Gap width	7.4 mm	7.2 mm	6.6 mm
Antenna side	50x50 mm	50x50 mm	50x50 mm

The above TABLE 2-3 summarises the achieved optimum conditions along the transition from the basic configuration to the more complex one: Initial results are in line with expectations for similar patch antennas and previous design experiences.

As a good compromise between electromagnetic performances and mechanical properties, the latest configuration was chosen and kept as a baseline for the investigations, thus fully relying on the pair RT Duroid 5880 substrates and Rohacell 31HF foam one in between. Differently from the two previous solutions, this one shows a parasitic element slightly smaller than the patch underneath.

The following two pictures show the main simulated parameters of the chosen configuration with regards to gain and Half Power Beam Width (HPBW).

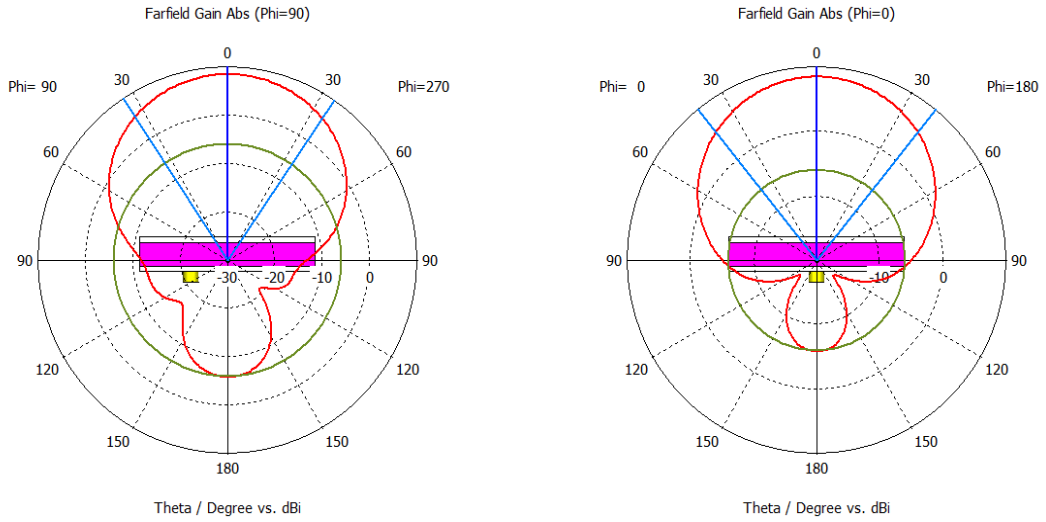

Figure 2-3: On the right-hand side, the radiation diagram in polar coordinates for the H (xz) plane (red curve). On the left-hand side, the same radiation diagram in polar coordinates for the E (yz) plane (red curve). Both H-E planes show a HPBW of nearly 76°. [37] © 2019 IEEE

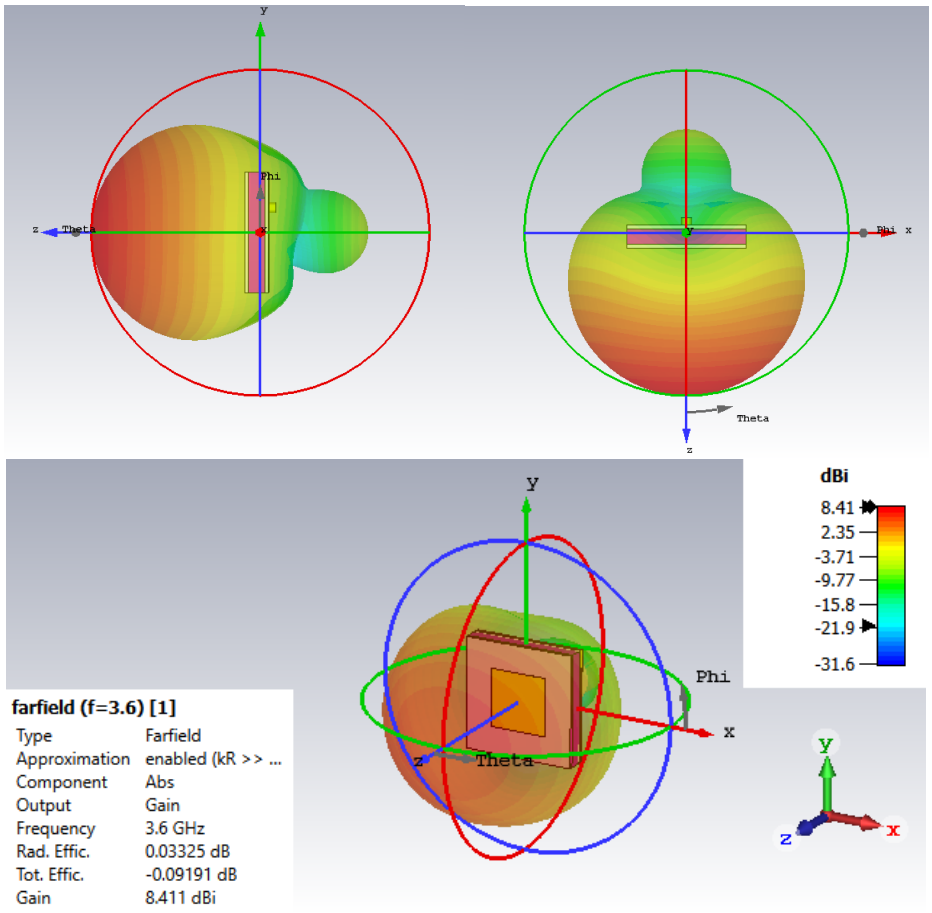

Figure 2-4: The simulated 3D radiation diagram (side, top and perspective views) of the patch antenna at centre frequency.

With regards to gain, Figure 2-5 shows the improvements when the RT Duroid 5880/ Rohacell 31HF configuration is chosen with respect to the other of TABLE 2-3.

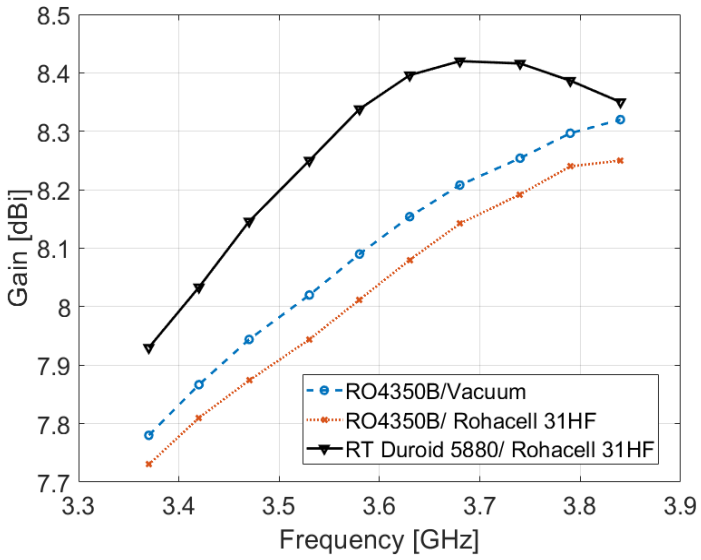

Figure 2-5: Simulated antenna gain, compared to other substrate configurations, [37] © 2019 IEEE

From the simulation results, it is found out that the magnitude of the reflection coefficient S_{11} – simulated for the three configurations of TABLE 2-3 - shows minimum differences among each other with values always better than -15dB over the entire frequency band 3.4-3.8 GHz, as shown in Figure 2-6.

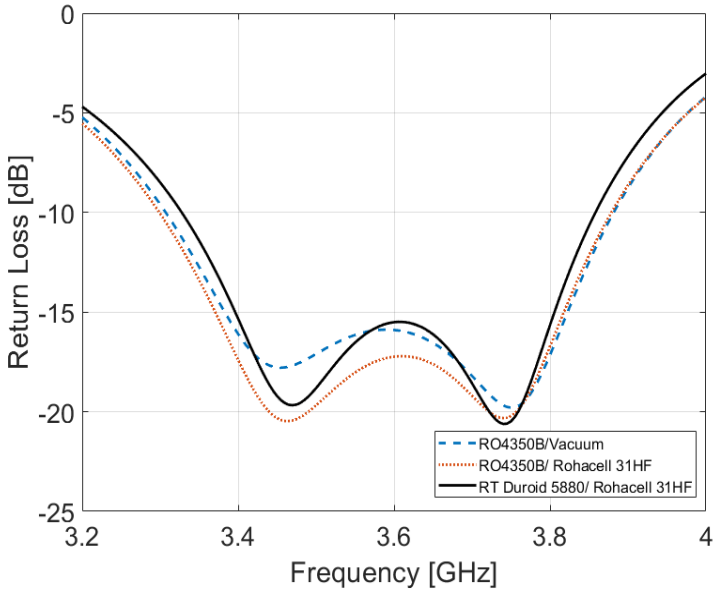

Figure 2-6: Simulated S_{11} parameter, compared to different substrate configurations, [37] © 2019 IEEE

2.2.2 Design of a 2x2 Square Array

After designing a single radiating patch with a parasitic element on top and taking the latest solution as the most convenient one, the same configuration was then replicated on a 2 × 2 array, whose final side resulted to have a length of 100mm, leading to a footprint of 100 cm^2.

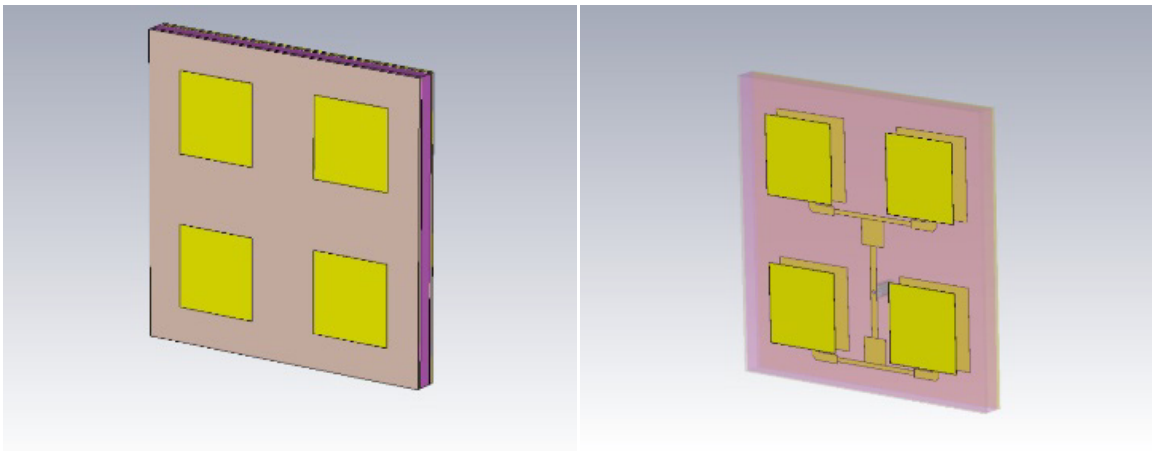

Figure 2-7: On the left-hand side, the 2x2 array is shown. On the right-hand side, by means of a soft transparency, it is possible to see the same parasitic elements together with the radiating patches and the feeding network behind, [37] © 2019 IEEE

In this case, it was not possible to place the coax feeder (SMA connector) directly at the back of each radiating patch, but it was necessary to place first a specific feeding network for impedance matching among the four patches [40] as shown in Figure 2-8.

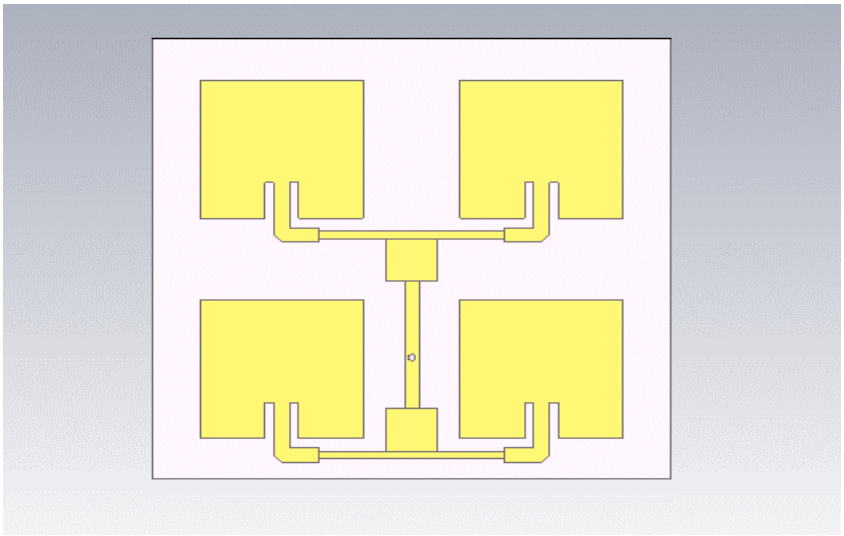

Figure 2-8: Details of the corporate feeding network, [37] © 2019 IEEE

As a matter of fact, during the design phase, it was important to run different simulations in order to evaluate the mutual couplings that occur between antenna elements and the transmission line. It is indeed important to consider them – together with internal reflections among the elements of the array - for better radiation and efficient power transfer since of paramount importance for energy optimisation in any UAV base

communication link. The centre-to-centre distance between the patches was set to slightly less than λ/2 in order to reduce the overall array dimensions as far as practical.

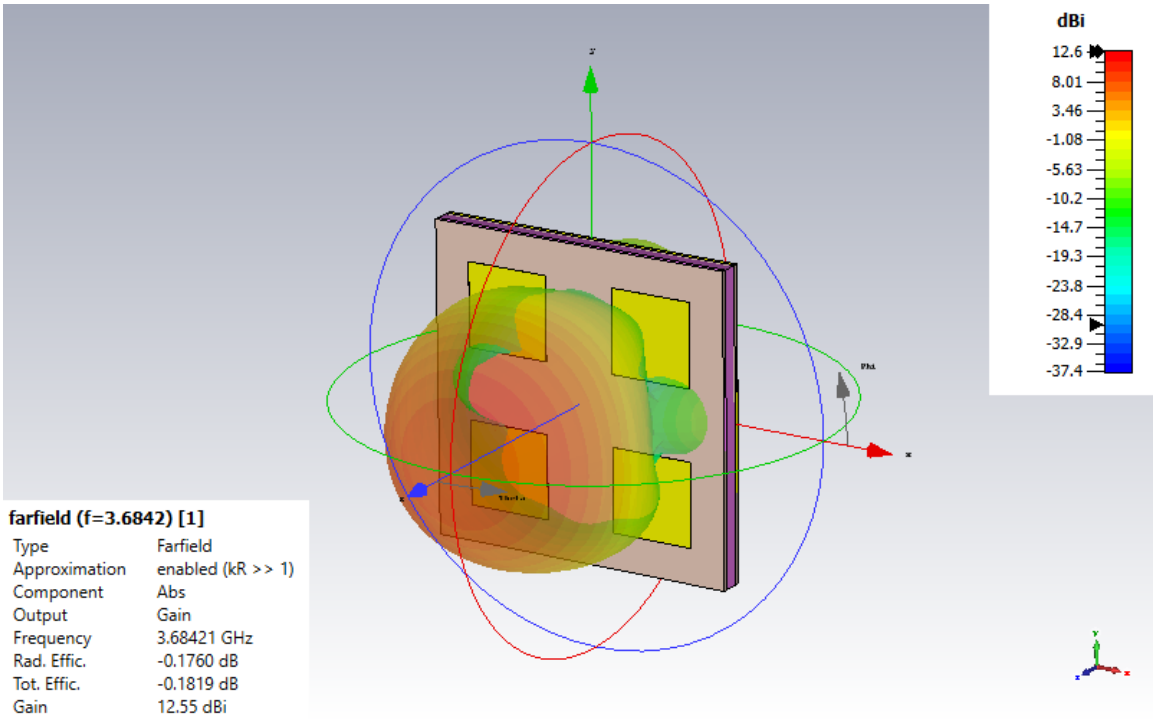

Figure 2-9: The simulated 3D radiation diagram of the 2x2 array at centre frequency, [37] © 2019 IEEE

As it can be seen again in Figure 2-9, a corporate fed system, with lambda-fourth transformer, was used [41], as it was more efficient than single fed arrays in terms of matching and gain, as will be seen in the next pages.

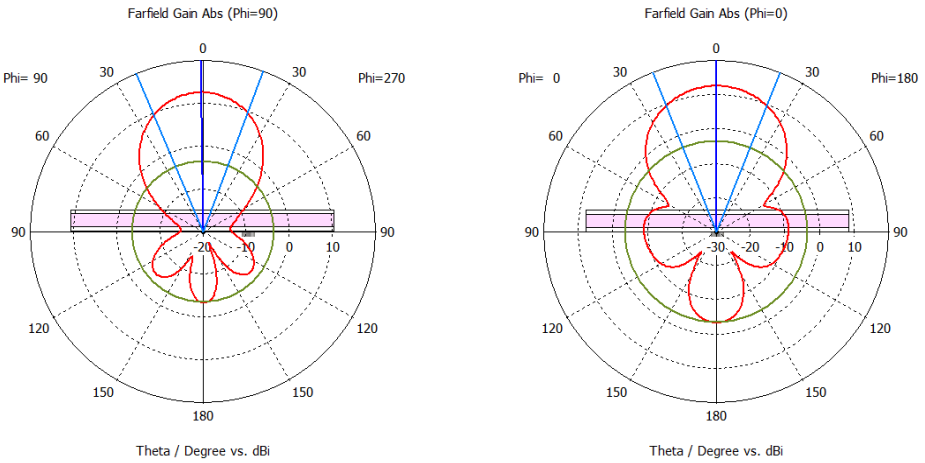

Figure 2-10: On the right-hand side, the radiation diagram of the 2x2 array in polar coordinates for the horizontal plane. On the left-hand side, the same radiation diagram in polar coordinates for the vertical plane. Both H-V planes show a HPBW of nearly 44°, [37] © 2019 IEEE

In the case of no feeding network, feed of each element can be controlled separately which helps in beam steering and scanning as per some 5G network needs, at higher cost expense [42].

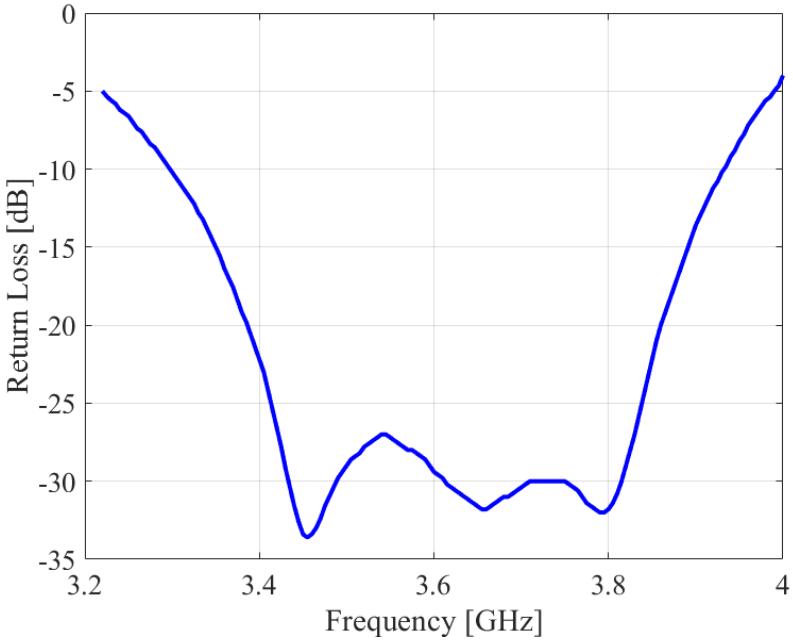

Figure 2-11: Simulated S_{11} for the 2x2 array with RT Duroid 5880/Rohacell 31HF, [37] © 2019 IEEE

From the simulation results, it is found out that the magnitude of the reflection coefficient S_{11} drastically improved with respect to the single antenna case, achieving values always better than -26dB over the entire frequency band 3.4-3.8 GHz, as shown in Figure 2-11.

With regards to antenna gain, Figure 2-12 shows the improvements when the array configuration is chosen with respect to the single element example, reaching an interesting average value of 12dBi. Continuous black curve – including markers – shows the simulated gain, while the overlapped dashed violet curve is the best quadratic fitting curve that further helps to evaluate the trend.

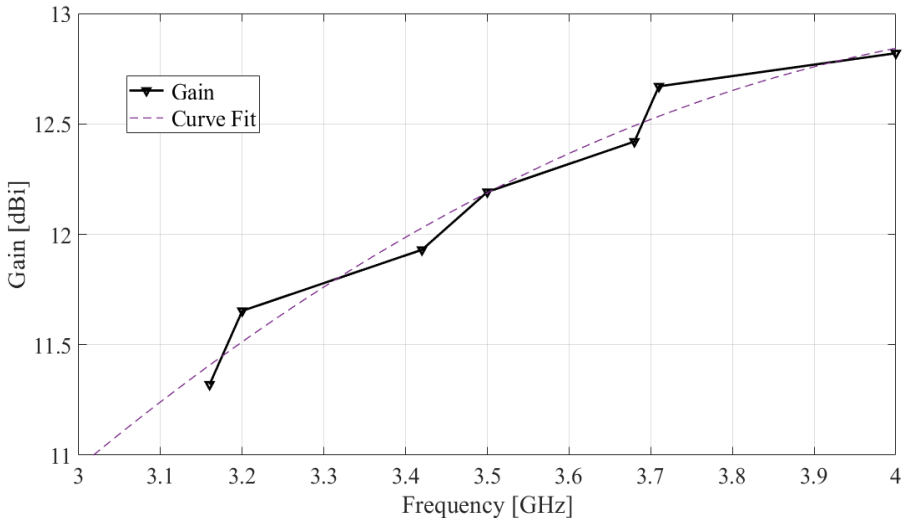

Figure 2-12: Simulated antenna gain for 2x2 array with RT Duroid 5880/Rohacell 31HF

2.3. PERFORMANCES UNDER DIFFERENT BENDING RADIUS

The most difficult challenge for an antenna engineer after designing the antenna is to determine how the antenna behaves when placed on board of a UAV. This is not about the optimum (mechanical) location for installation on the UAV for EM performances, which will be part of future investigations, but how flexible this specific antenna structure can be when fitting the UAV fuselage or wing shape [43]. The following picture shows the same 2x2 array bent around a virtual cylinder along the Y-axis.

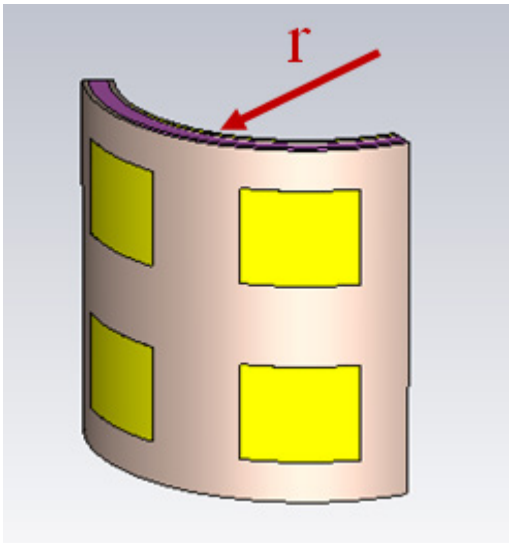

Figure 2-13: Bent 2x2 array around a virtual cylinder with radius 'r', [37] © 2019 IEEE

Next picture shows the different curvatures which the array antenna has been folded around: 25, 50, 200, 350, 500 and 650 mm radius. This time, from the simulation results, it is found out that the curvature radius affects the magnitude of the reflection coefficient S_{11}: of course, the lower the bending value is, the closer the results are to those of a flat antenna array.

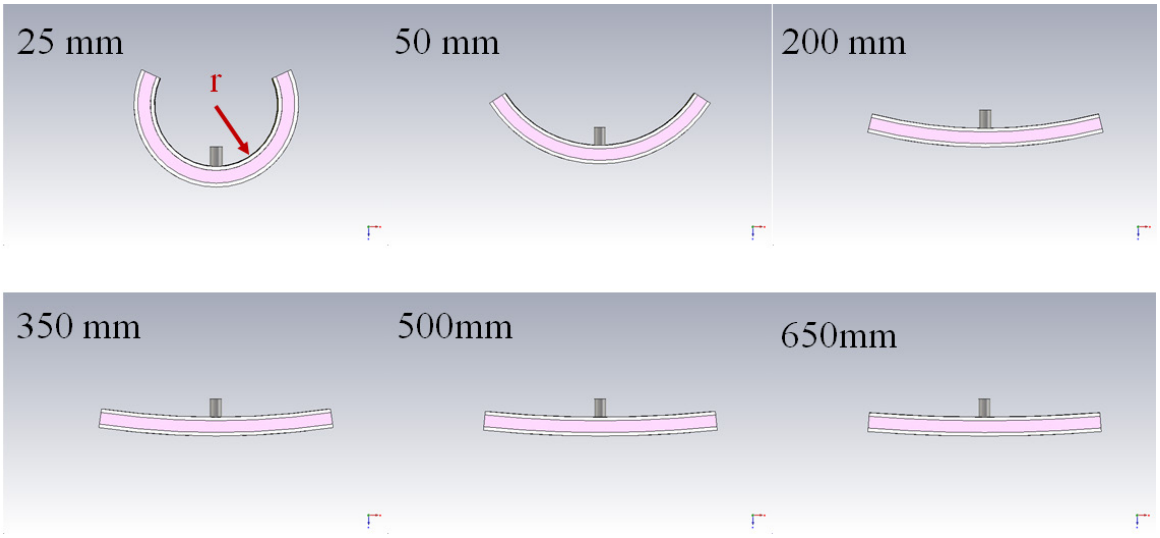

Figure 2-14: Top view of a bent 2x2 array, around a virtual cylinder with radius 'r', [37] © 2019 IEEE

The higher the bending is, the more the array is affected by a shift of the S_{11} curve to lower frequencies, roughly in the order of 5 MHz to 10 MHz. However, except for the extreme case of bending ray equal to 25mm, the minimum frequency bandwidth requirements of -10dB are satisfied even in non-flat configuration, as it can be seen in Figure 2-15.

2.4. OVERALL ANALYSIS OF THE RESULTS

The antenna was simulated with CST Microwave Studio 2018. The matching conditions of a single patch antenna - evaluated under different substrate configurations show a return loss better than 15 dB over the entire working frequency band 3.4-3.8 GHz and an average antenna gain of 8 dBi over the same band. The single element antenna has a nearly symmetric radiation diagram on the H- and E-planes, with a HPBW of about 76°.

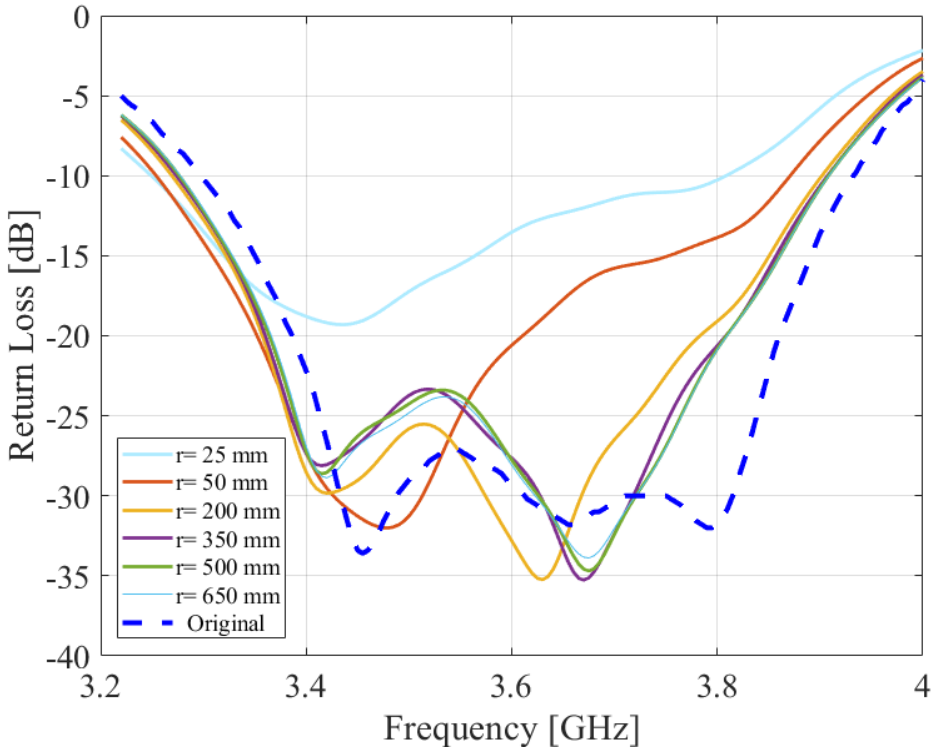

Figure 2-15: Simulated S_{11} parameter for the 2x2 array with RT Duroid 5880/Rohacell 31HF, under different bending conditions, [37] © 2019 IEEE

The return loss of the array configuration shows a theoretical return loss better than 25dB over the entire band and an average antenna gain of 12 dBi. Due to the intrinsic geometry of the array, the antenna has a nearly symmetric radiation diagram on the H- and E-planes, with a HPBW of about 44°. This means that the main lobe aperture lays in the range of ± 38° (single element) and ±22° (2x2 array) which makes this design very attractive [44] for any base station application when placed below the UAV fuselage, with the main lobe perpendicular to the ground. In this regard further simulations were run in order to bend the array around a fuselage (i.e a virtual cylinder) and simulate the behaviour of the return loss under different conditions. The antenna array behaves properly in most cases: there is a general shift in frequency towards the lower bound when the bending ray is close to 25mm while performances tend to normality when the bending radius is close to 650mm, like a flat antenna array.

By comparing the results, it is possible to conclude that the array design generates intense radiation at the centre and achieves more directivity and gain. As visible from the

simulation results, the 2x2 array antenna outperforms the single element antenna in terms of gain, as obvious, but most of all in bandwidth, while dramatically increases neither the complexity of the design nor the footprint and weight.

Design of antennas for broadband UAV applications over 5G networks brings definitely new challenges to designers. During the research activity it was seen that the single microstrip antenna performances were lower than compared to those of a 2x2 array antenna, which - as expected - outperformed the single antenna in terms of gain and impedance matching. Anyway, the proposed array is very simple and uses low-cost substrate materials. Especially, the use of an innovative and special foam like the Rohacell HF series provides a substrate that has a dielectric constant very close to air while keeping the antenna mechanically in place. Matching characteristics of the array antenna are evaluated under different bending conditions due to UAV installation on a fuselage. Results show matching performance acceptably robust in most cases, although a slightly shift in the resonant frequency is seen. Overall, the performance of the antennas meets the desired requirement in terms of return loss, gain and - especially – mechanical dimensions and weight, although it was not possible to finalize the prototype due shortage of materials and difficulties in coordinating activities during to the different lockdown periods.

CHAPTER 3. RAY LAUNCHING SIMULATION TOOL

This chapter introduces the Ray Launching simulation tool and the motivations behind the technological transition from Central Processing Unit (CPU) to Graphics Processing Unit (GPU) computing and the enhancements in terms of simulations speed-ups under different conditions. Section 3.1 provides a brief introduction and an overview, then section 3.2 describes the Ray Launching (RL) tool. Section 3.4 guides the reader through the observed computation efficiency and the comparison among different NVIDIA GPUs.

3.1. FROM CPU TO GPU COMPUTATION

Deterministic wave propagation modelling represents a state-of-the-art technique for RF channel analysis. The accuracy of site-specific propagation models, like ray tracing or ray launching, has seen great improvements in the last few decades thanks to better characterization of propagation mechanisms [45]. Although the compute capability of modern processors is constantly increasing, deterministic models still require significant runtimes to achieve accurate results, which has motivated the research community to extensively look for optimized and efficient acceleration methods [46]. Unfortunately, the complex mechanisms of electromagnetic waves as well as the huge amount of geometric calculations can make CPU computation inefficient. It can be reported that standard models - lacking of any speeding-up expedient - take more than an hour to retrieve channel characteristics across a kilometre-scale scenario with a single radio source [47]. Parallel computing – on the contrary - is a process of decomposing a large serial task into smaller

sub-tasks, which can be calculated concurrently. Multi-core processors are currently the most commonly available and exploited parallel computing platform, allowing much faster computations compared to a single core, as long as the computer code is optimized to take advantage from the multiple cores [48]. Furthermore, interest has grown rapidly in recent years towards harnessing the power of graphic hardware to perform general-purpose parallel computing. This alternative approach has become widespread and is based on the use of the GPU—in addition to the CPU—for general purpose computing.

Having effectively reached a limit in the improvement of the single-core frequency of CPUs, GPU computing has become the method of choice for applications with high computational demands. Although GPUs have been known in the computing industry for over 40 years, they have not represented a breakthrough until programmable and general purpose (GPGPU) have been developed. Since then, the computation potential has gained increasing acknowledgement, and GPUs have become far more than an embedded device for display operations: their special design allows to perform many operations simultaneously and to perform computation-heavy tasks that would otherwise require a large computer cluster. Moreover, modern GPUs are equipped for double-precision mathematical operations in parallel configuration, which extends the range of applications even further. It is anyway important to note that even if parallelisation is not always guaranteed by simply having installed a GPU card and using CUDA language, it can be potentially achieved at a high- or low-level scale for many applications [49].

By means of a comparative study of the computation efficiency in terms of calculation time, this chapter aims at shedding light on the crucial benefits that GPU computing can bring to the characterization of electromagnetic propagation between an UAV flying over an urban area and users roaming at street level. For what has been investigated in scientific literature, no research activities have been devoted so far to comparative, detailed, cost-benefit analyses of GPU architectures applied to electromagnetic computation problems. This represents one of the main novel contributions of this dissertation since – surprisingly - high-end, more powerful GPU card might not always provide the greatest computation efficiency as it will be shown in the following.

As a matter of fact, while UAV assisted wireless communications are currently envisaged in the framework of 5G and beyond [7], experimental investigations of the A2G link are extremely challenging and complex due to the limited payload, the problem in powering up flying transceivers and the regulations to comply with at national/international level especially within inhabited areas. Therefore, ray-launching simulations can represent an easier and cheaper way to improve awareness about A2G propagation properties, as long as the corresponding computation effort is worth it. In this regard, a key characteristic of the ray launching approach is that rays do not interact each other along their own propagation paths. From departure to arrival, ray paths can be independently traced, which is of great advantage for GPU-based computation thanks to the intrinsic parallelisation degree within the whole propagation process.

3.2. BRIEF DESCRIPTION OF THE RAY LAUNCHING TOOL

Due to the increase in the computational demands of modern applications, many developers are currently looking for different ways to accelerate their applications beyond the – limited – speed that conventional CPUs can provide. Among all the possible solutions, the baseline for the GPU-based A2G propagation assessment proposed within this dissertation is the Discrete Environment-Driven Ray Launching model (DED-RL), which has been introduced for the first time in [31] together with the related computational theory and which will be used extensively to simulate, retrieve, and collect the data in this PhD thesis.

As with all RL algorithms, DED-RL is suitable for prediction over large areas or volumes. More specifically, it has been designed in the recent years to perform fast deterministic propagation prediction on 3-D outdoor surfaces of all buildings and streets in a given target area, to enable multi frequency RF coverage design and optimization.

The software relies on a digitalised 3D urban model where each building is a polygon prism with a defined shape, material, position and height. The model is totally discrete, i.e. the building walls are properly discretized into “tiles” with a predetermined size. DED-RL

has also inherited some advanced features from a pre-existing RT model developed at the University of Bologna, such as the Effective Roughness (ER) diffuse-scattering model.

In this regard, it should be pointed out that conventional RT models usually account for rays that undergo specular reflections or diffractions, and for this reason they fail to properly address diffuse scattering phenomena. As intended here, diffuse scattering refers to the signals scattered in other than the specular direction because of deviations (surface or volume irregularities) in a building wall from a uniform flat layer. Recent experimental studies have shown that diffuse scattering contributions due to buildings façades or lampposts or monuments play an important role in determining time and angle dispersion of radio signals in real environments [50]. Diffuse scattering can have thus a significant impact on radio propagation in urban areas, as it will be shown later on in section 4.6.

In addition to the environment discretization, the algorithm is also "environment-driven", meaning that ray tubes are launched only towards the tiles that are visible from the transmitter, and these ray tubes are then bounced toward tiles that are visible to each other. In the DED-RL tool rays continue to propagate as long as the power level info they carry is above a propagation threshold. Once it is below, that specific ray is stopped, and the propagation for that specific ray is terminated.

Another advantage of the discretization is that all the visibility relations among the tiles can be pre-computed and properly stored into a "visibility matrix" since the tile centres can be assumed as fixed points. This visibility pre-processing takes advantage of GPU parallelization and must be done only one time for a single simulation scenario. Once the pre-processing is done, ray bouncing can be performed very efficiently for any transmitter location in the same environment. All these features are implemented in DED-RL through the CUDA C++ language for NVIDIA GPUs. Using the combination of the above-mentioned techniques in addition to GPU parallelization, DED-RL is thus able to achieve very high levels of computational efficiency – up to four orders of magnitude compared to a conventional ray-tracing algorithm – while retaining a good level of accuracy, despite the intrinsic error introduced by any environment discretization [51].

All the main features of DED-RL algorithm described above — visibility pre-processing, launching of ray tubes, ray bouncing, and field computation — are suitable for code parallelization via GPU acceleration and thus may benefit significantly from GPU-based computation due to its ability to process vectors or matrices with extreme efficiency, as it will be shown in the following sections.

3.3. SIMULATION SCENARIO AND ITS PARAMETERS

The DED-RL simulations take into account both antenna patterns (isotropic and directive) and different parameters of the transmitting system such as frequency and power, as well as the number and types of the allowed propagation interactions (i.e., reflections, diffractions, diffuse scatterings) to be considered. Specular reflection and diffraction are modelled according to the Geometrical Theory of Propagation (Geometrical Optics + Uniform Theory of Diffraction), while diffuse scattering is modelled through the Effective Roughness (ER) model [50-52], whose main parameter is the diffuse scattering coefficient S. The output of the simulations of technical interest is the received power level in dBm at ground, while path loss and other major propagation figures are retrieved by means of specific post-processing scripts.

The three urban environments in Figure 3-1 have been picked up as good representatives of dense inhabited areas: one American and two European cities with towers, churches, lengthy porticoes, and a specific narrow maze of streets that lead to a well-preserved historical centre or – conversely - wide streets full of skyscrapers that end up into a modern metropolitan centre.

(a) Bologna (b) Munich (c) San Francisco

Figure 3-1: Digitalised Urban models for three different cities, © 2021 IEEE

Concerning resolution, a discretization with 10m x 10m tiles has been considered; further details about the simulation scenarios can be found in TABLE 3-1.

TABLE 3-1: URBAN SCENARIO STATISTICS, © 2020 ACES SOCIETY

	Bologna	**Munich**	**San Francisco**
Num. of Buildings	9.377	2.000	18.047
AVG. Height [m]	12.9	16.9	17.35
Height STD. Dev. [m]	6,7	8,2	19,63
Total Tiles	170.931	148.584	268.868
Built-up Area [%]	30.5%	37.8%	40.5%
Map Area [Km^2]	6.5	8.8	10.2

Ray Launching simulations have been extensively carried out for 8 different hovering positions at 7 different altitudes and 4 communication frequencies. In order to perform propagation studies with general validity and not influenced by specific antenna characteristics, in this research activity UAVs are considered to be equipped either with an isotropic (omnidirectional) antenna or with a directional one, installed below the drone body and pointing perpendicular towards the ground, with a fixed aperture angle θ. This angle θ is simply the aperture of an ideal and symmetrical radiation cone within which it is assumed to have an ideal constant gain and consequently negligible side lobes to keep the RL simulations affordable. This can be also seen as a best-case scenario where rays are launched only within a specific cone angle θ, thus drastically reducing the computation effort of calculating multiple interactions. In addition, this choice allows to possibly extend the results to a wider range of directional antennas as a function of the simple aperture angle θ which can then generalize the analysis to some extent since not linked to any specific antenna radiation diagram. Consequently, for the spot area covered on the ground (i.e the drone antenna footprint) it is easy to expect a circular shape whose radius depends on the aperture angle and the UAV altitude.

3.4. COMPUTATION EFFICIENCY

In order to investigate the computation time for UAV A2G propagation, worst-case ray-launching simulations of a full three-dimensional (3D) scenario were performed. DED-RL simulations were run by means of dedicated scripts within a MATLAB R2017B (Update 9) environment. The purpose of the scripts was to automate in a simple and efficient way the different runs concerning UAV positions and flight levels, as well as its transmitting frequencies.

3.4.1 Preliminary Insights and Observations

In addition to getting a huge number of data samples and to investigating different situations, the same simulation runs gave a better insight on the computation time and the speed-ups over GPU accelerated simulations, according to the parallelization concept introduced in section 3.1 and which forms the basis of the DED-RL tool used in the research activity. Simulations were run on an Intel® Xeon® CPU E5-2620 v3 @ 2.40GHz [6c/12t], 48 GB RAM, cooperating with a Nvidia Titan Xp GPU with 12 Gb and 3840 CUDA Cores. Further details of the NVIDA GPU card can be found in TABLE 3-2.

Figure 3-2 summarises the simulation time for a single run as averaged among the eight UAV positions over Bologna city using an isotropic antenna, but similar trends were observed also for the other two cities of Munich and San Francisco.

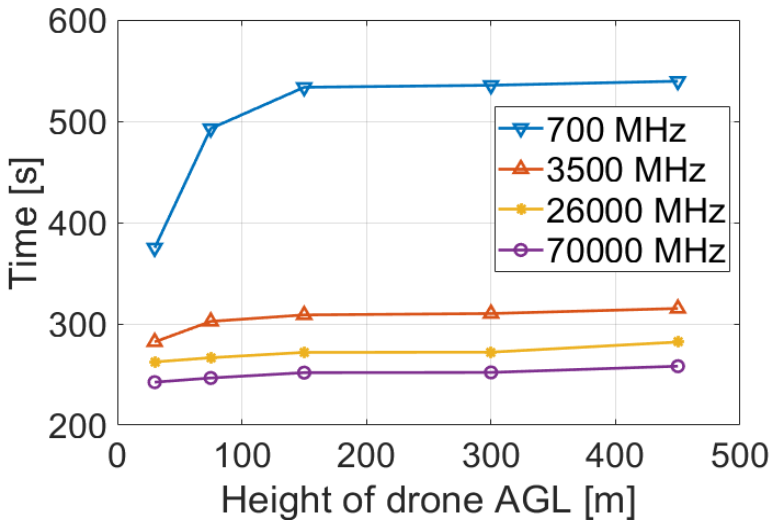

Figure 3-2: Simulation time over UAV altitude for different frequencies, with an isotropic antenna over Bologna city, © 2020 IEEE

This clearly shows a dependency of the computation time both over frequency and flying altitude of the UAV. As a matter of fact, the lower the frequency the longer the computation time, which is seen more than halved when moving from 700 MHz to 70 GHz. Conversely, the higher the flying altitude, the longer the simulation time although simulation time keeps basically steady from a certain height of the UAV onwards. Both behaviours are clearly in connection with the number of rays propagated by the RL tool: at higher frequencies the rays are terminated earlier due to the higher attenuation involved and thus the simulation time is shorter. Conversely, at higher altitudes, there is a higher number of rays that propagate and thus the simulation time increases. From the same Figure 3-2 it is possible to see that in our specific case the simulation time stays nearly the same above a certain UAV altitude onwards (of ~300m), due to the number of ground tiles reached by the UAV under the assumptions of a defined map size and the use of the isotropic antenna.

In addition to the isotropic case, the investigation has been carried out also in case of directive antennas. Replacing the isotropic antenna with a directive one, having namely an aperture angle θ=40°, 60° and 80° - to take advantage of the most significant runs already calculated in the previous sections - leads to more realistic study cases.

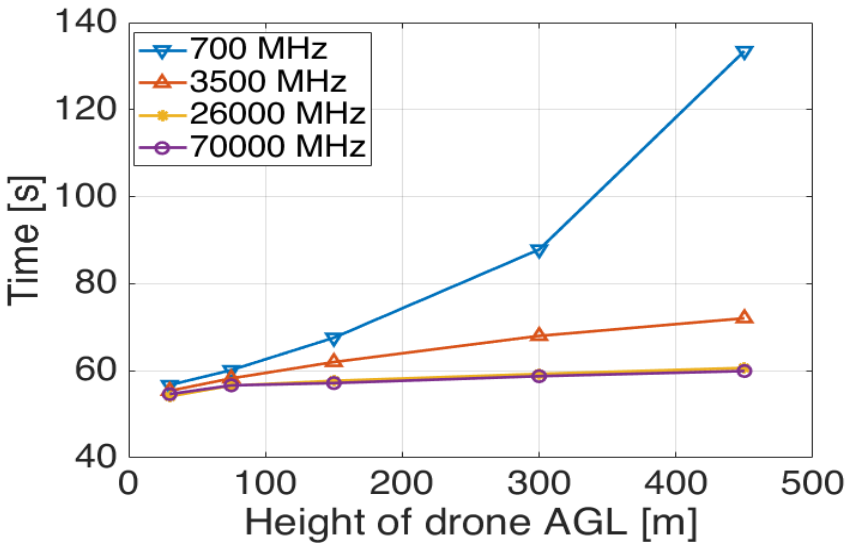

Figure 3-3: Simulation Time over UAV altitude for different frequencies, Directive antenna over Bologna city © 2021 IEEE

Figure 3-3 shows the same trend as in Figure 3-2, i.e computation time as a function of drone altitude. Results have been averaged among the 3 different directivity values.

It can be seen that the higher the drone altitude and the lower the transmitting frequency is, the longer it takes to complete the computational time for the requested simulation. One more time, for higher frequencies there is a lower dependency on altitude and the trend stays mostly flat. On the contrary, for lower frequencies like 700 MHz, the simulation time is remarkably higher, but it levels off for higher frequencies. This is justified by the use of a directive antenna which creates a specific radiation footprint on the ground: the radius of this footprint increases with the UAV altitude and within this same footprint the number of rays that propagate is dependent of the frequency.

Figure 3-4 similarly, shows an interesting connection between directivity and computational times. Results have been averaged among the different drone heights. It shows that the lower is the antenna directivity and the transmitting frequency, the longer the computational time is. One more time this highlights the strong link existing among frequency, footprint and directivity with regard to the rays that the RL has to manage in the propagation process.

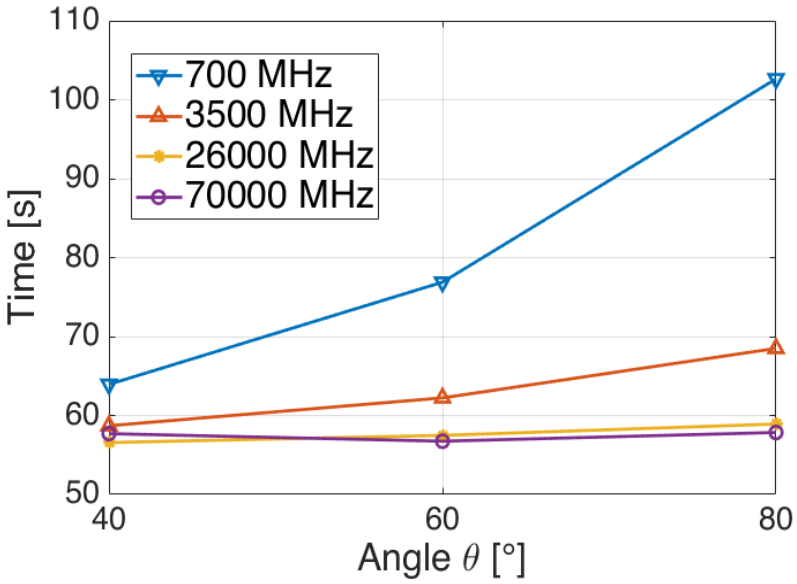

Figure 3-4: Simulation Time over aperture angle θ for different frequencies, Directive antenna over Bologna city, © 2021 IEEE

To sum up the matter in a different perspective, Figure 3-5 shows the same trend as Figure 3-2, i.e., computation time as a function of drone altitude, but this time the results have been highlighted with regard to the aperture angle θ at 3500MHz instead of the whole frequency span.

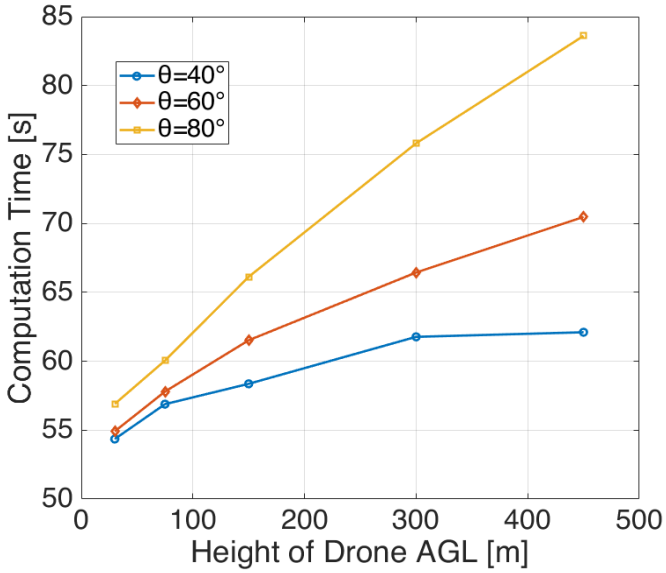

Figure 3-5: Simulation time over UAV altitude for different antenna aperture angles θ, at 3500 MHz, © 2021 IEEE

This figure shows an interesting connection between directivity and computation times: the wider is the antenna aperture θ or higher the flying altitude, the longer the computation time. Both situations described in Figure 3-2 and Figure 3-5 are in good agreement with the research activities introduced in [53] under the assumption that there are more rays that propagate at lower frequencies, for low directivity values or for higher altitudes of the drone. The explanation of this trend relays on the ray-launching algorithm and its strong relationship between the number of rays that are launched – and kept "alive" along the propagation way - and the system parameters, configured under these specific circumstances.

3.4.2 Multi GPU investigation and comparison

Following the promising results in subsection 3.4.1, two more NVIDIA GPU cards have been temporary set-up inside the same workstation. As a whole, the research activity was based on two cards belonging to the professional business sector (Tesla series), namely

Tesla K40c (medium end) and Tesla P100 (high end), while the last one – used also in the previous subsection - belonging to the gaming business one (GTX series), namely Titan Xp (high end) as it can be seen in Figure 3-6.

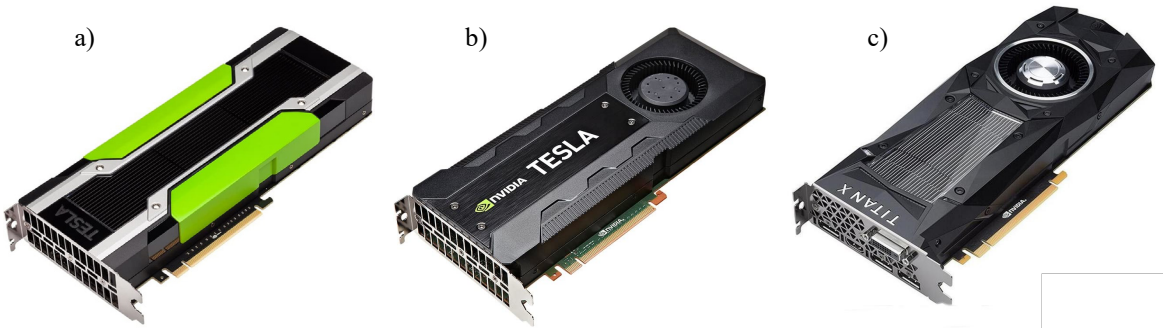

Figure 3-6: NVIDIA GPU cards used during the research activity. From left to right: Tesla P100 (a), Tesla K40c (b) and Titan Xp (c). Courtesy of © NVIDIA

Main specifications are listed and briefly described in TABLE 3-2. Although an extensive description of hardware details and specific mechanism of NVIDIA GPUs is out of the scope of this section, the reader can find interesting details in [54] for Kepler and in [55] for Pascal architectures.

Regardless of the specific business sector they have been designed for, GPU processing capabilities can be measured in terms of streaming processors (SP) and Video RAM (VRAM), together with floating point operations per second, either single or double precision. It can be seen from TABLE 3-2 that the three NVIDIA GPU cards show the same VRAM but they differentiate from each other for specific features. The Tesla series cards, as expected for professional business purposes, show better performances in terms of double precision TFlops, while the GTX card, gaming-oriented, really lacks.

Conversely, the GTX card outperforms the Tesla series concerning single precision TFlops and memory clock, as expected from a card that must react promptly in tough gaming sessions.

TABLE 3-2: NVIDIA GPUs CONFIGURATIONS UNDER INVESTIGATION, © 2020 ACES SOCIETY

GPU Card	Architecture	Streaming Processors	Core Clock	VRAM	Single Precision	Double Precision
Tesla K40c	Kepler, GK180	2880	745 MHz	12GB	5.04 TFLOPS	1.68 TFLOPS
Titan XP	Pascal, GP102	3840	1405 MHz	12GB	12.15 TFLOPS	0.38 TFLOPS
Tesla P100	Pascal, GP100	3584	1190 MHz	12GB	9.32 TFLOPS	4.73 TFLOPS

The number of SP is comparable between the two high-end GTX and Tesla cards, being instead slightly lower in the medium-end Tesla card. It should be remarked that performance improvements are an increasing function of the number of available computing cores; the more cores are available, the higher the speedups that can be achieved compared to sequential counterpart versions.

Together with the complexity of device architectures, it is seen that computational power of GPUs is rapidly growing with many new features proposed to developers, to the researchers or to the gaming community, like the very recent Ray Tracing (RT) cores for real time ray-tracing calculations [56]. Nevertheless, research targets must not be confused by the multiple features and capabilities: one of the most important aspects when comparing performances in terms of computation times, is to get a fair and balanced set of output metrics for proper accelerator comparison.

In this regard TABLE 3-3 summarises the main DED-RL parameters set-up during the different simulation runs. In fact, it was important to fine-tune the DED-RL parameters - among those related to the addressed GPU memory and the number of rays launched per cycle - with a set of commonly acceptable values for all the involved GPUs and to get comparable results among the different scenarios.

TABLE 3-3: RL MAIN SIMULATION PARAMETERS FOR GPU COMPUTING, © 2020 ACES SOCIETY

Parameter	**Values**
Frequency	0.7, 3.5, 26 and 70 GHz
UAV heights	30, 50, 75, 150, 300, 450 m AGL
UAV hovering positions	8 circular positions
Number of Interactions	5 bounces, 5 reflections, 2 diffractions and 1 scatter
Number of Combined Interactions	3 reflections/diffractions (max), 3 diffractions/ scatters (max)
GPU Memory Allocation Heap Size	1536 MB
Maximum LOS Rays Per Cycle	100000
Amount Of GPU Memory For Packets	40%

For benchmarking purposes, the DED-RL software was configured assuming a single UAV hovering over a 3D urban city environment at different positions in space.

Three different urban models were investigated, as anticipated in Figure 3-1, with a special focus on their city centres: Bologna (Italy), Munich (Germany) and San Francisco (USA). This was done to explore how much a specific urban map was affecting the computation time. Coverage predictions were performed on a whole urban area with a single tile resolution of 10x10 m and general details as further specified in previous TABLE 3-1.

By means of *tic* and *toc* Matlab commands [57], it was possible to measure - and to focus only on - the elapsed time before and after the call to the executable DED-RL file.

Although, on one hand, this is the most straightforward way to measure the computation time in a coherent way among the different GPU cards, on the other hand it may be objected that the CPU processing affects this measurement as part of the whole RL code execution. Not only that this part is negligible, but it must also be emphasised that this part is common – and the same – for any simulation run on the same workstation, thus returning a set of comparable results, at least in relative terms among the three GPU cards.

3.4.3 Analysis of Results

Simulation results shown in the following subsections represent the combined outcomes of multiple aggregated runs corresponding to different UAV spatial hovering positions (i.e. lat-long UTM coordinates and height above ground level,) or transmitting frequencies, over the three different test-referenced scenarios. This strategy was agreed to make available significant data samples and a clear breakdown of run parameters and characteristics.

3.4.3.1 Computation time for isotropic antennas

In this specific subsection, the UAV was equipped with an isotropic antenna. Although this type of antenna does not have any physical meaning, it allowed to run a worst-case scenario where rays were launched in all directions, thus increasing the computation effort of calculating multiple interactions at 360° spherical degrees. Furthermore, it is worth noting that the isotropic case can somehow represent real situations where the radiation lobe of the antenna is wide enough to illuminate the whole urban area below the UAV frame.

To get the representative graphs in Figure 3-2, runs have been averaged over the UAV spatial positions, as it turned out to slightly affect the computation time. According to Figure 3-2, this time is generally longer at lower frequencies and shorter at higher frequencies. Differently from “Image” Ray Tracing techniques, where the intensity of a ray can be computed only after the whole ray path - from the transmitter to the receiver - is traced, Ray Launching can take note instead of the ray intensity while it is being traced. Therefore, rays with negligible intensity can be stopped and discarded, thus saving computation time. As propagation losses increase with frequency and distance, many rays are therefore dismissed by the DED-RL algorithm, thus explaining the achieved results.

At the same time, the Tesla P100 GPU card tends to be the fastest one at lower frequencies, with an average speed up factor of ~4x vs. Tesla K40c and ~2x vs. Titan Xp. This speed-up factor is seen to increase with the complexity of the environment. In the most challenging case (San Francisco, according to the parameters listed in Table 3), the

Tesla P100 shows a simulation time which is ~3x and ~7x lower compared to the Titan Xp and the Tesla K40 cards respectively, whereas the three GPU cards show similar performances from 26 GHz onwards. On one hand, these results are reasonable and proportional to the number of rays vs. computed interactions. On the other hand, this sounds like a surprising result: it might be expected the high-end Tesla P100 card to always be somehow the first of the class due to its technical specs and economical value, while actually the gap with the Titan Xp is indeed minor.

In agreement with CUDA programming best practices [58] and literature [59], this behaviour is likely related to the additional overhead the Tesla P100 brings in connection to its intrinsic complexity. This can limit the computation speed when there is no good balance among the different thread blocks scheduled onto the GPU Streaming Multiprocessors (SM). However, this imbalance is more likely to happen in less challenging cases, i.e. the higher frequencies, due to the selective discarding of those rays whose intensity falls below the minimum power threshold, as previously mentioned.

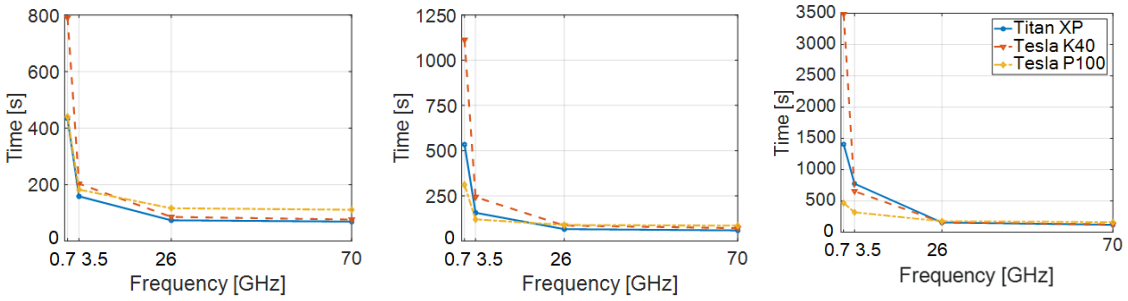

(a) Bologna, Italy (b) Munich, Germany (c) San Francisco, USA

Figure 3-7: Computation time [s] over frequency [GHz] for different Nvidia cards and environments, © 2020 ACES SOCIETY

3.4.3.2 Computation time for directive antennas

Following the interesting results of the previous subsection, the UAV was then equipped with a directional antenna of fixed aperture angle θ, placed under the UAV fuselage and pointing downwards.

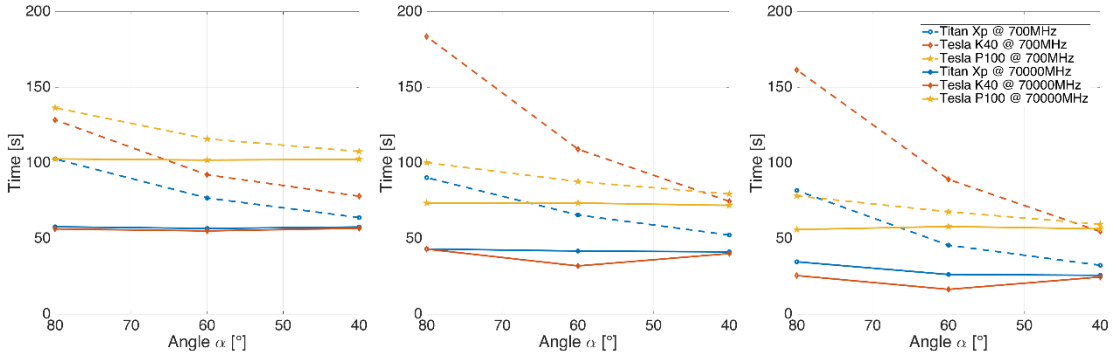

(a) Bologna, Italy (b) Munich, Germany (c) San Francisco, USA

Figure 3-8: Computation time [s] over antenna aperture angle [°] for different NVIDIA cards and environments, © 2020 ACES SOCIETY

This can be seen as a best-case scenario where rays are launched only within the specific cone θ, thus drastically reducing the computation effort of calculating additional interactions.

To get the representative graphs in Figure 3-8, runs have been averaged in terms of spatial positions and results split into low and high frequency samples, 700 MHz and 70GHz respectively. On that note, it is seen that at 70GHz the simulation time are flat all over the α angle span, with the Tesla P100 now the slowest among the cards.

As the limited number of rays to be traced at high frequency is further reduced by the antenna directive pattern, the simulation time is indeed simply dominated by the specific overhead of the GPU, which is likely to be heavier for the Tesla P100. This is not completely true at 700MHz, where plots are no longer flat and simulation time logically decreases as a function of the angle α, (i.e. it increases as a function of antenna directivity).

Generally speaking, the use of directive antennas in this test-case brings out the way in which GPU overhead represents an important factor for any evaluation of the computation time and it justifies the swap in the results. From these plots, it is possible to see the Titan XP card to better perform out of the other two cards, which is not always true in case of an isotropic antenna.

3.4.3.3 Notes on computation time

It was demonstrated the benefit of GPU parallelization as a means to accelerate ray launching field computation, with typical computation times for complete predictions over

all building surfaces ranging from seconds to few tens of minutes, depending on the size of the urban scenario, the hardware used for simulation runs and the characteristics of RF propagation. This shows the potential benefit of GPUs for electromagnetic simulations, in fair agreement with the main outcomes of previous works in [60-62].

It was seen how computation time decreases with frequencies and the use of different directive antennas could affect simulation time. As it can be expected, the wider the antenna radiation cone, the longer the simulation time, although remarkable only at lower frequencies. It was also seen that both professional and gaming GPGPU provide reasonable and consistent results in terms of computation time, the former having better performances at lower frequencies due to the higher number of rays to be processed. On the other hand, performance can be degraded when using the high-end Tesla GPUs in less demanding environments, due to their additional overhead.

CHAPTER 4. NARROWBAND PROPAGATION

Compared to terrestrial cellular networks, UAV-assisted communication systems are characterized by some peculiar aspects that should be accounted for in the propagation modelling procedure. Section 4.1 and section 4.2 introduce the challenges faced during the research activities, while section 4.3 provides a possible solution to overcome simulation constraints. These same sections form the baseline to the calculation of the LOS probability as well as the path loss exponent and the sigma shadowing, in section 4.4 and section 4.5 respectively.

4.1. EFFECT OF THE ANTENNA RADIATION PROPERTIES

Propagation measurement/simulation activities should be always planned with the transmitting-receiving locations mutually included inside the main radiation lobe of the antennas. This is done to minimise the possible side propagation effects like the multiple direction of departure / arrival of the different multipath components. Therefore, the simulation/measurement area shrinks down for increasing directivity of the on-board antenna and/or for lower flight levels of the UAV (from red to green colour in Figure 4-1), since the UAV is expected to be equipped with an antenna commonly pointing towards the ground. This difference in the area extension – which depends thus on the on-board antenna radiation properties - may correspond to different best-fitting lines matching the collected attenuation values shown in Figure 4-2, again moving from red to green colour.

As a consequence, this means that the on-board antenna directivity can significantly affect propagation parameters like the Path Loss Exponent (PLE) α and the sigma

shadowing coefficient σ of a Hata-like path-loss model [27], respectively representing the slope of the best-fit line and the standard deviation of the attenuation samples with respect to the fitting line.

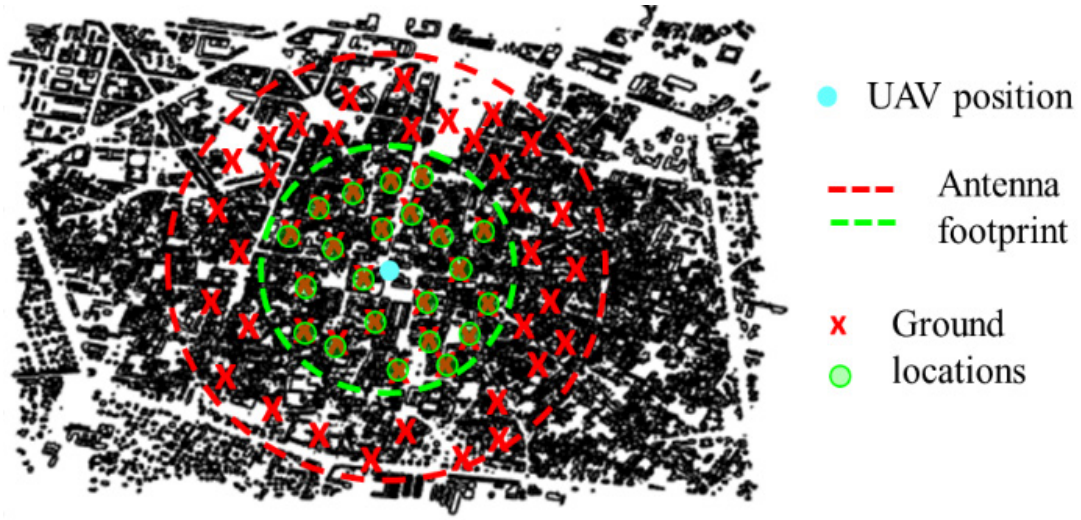

Figure 4-1: Antenna footprint and the expected propagation area, example, © 2021 IEEE

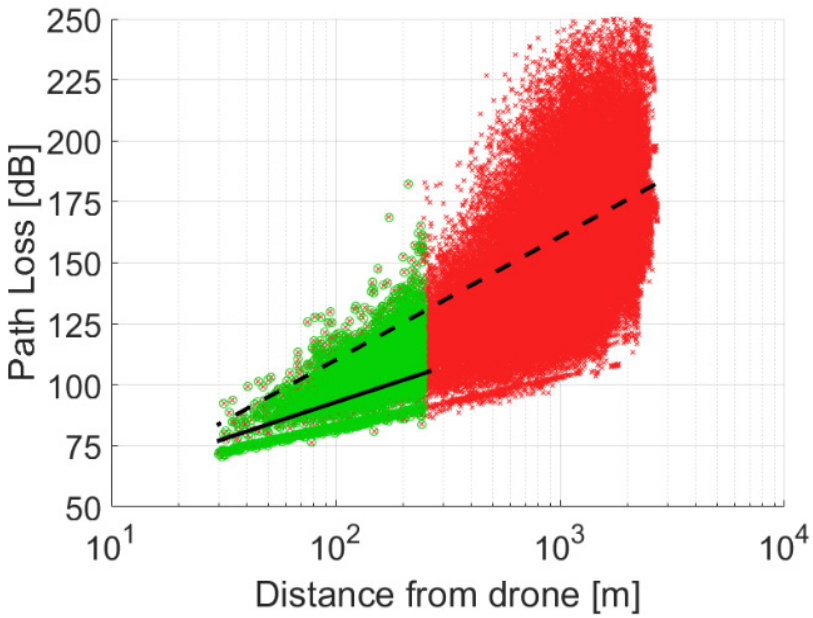

Figure 4-2: Impact of the antenna footprint, © 2021 IEEE

It is worth pointing out that the same impact does not automatically occur in terrestrial cellular networks, where the main lobe of the base station antennas is fundamentally parallel to the ground (or slightly tilted downwards), and therefore increasing the

directivity primarily restricts the size of the measurement/simulation area mainly in the azimuth direction rather than reducing the distance range.

4.2. NOTES ON THE PATH LOSS FITTING FORMULAS

According to the Hata-like approach, the PLE can be derived by fitting with a straight line (Figure 4-2) a large set of point-specific attenuation values displayed in a log-log graph. The attenuations samples often come from measurement investigation, but they can be provided by deterministic propagation model as well, as achieved in the study herein.

Two different equations are usually considered for the best-fit line [63-64]: the first is a "fixed intercept" model (also referred in literature as the "close in" model) as in eq. (4-1), where d is the distance between the drone and the ground tile, $PL_{free}(d_0)$ is the free space loss at a reference distance d_0 (set equal to 1 m for simplicity) and α_1 represents the PLE; the second consists of a "floating intercept model" as in eq. (4-2), where a second fitting coefficient (β) is introduced in addition to the PLE (α_2).

$$PL_{dB}(d) = 10 \cdot \alpha_1 \cdot \log_{10}\left(\frac{d}{d_0}\right) + PL_{free}(d_0) \qquad (4\text{–}1)$$

$$PL_{dB}(d) = 10 \cdot \alpha_2 \cdot \log_{10}(d) + \beta \qquad (4\text{–}2)$$

Provided that the distance range is similar to or even larger than its corresponding attenuation range (in relative terms), Equations (4-1) and (4-2) turn out to be quite similar, with $\alpha_1 \approx \alpha_2$. This may be not the case in UAV to ground communications, when the flight level is low and/or the UAV antenna directivity is large (Figure 4-3), corresponding to a quite narrow beam and thus a small antenna footprint.

Ground locations falling within the main antenna lobe would basically share the same link distance, whereas attenuation can still undergo large fluctuations, especially in case both LOS and NLOS conditions occur. In Eq. (4-2), the corresponding optimal value of α_2 might become awkwardly large, with questionable physical meaning although mathematically correct. Conversely, in Eq. (4-1) α_1 would be much less affected under the same conditions, i.e., it keeps physically sounded whatever the UAV height and its antenna

directivity are. This is shown as an example by the continuous and dashed lines in Figure 4-2. Because of this greater robustness, only the close-in model in Eq. (4-1) is considered in this thesis and in the frame of the research activity.

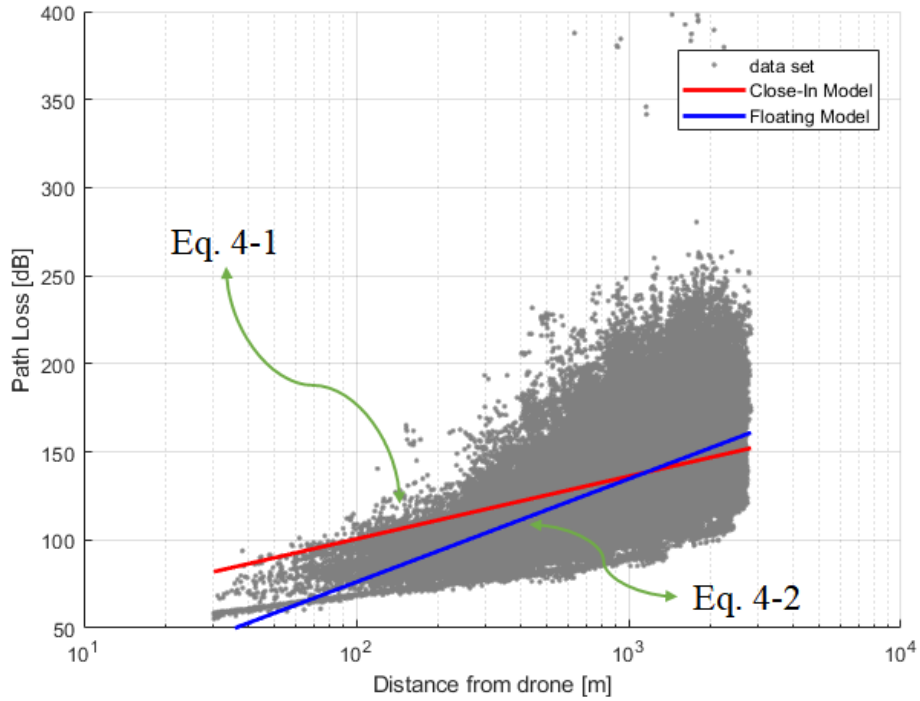

Figure 4-3: Path loss vs. Distance for a UAV; the same data set is fit with the close-in model (red line) and the floating one (blue line).

4.3. MAXIMUM TOLERABLE LOSS

Wireless communications are always affected by signal attenuation and a maximum acceptable propagation loss (PL_{max}) can be easily set based on the transmitter power level, the receiver sensitivity and the noise threshold at the receiver side. Depending on the attenuation law, the maximum communication range can be easily estimated. The same limitations do not automatically apply when the propagation analysis is carried out by means of a software simulation tool, which can virtually compute any received signal intensity value, whatever the attenuation experienced by the propagating signal actually is.

In order for the channel simulations to effectively replace channel measurement, i.e., returning similar data set with a high level of confidence, a PL_{max} value must be properly set: the analysis of the simulations data should be restricted to the distance range where the

probability to compute attenuation values greater than PL_{max} is basically negligible. According to what has been proposed in [32], the statistical analyses carried out are limited to a maximum threshold distance d_{max}. However, due to the broadband nature of the analysis, it has been extended to a dual PL_{max} definition: PL_{max}=160 dB for the lower frequencies – 700 MHz and 3.5 GHz - and PL_{max}=180 dB for the higher ones – 26 and 70 GHz. This strategy stems from the need to better address such a broad range of frequencies, where a single PL_{max} value, used in [32] [65] for a single frequency, would not have been sufficient to fit them all.

4.4. LINE-OF-SIGHT PROBABILITY

The availability of Line of Sight has a great impact on the properties of the wireless channel, and therefore on the performance of the wireless link. Propagation with a high Probability of LOS (PLOS) with a strong direct path intensity corresponds to free-space like conditions (i.e. PLE≈2) with limited σ values, whereas increase in both the PLE and the sigma shadowing σ effect is expected when LOS condition seldom occurs. Investigation of LOS probability is especially important in the mm-wave band, where multipath is often made of few, sparse components for the user to rely on in case the LOS path is obstructed.

Whether the LOS path exists or not depends on various factors, e.g., terrain features, density of buildings, their height and mutual distance or distribution. As ground users are inherently placed in the tiles centre by the RL algorithm, i.e., almost everywhere along the streets, the LOS probability discussed in this section basically depends on the UAV flying altitude and on the geometrical properties of the environment. It is worth mentioning that the geometrical LOS is independent of the system frequency. Similarly to TABLE 3-3, TABLE 4-1 shows the key simulation parameters used for the three dense urban scenarios, introducing the chosen dual PL_{max} values. For the sake of consistency within this dissertation, these same parameters will form the baseline for any simulation carried out during this research activity.

TABLE 4-1: RL PARAMETERS FOR NARROWBAND SIMULATIONS, © 2021 IEEE

Parameter	**Values**
Frequency	700, 3500, 26000 and 70000 MHz
Flight level	30, 50, 75, 100, 150, 300 and 450m Above Ground Level (AGL)
Position	8 locations (circularly distributed)
Number of Interactions	5 bounces (max 5 reflections, max 2 diffractions and max 1 diffuse scattering)
Number of Combined Interactions	3 among reflections and diffractions (max) 3 among diffractions and scatters (max)
Diffuse Scattering Coefficient	0.4 [for 700 MHz – 3.5 GHz] 0.6 [for 26 – 70 GHz]
Wall Relative Permittivity	5
Wall conductivity	0.01 S/m [for 700 MHz – 3.5 GHz] 0.4 S/m [for 26 – 70 GHz]
PL_{max}	160 dB [for 700 MHz – 3.5 GHz] 180 dB [for 26 – 70 GHz]

LOS probability can be easily and quickly estimated running RL simulations, setting the number of allowed interactions to zero, and then getting the ratio between the number of tiles where the received power is greater than zero and the overall tiles number inside the target area. In Figure 4-4 (a) LOS probability vs. UAV height for isotropic antennas is presented for the three cities of interest.

For the sake of comparison, i.e., to avoid the computation being affected by the different areas of the simulation maps (TABLE 3-1), the PLOS occurrence was calculated over circular spots of 2 km^2 underneath each UAV position (i.e comparison area). As expected, it can be seen in Figure 4-4 (a) that for an isotropic antenna, the higher the drone is flying, the higher the PLOS. Conversely, when the UAV is flying at very low altitudes, PLOS drops down, because of the increased shadowing level. In both cases, the trend is clearly monotonic, while the difference in LOS probability between the three urban samples may be attributed to the different properties of the building layers.

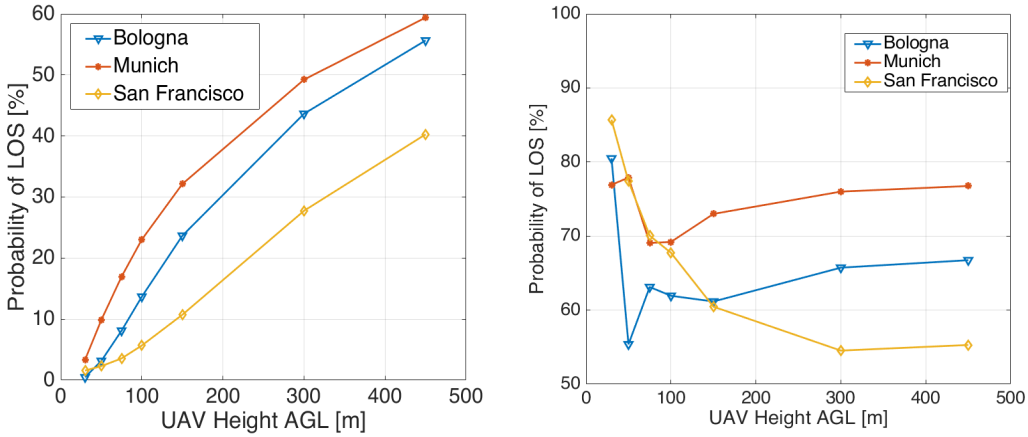

(a) isotropic antenna (b) directive antenna

Figure 4-4: LOS Probability for different antenna types, © 2021 IEEE

San Francisco exhibits the greatest building density and it includes some high-rise building areas. Furthermore, San Francisco has a hilly terrain profile. These reasons explain the corresponding lower values of LOS probability in Figure 4-4 (a).

In Figure 4-4 (b) the same LOS probability vs. UAV height is presented for a directive antenna, with an aperture θ=80° as an example - but similar trends have been observed also for other aperture values.

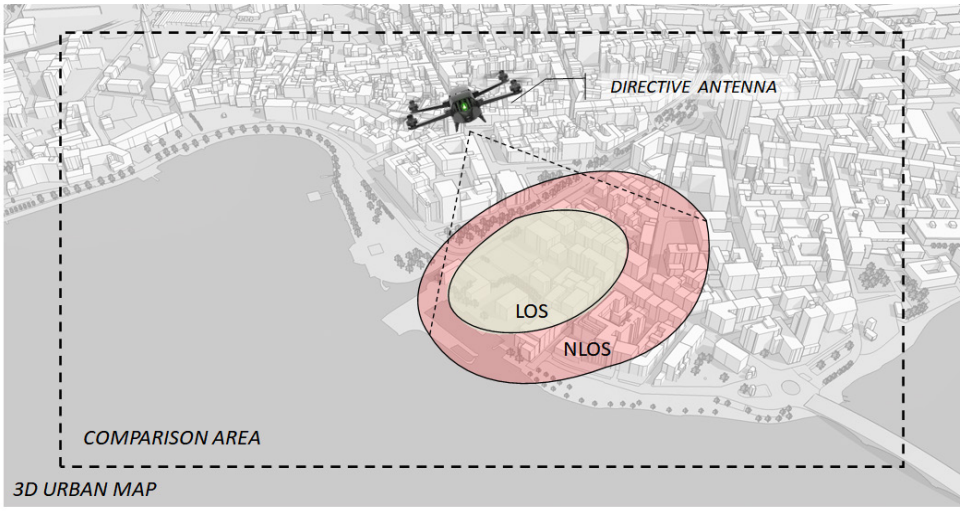

Figure 4-5: LOS and NLOS ratio in case of a directive antenna, example. PLOS tends to be higher since the calculation is run on a smaller area with less NLOS tiles although the LOS ones stay the same.

As a directive antenna on the UAV is expected to provide wireless connectivity to the users primarily through its main radiation lobe, the evaluation of the LOS probability is now carried out on the tiles inside the antenna footprint at ground level.

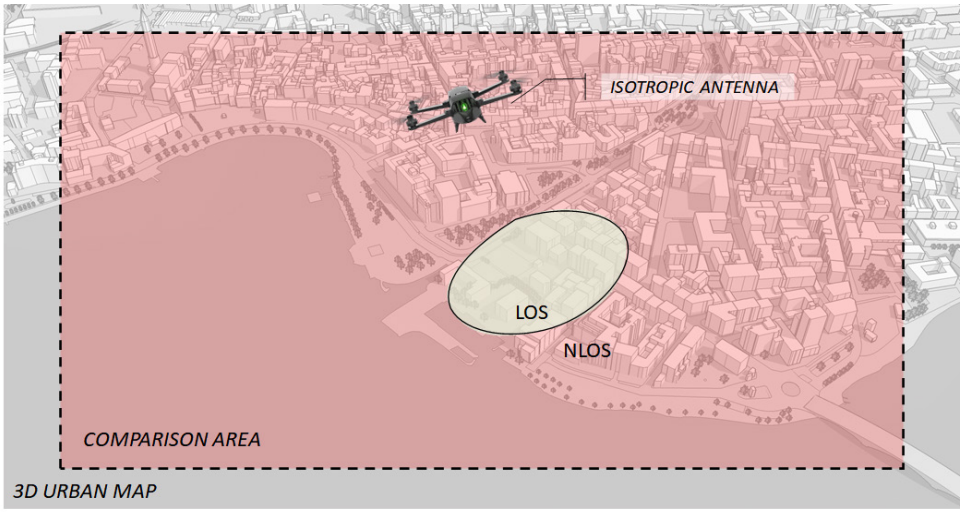

Figure 4-6: LOS and NLOS ratio in case of an isotropic antenna, example. PLOS tends to be lower since the calculation is run on a bigger area with more NLOS although the LOS ones stay nearly the same.

Performances of a directive antenna are based on the fact that, with a narrower beam, LOS is achieved with a larger percentage of points within its footprint as it can be seen in Figure 4-5. In contrast, the isotropic beam has LOS with fairly the same number of points as a whole but with a higher number of points not in LOS, as it can be seen in Figure 4-6.

Compared to Figure 4-4 (a), LOS probability in Figure 4-4 (b) is always greater, irrespective of the drone height. When the UAV is very close to ground, the footprint underneath is rather small and most of the few ground tiles inside it are in line of sight, corresponding to a probability equal to 80-85% in Figure 4-4 (b). While the UAV is flying at a greater altitude, more tiles fall within the ground spot. At first, they are likely to be shadowed by buildings rather than in sight of the UAV, and the LOS probability therefore drops down; then, the situation is reversed, and the probability begins to increase. This trend reaches then a steady state for which the PLOS becomes nearly constant at higher altitudes. According to these investigations, the minimum in this case can be related to a new parameter called “urbanization threshold” - expressed in meters – that gives a feeling

of the complexity of the 3D urban environment, in terms of number of buildings, heights, standard deviation, as per TABLE 3-1: while the UAV is flying higher – but still below this threshold - the PLOS drops down. Once the UAV overtakes the same threshold, the visibility of the UAV over the ground spot and consequently the PLOS starts to increase. This trend reaches then a steady state when the height of the surrounding buildings becomes somehow negligible with respect to the flying altitude of the drone. This value is between 50 to 75 meters in Bologna and Munich, while it is definitely higher in San Francisco where it reaches a value close to 300 meters.

The achieved results – with takeaways in both figures - should draw the attention to the key fact that having an A2G link does not always imply perfect LOS conditions. Since the UAVs might be expected to fly at altitudes lower than 100m in many applications, LOS turns out to be a rather uncommon condition in the isotropic case, whereas it does not occur in approximately 30% of the cases, when the directive antenna is considered.

The A2G channel behaviour is therefore less simple than it may appear, with multipath and shadowing effects that shall not be automatically negligible, and there is thus a need for further investigations about the A2G propagation mechanism.

4.5. PATH LOSS EXPONENT AND SIGMA SHADOWING

In this section, narrowband channel parameters are retrieved and analysed. The choice of an isotropic antenna is made in the following sub-section to focus the attention on the channel itself, with no misleading information coming from the antenna on board of the drone. Furthermore, it is worth noting that the isotropic case can somehow represent real situations where the radiation lobe of the antenna is wide enough to illuminate a large area below the UAV frame, e.g., when UAVs are deployed to set-up temporary emergency communication infrastructure after natural disasters. As drones can be as well equipped with directive antennas, e.g., to improve wireless connectivity at the cell boundary in cellular networks, the narrowband analysis is also carried out taking into account different beamwidths of the on-board antennas. To collect a common value for a specific altitude and frequency, regardless of the specific UAV hovering position, PLE and σ were

calculated by joining the different cloud of points for each of the 8 different drone positions and then calculating the best fit line according to Eq. (4-2). This strategy makes particularly sense for low UAV flight levels, where values can differ significantly among the chosen positions due to specific local obstructions; the higher the UAV flight level, the less this effect is seen, as all the location experience similar mean propagation conditions and obstructions from the environment.

4.5.1 Isotropic Antenna

The first parameter under investigation has been the path loss exponent α, which accounts for attenuation and for the "mean degree of obstruction" on the propagation of the paths. The main results about PLE are shown in Figure 4-7 for different UAV altitudes and different frequencies, using an isotropic antenna. Similar to [29][33], PLE has a decreasing trend with height: the higher the UAV is flying, the lower the PLE. It is worth noting that for each environment the values of α achieved at the lowest UAV height and frequency - respectively equal to 30m and 700MHz - are in quite good agreement with those retrieved from the well-known Hata model [27].

Nevertheless, the path loss factor reduction in Figure 4-7 for increasing flight height is faster compared to the trend highlighted by the Hata formula. Although the number of receiving LOS locations increases as the UAV flies at higher altitudes, the PLE at 450m is still greater than 2, according to LOS probability values which were well lower than 1 (Figure 4-4 (a)).

Concerning frequencies, PLE is faintly depending on them as already revealed in [27]: α increases with the frequency due to either more challenging overall propagation conditions as reported in section 4.6 or intrinsic attenuation as reflected in the cloud of points. This dependency is slightly higher for the lower bands, between 700 MHz and 3500 MHz, than for the higher ones, between 26000 MHz and 70000 MHz, where the gap is marginally noticeable.

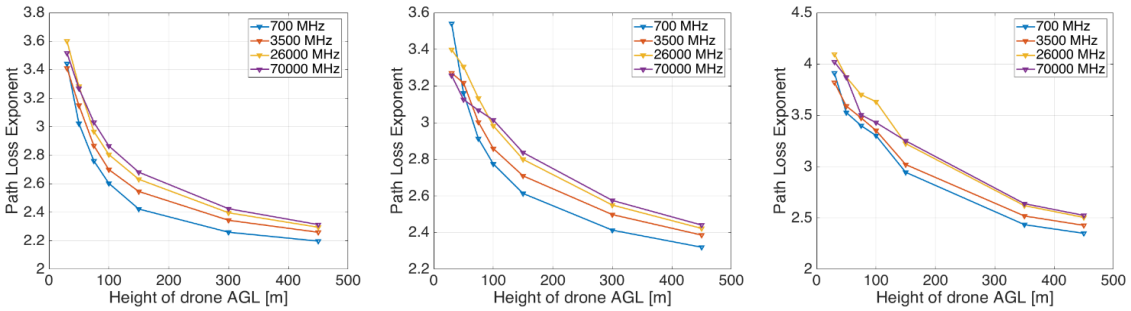

(a) Bologna (b) Munich (c) San Francisco

Figure 4-7: Path loss Exponent (PLE) using an isotropic antenna for three different cities, © 2021 IEEE

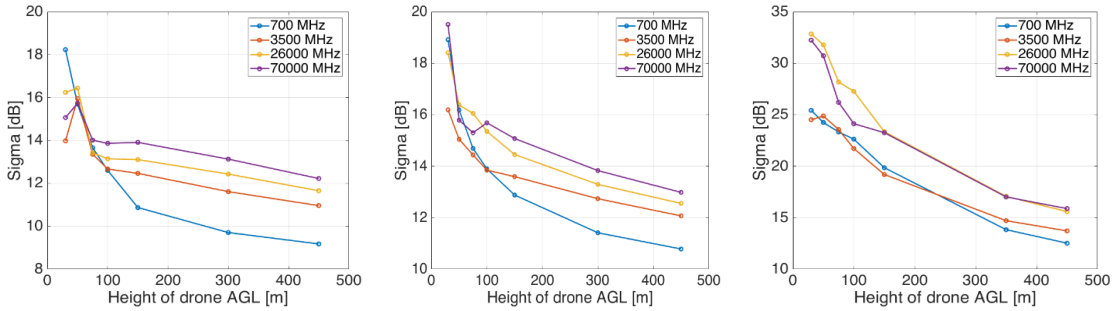

(a) Bologna (b) Munich (c) San Francisco

Figure 4-8: Sigma Shadowing using an isotropic antenna for three different cities, © 2021 IEEE

The achieved σ values as a function of the UAV flying altitude are reported in Figure 4-8. It is observed that σ also has a decreasing trend with height: the higher the UAV is flying, the lower the σ value is, since the effects of propagation at local level become negligible in favour of a wider covered area. The same Figure 4-8 shows the dependency of the shadowing component from frequency. This dependency seems to be more visible for the lower bands than for the higher ones, where the gap between 26GHz and 70GHz is again narrower.

Shadowing levels in Figure 4-8 look quite large compared to what usually assumed for wireless cellular networks, where σ hardly exceeds 10 dB in urban scenarios at UHF frequencies [52]. This difference can be related to the use of an isotropic transmitting antenna in dense urban contexts, where both line-of-sight conditions and heavily obstructed ground locations are likely to be simultaneously present, thus increasing the signal spread. This is especially stressed at lower UAV altitudes, where pathloss at the

locations in LOS is reduced by the limited distance, whereas it is instead particularly large at the heavily obstructed furthest tiles.

To achieve mathematical accuracy while keeping the necessary filtering on distance introduced in Section 4.3, it is vital to ensure that the maximum path loss in the ray launching model exceeds the values expected in the actual radio system [32] and for this reason it was necessary to account for slightly different values, namely PL_{max}=180 dB and 210 dB, for the case of San Francisco.

4.5.2 Directive Antenna

In this subsection, the UAV is then assumed to be equipped with a directional antenna of fixed aperture angle θ, placed under the UAV fuselage and pointing towards the ground, as introduced previously in Section 3.3.

In Figure 4-9– which refer only to Munich city and to only one frequency at 3500MHz for simplicity - it is possible to see respectively the trend of the path loss exponent α and the sigma shadowing σ as a function of the antenna aperture angle θ, ranging from 40° to 180°, and for different flight altitudes.

As a general trend, the increase in the antenna directivity reduces the size of the service area at ground, resulting in a greater LOS probability (Figure 4-4 (a) and (b)).

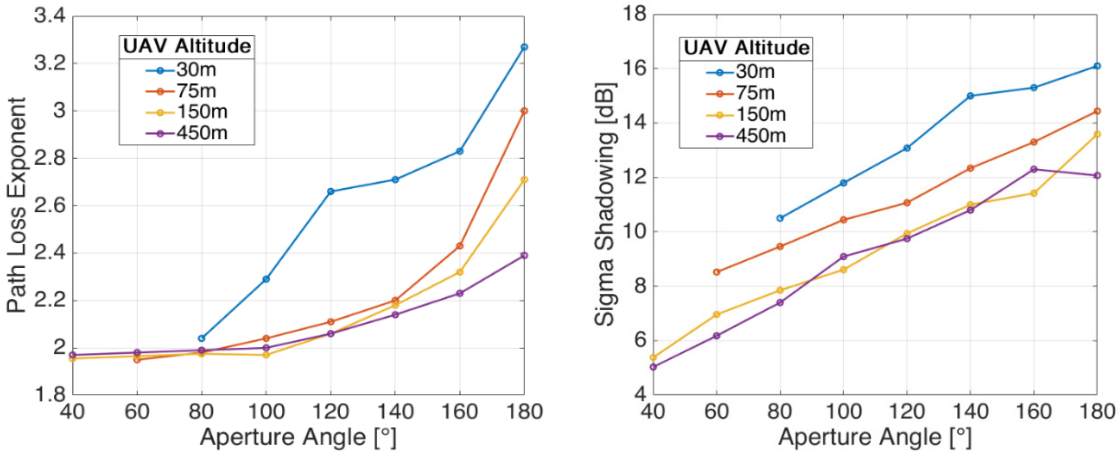

Figure 4-9: Path loss Exponent and Sigma Shadowing trend in Munich at 3500 MHz, © 2021 IEEE

The weaker average obstruction on the propagating paths results in the lower values of PLE in Figure 4-9, compared to Figure 4-7(b). At the same time, the extent of shadowing effects is also reduced, corresponding to a decrease in σ for decreasing antenna aperture values. It is interesting to report that for θ<80° the simulation samples available in this model are not statistically significant – i.e few points - at low UAV altitudes and do not lead to any calculation but – being already close to α=2 for the same θ value at higher altitudes – it can be reasonably extrapolate them as those in the free space since all the tiles within the antenna footprint happen to be in clear line of sight to the drone. This constraint does not exist anymore for higher altitudes, and statistical samples are available also for θ<80°. The more the antenna aperture angle increases – and thus the directivity decreases – the more both α and σ parameters tend to the isotropic case (corresponding to antenna beamwidth equal to 180° in Figure 4-9). From these trends at different UAV altitudes, it is possible to see that the higher the drone is flying, the lower both α and σ values tend to be. The same trend was observed for the other frequencies, also in Bologna and San Francisco, except for a different gradient which accounts in this study for the different urban environments and the different frequencies.

4.6. CONTRIBUTION OF MULTIPATH COMPONENTS

This section sheds some light on the different multipath components that contribute to the A2G propagation. It is known that the received power in a specific location (tile) is the result of different contributions: mainly one direct ray (when existing) and many indirect rays, which consist of multipath signal components generated by reflection, diffraction and diffuse scattering phenomena [66].

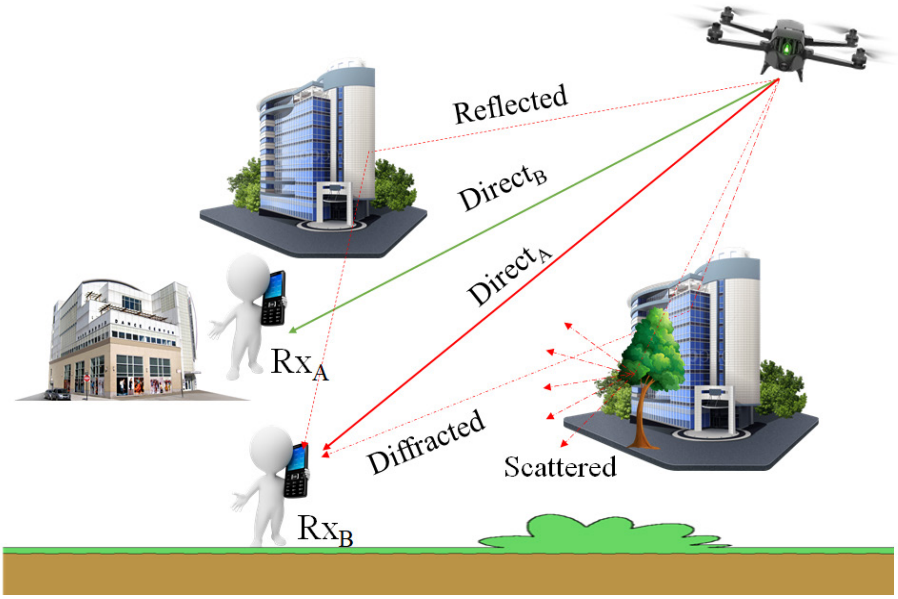

Figure 4-10: Air-to-ground propagation scenario with a UAV and two users (example). User Rx_A and Rx_B both receive the UAV signal but with different multipath contributions.

What has not yet been deeply investigated – and is actually difficult to measure during in-field measurements – is the way their percentage contributes to the final received signal (Figure 4-10). As an example, user Rx_A is in open space and in clear line of sight to the UAV, thus it receives a direct signal only (green arrow). User Rx_B is also in line of sight to the UAV but its path is masked by different buildings that generate different multipath components (red arrows). The reader is thus guided in the process of understanding the way the weights of this phenomena affect the received signal. Due to the relevant set of data, additional simulation results are attached in the APPENDIX.

4.6.1 Isotropic Antenna

By running several “single events only” simulations, i.e., enabling only direct rays or only diffracted rays or only reflected rays and so on, it is possible to evaluate the incoherent power contribution of each event - or combination of events, like 2 diffractions and 1 reflection, as an example - to the total received power, whose effects are approximated using simple geometric equation instead of Maxwell's wave equations [35].

To further investigate the A2G link, the analysis has been focused on the isotropic and directive antenna cases, bearing in mind the same ray launching configuration parameters as in TABLE 4-1.

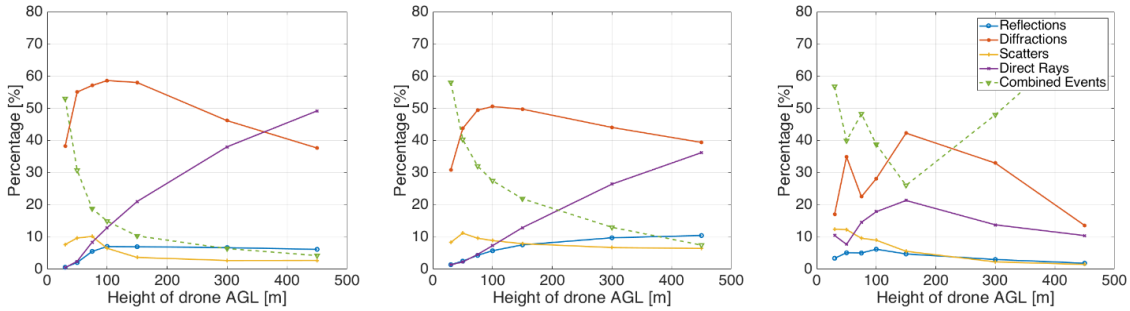

(a) Bologna (b) Munich (c) San Francisco

Figure 4-11: Multipath components at 700 MHz for three different cities using isotropic antenna, © 2021 IEEE

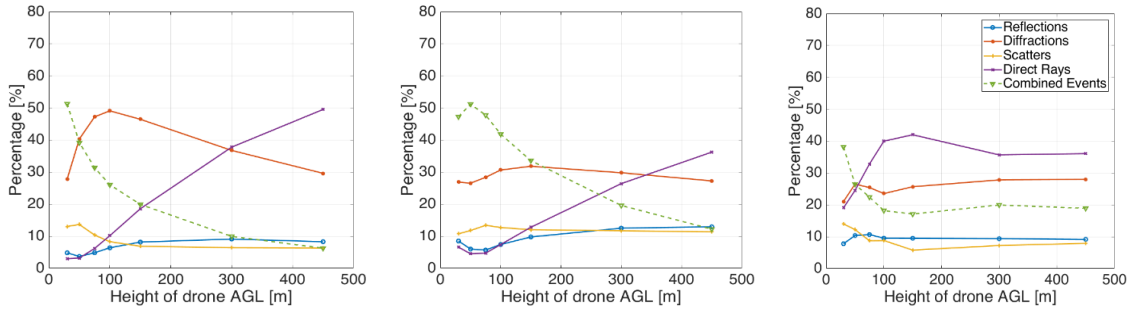

(a) Bologna (b) Munich (c) San Francisco

Figure 4-12: Multipath components at 3500 MHz for three different cities using isotropic antenna, © 2021 IEEE

At the lower frequency of 700 MHz (Figure 4-11), diffraction is the major propagation mechanism overall in case of isotropic antenna: as the UAV flying altitudes are always higher than the average building heights (TABLE 3-1) while single diffractions on the rooftop can convey significant power to most of the ground locations. Anyway, the lower the UAV height, the further the distance of the diffracted rays from their shadow sides; this may explain why A2G propagation better relies on combinations of different interaction at the lowest altitudes (Figure 4-11). In particular, combined events challenge the leadership with diffraction in San Francisco (Figure 4-11c), where hilly terrain and high-rise buildings can support propagation through mixed interactions along longer wireless paths.

This seems especially true at the higher altitudes, where the UAV has better visibility of the whole urban area, and rays experiencing few bounces on the taller buildings are likely to provide radio coverage almost everywhere. Not surprisingly, the strength of the LOS path increases with the UAV altitude to the detriment of diffraction relative weight (Figure 4-11a-b). This is not as much true in San Francisco (Figure 4-11c) where the high skyscrapers prevent LOS to dominate even at high flying altitudes and A2G link is mainly relying also on diffraction and combined events. Scattering as well as reflection alone contribute to the total received power to a relative extent always lower than 10%.

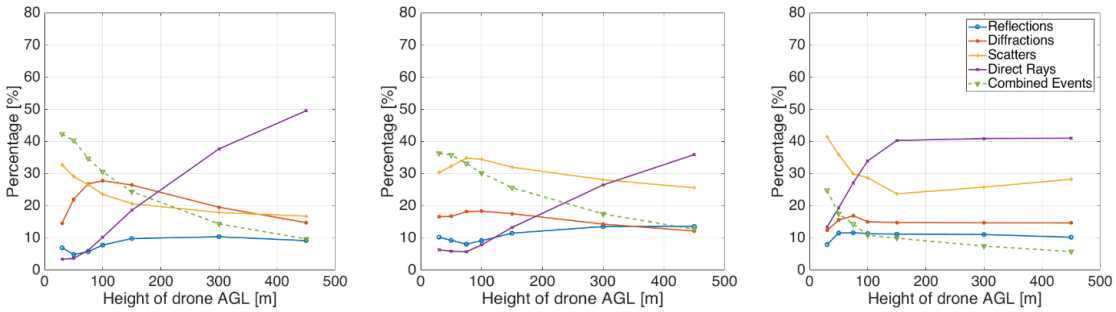

(a) Bologna (b) Munich (c) San Francisco

Figure 4-13: Multipath components at 26000 MHz for three different cities using isotropic antenna, © 2021 IEEE

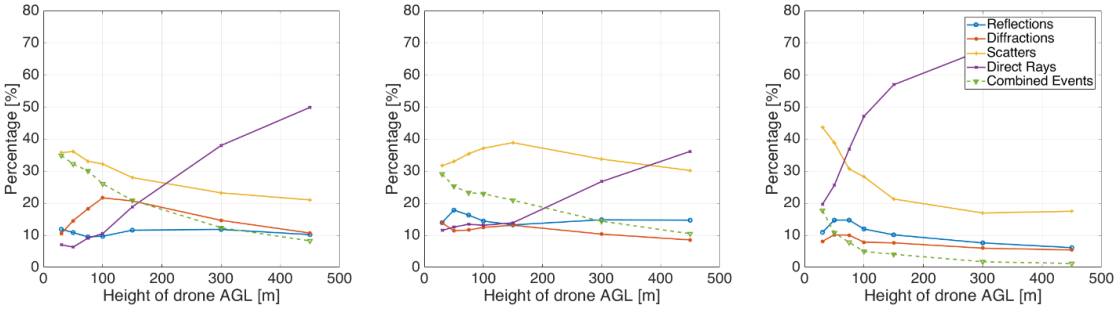

(a) Bologna (b) Munich (c) San Francisco

Figure 4-14: Multipath components at 70000 MHz for three different cities using isotropic antenna, © 2021 IEEE

At higher frequencies (Figure 4-13), power contributions from diffraction undergo a great reduction, that is of course physically sounded in case of isotropic antenna. Conversely, scattering rises to greater importance (20%-40% of the total), to the extent that it stands out as the major propagation interaction, at least at the lower flying levels. This

seems in contrast with the general statement that the millimetre wave channel is sparse and dominated by few powerful contributions commonly classified as reflections.

In this respect, it should be noted that:

i. A2G propagation is mostly happening in the longitudinal direction, perpendicular to the ground since the antenna is pointing downwards

ii. sparsity of the mm-wave channel has been mainly investigated indoor and with the antenna pointing parallel to the floor

iii. the scattering model embedded into the RL tool aims at modelling not only actual scattering from surface roughness, but also other multipath components – regardless of their specific nature – spread by the architectural and structural elements on the facades of buildings (i.e. balconies, pipes, windows frames, etc.) usually not included in the simulation input files for practical reasons. LOS power is still increasing with the UAV height and becomes remarkably uppermost at the higher altitudes.

It is also worth noting that up to few hundred meters in altitude, propagation seems never driven by the LOS contribution only, thus highlighting the need for multipath propagation models for the A2G channel.

4.6.2 Directive Antenna

The outcomes in case of a directive antenna are interesting as well and reported in Figure 4-15 and Figure 4-16, in good agreement with the research expectations. For the sake of simplicity and clarity, figures have been focused only on 700MHz and 26000 MHz, as significative representative frequencies for the low and high 5G bands.

Figure 4-15 and Figure 4-16 show the same trends discussed before but for a directive antenna with an aperture angle θ=100°, taken as a representative example. Not surprisingly, the LOS path in both cases is the predominant contribution with an outstanding value ranging between 55% and 60% along the different UAV altitudes, with peaks between 70% and 80% at low UAV altitudes. This result matches the trends

explained in previous sections, since most of the tiles within the antenna footprint are in clear line of sight. At the lower frequencies, diffraction supports propagation for a good 30% while it drops down to 10% at higher frequencies. Conversely, diffuse scattering is negligible with a contribution of around 5% at lower frequencies, while it stands up to around 20% at higher frequencies.

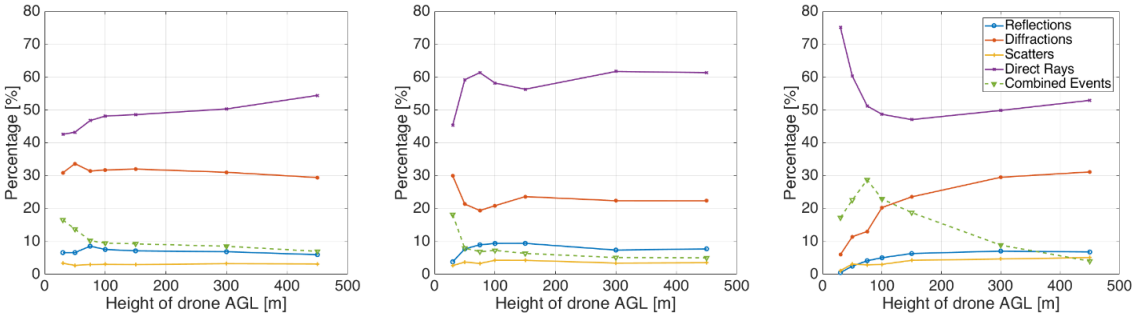

(a) Bologna (b) Munich (c) San Francisco

Figure 4-15: Multipath components at 700 MHz for three different cities using directive antenna θ=100°,© 2021 IEEE

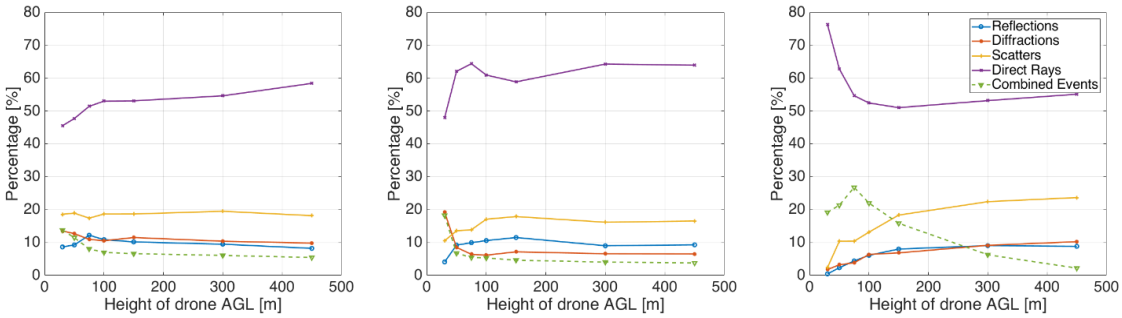

(a) Bologna (b) Munich (c) San Francisco

Figure 4-16: Multipath components at 26000 MHz for three different cities using directive antenna θ=100°, © 2021 IEEE

Remaining components – like reflections and any combination of them – are not remarkable, being well below 10% for most of the UAV altitudes and transmitting frequencies, similarly to the isotropic case seen in Figure 4-11-Figure 4-14.

CHAPTER 5. RADIO ENVIRONMENTAL MAPS FOR UAS

The fifth generation (5G) of mobile radio networks will dramatically increase the number of connected devices as well as the need for broadband connectivity and real time applications [67]. As a consequence, a higher density of connected devices will produce intuitively a larger standard deviation in the traffic type, content and the generation process: a network deployment based on average or peak traffic predictions will thus produce highly suboptimal results. Therefore, future networks will need to be much more flexible than in the past and they should be able to react smoothly and automatically to the fast time-space variations of any traffic demand. This can be achieved by moving the network infrastructure and by tailoring it according to actual traffic needs, as introduced in section 5.1 and detailed in section 5.2.

The system model behind this concept has been developed by the Radio Networks Teams at the University of Bologna and it is explained in section 5.3 while section 5.4 introduces the design phase, using this time the Radio Environmental Maps generated via RL as inputs to this joint research activity. Section 5.5 reports the main outcomes.

5.1. UNMANNED AERIAL BASE STATIONS AND REM

In the frame of UAV trajectory optimisation, many works related to Unmanned Aerial Base Stations (UABSs) assume free-space path loss propagation environment. This is a quite limitative assumption since the channel model may vary significantly depending on the location, especially in urban environments. Existing Air-To-Ground (A2G) models try

to capture the variations of the channel as a function of UABSs altitudes and angle to the users but are rarely tested and compared in practical scenarios. Previous works propose a possible approach to employ Radio Environmental Maps (REMs) in UAV-networks planning [68], but only with a simple and parametric emulation of radio maps.

To further enrich the research activities, Ray Launching (RL) simulations were used this time to investigate the performance of a heterogeneous network made of both Terrestrial Base Stations (TBSs) and UABSs by providing a database of coverage maps of the mission critical urban environment. The key task of this joint research activity was to compare the emerging technique in the use of REM generated by RL with common – statistical - channel models. The communication channels investigated are both the TBS-user and UABS-user links, the latter being the A2G model.

5.2. REFERENCE SCENARIO

To include proper RL estimations in the model and define the service area, it was necessary to use a real map of an urban city. In this case, it was selected the city centre of Bologna, Italy, since immediately available from previous research activities. The TBSs locations are emulated starting from the actual UMTS/LTE network deployment, with a total of NTBS legacy BSs. The UABSs are initially parked in one of the TBSs, and this location becomes the starting point of their mission. Both BS types operate as a 5G network system with carrier frequency f_c=3.5 GHz, where Radio Resources (RRs) are organised in Physical Resource Blocks (PRBs) and frames of 20 s. The maximum capacity per frame is 7.2 Mbps. The values of the scenario parameters are presented in TABLE 5-1.

TABLE 5-1: SCENARIO AND NETWORK PARAMETERS, © 2020 IEEE

Parameter Definition	Value
N_{TBS}	36
v	20 m/s
B	200 MB
S_{min}	100 Mb/s

T_W	15 s
f_c	3.5 GHz
TBS bandwidth	100 MHz
Subcarrier spacing	30 kHz
Number of subcarriers in each PRB	12
Minimum SNR value for connection	10 dB
Transmit power of TBSs	36 dBm
Antenna gain of TBSs	12 dB
Transmit power of UABSs	10 dBm

5.2.1 Traffic Model and User Distribution

To comply with RL simulations, users are randomly distributed in the outdoor space of the city centre with a mean density λ. It is assumed that users in the area are asking for a video download of size B, that has a minimum throughput requirement denoted as S_{min}. Moreover, each user is willing to wait a maximum time T_W, otherwise it leaves the network. As commonly seen in the literature, it is again assumed that the UABSs can estimate users' locations through network information. The RL and network simulations map is also shown in Figure 5-1, together with the TBSs placement.

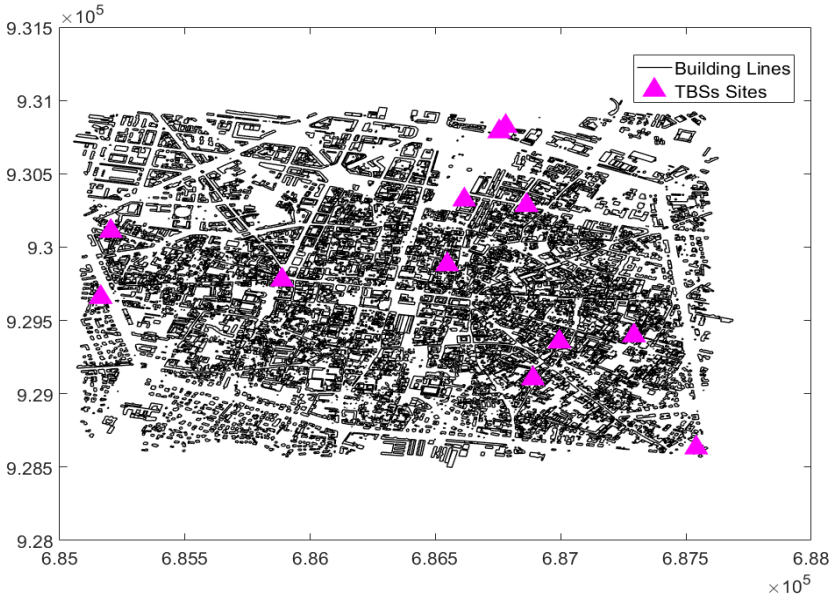

Figure 5-1: Bologna city centre, urban environmental 3D model including base stations, © 2020 IEEE

5.2.2 UABS Antenna System

For the purpose of this analysis, UABSs were equipped with a directional antenna pointing perpendicular towards the ground, with a fixed aperture angle θ. This angle θ is the same as previously introduced in section 3.3. The UABS antenna gain is assumed to depend on θ according to $G_\theta = 29000/(\theta)^2$. A 3 dB gain was added in order to account for a minimum level of gain even when θ is very large. Therefore, it is possible to state that the larger the UAV altitude, the larger the footprint. Consequently, the number of users that can be served by the UABSs (i.e., within its footprint) might increase. On the other hand, by fixing h, the larger is the angle θ, the larger is the footprint and the smaller is the antenna gain (Figure 5-2).

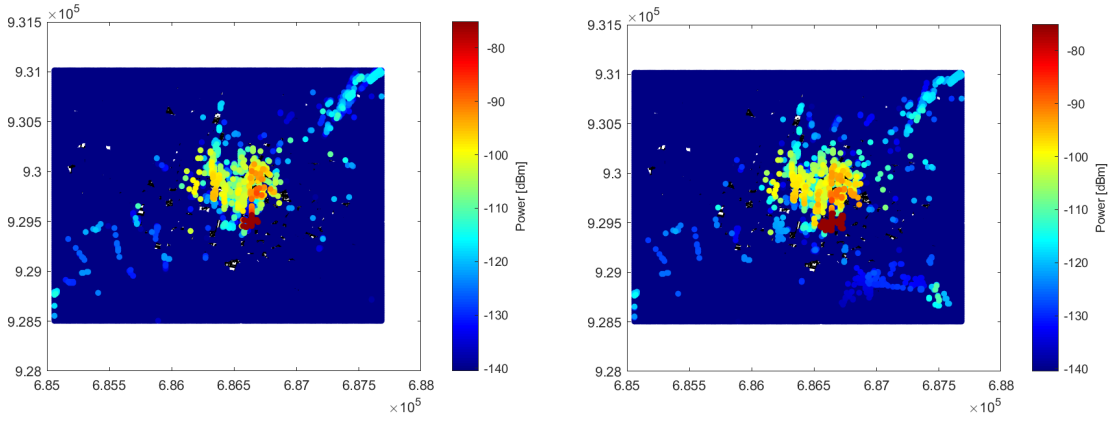

(a) h=75 m, α=80 (b) h=100 m, α=80.

Figure 5-2: Coverage map over Bologna city centre, examples at 3.5GHz, © 2020 IEEE

5.2.3 Statistical Channel Model and Data rate

Received power, P_{rx}, is computed as a function of the transmitted power P_{tx}: $P_{rx}[dBm] = P_{tx}[dBm] + G_{tx}[dB] - L[dB]$. Then, to investigate the propagation comparison, the channel loss $L[dB]$ is computed through RL. For what concerns the user links with TBSs, the channel model is the one used in [68], with a propagation coefficient of 3.6 and a shadowing variance of 6 dB. For the A2G link, the propagation model is based on the one described in [69] for an urban environment. According to this model, connections between drone and ground users can either be LOS or Non-Line-Of-Sight (NLOS). When the connections occur in NLOS, the signals travel in LOS before interacting with objects

located close to the ground, which results in shadowing effect. One further assumption is that UABSs can estimate the loss of a link before reaching it. This is not needed in the case REM are available, because it refers to a database that is known *a priori*.

5.2.4 Deterministic Channel model and RL Simulations

The additional simulation parameters, specifically set for the RL in order to interface the network simulator, are shown in TABLE 5-2. The database generated after multiple RL runs is made of a set of REMs calculated on each of the 1156 drone positions, which ensure thus the reliability of the constructed REMs, minimising the need for any spatial interpolation [70] due to an average distance of around 70 m between each consecutive drone position, enhancing the accuracy of the database on one hand, but increasing the complexity on the other hand.

TABLE 5-2: PARAMETERS FOR REM GENERATION

Parameter Definition	Value
Frequency	3.5 GHz (single)
Altitude	{50, 75, 100} m AGL
Drone Position	distributed square grid of 1156 points

5.3. SYSTEM MODEL

In the service area, users may be served by either the TBSs or UABSs. This is possible because it is assumed continuous communication between the network orchestrator and each BS in the control plane. The selection of the best server and Radio Resource Management (RRM) is made following principles of fairness and network throughput increase. For example, the orchestrator chooses the best server for a user depending on the strongest link in terms of PL or selects the nearest UABS if neighbouring TBSs are

overloaded by the high traffic demand. Then, the RRM is made with a Round Robin algorithm, followed by Proportional Fair if spare radio resources are present.

5.4. UABS TRAJECTORY DESIGN

The dynamic trajectory design follows the algorithm proposed in [71] and further details can be found in [72]. The cost function C_i is computed as:

$$C_i = \frac{d_i}{d_{th}} \cdot \frac{\delta_i}{\delta_{\max}} \cdot \frac{W_i}{W_{\max}} \cdot \frac{S_{\min}^{(cl)}}{S_i^{(cl)}} \cdot (1 + B) \qquad (6\text{–}1)$$

where d_i and δ_i represent the distance of the *i-th* centroid to the drone and the user density, respectively. d_{th} and δ_{max} are normalizing factors with the maximum value of distances and densities, respectively. Further, the fraction $\frac{W_i}{W_{\max}}$ accounts for the resource reuse, where W_i are the RRs already used by the TBSs under the UAV coverage area and W_{max} normalises the factor with the maximum available.

The fraction $\frac{S_{\min}^{(cl)}}{S_i^{(cl)}}$ considers the estimated Sum Throughput (ST) obtained in the *i-th* centroid $S_i^{(cl)}$. $S_{\min}^{(cl)}$ is the minimum throughput achievable in the current set of identified clusters. The term (1+B) provides spatial fairness.

It is important to note that the ST is obtained by computing the link budget and PL of every user to its BS. Therefore, when a statistical model is employed to compute the A2G PL, the ST is an estimation from the given formulation (Section 5.2.3). Conversely, when the RL database is employed, actual loss is retrieved from the PL sample corresponding to the user position. For this reason, it can be effectively stated that the trajectory planning is based on a REM knowledge. It should be noted that the PL samples – stored in a database - are always updated in time with regards to the UABS and users' positions. Therefore, the REM accuracy is based on the discretization of the UABS possible positions in the map of the service area and the variations of fast fading.

5.5. SIMULATION RESULTS AND DISCUSSION

The metric chosen for the analysis of the results is the network throughput gain G, computed following Eq. (6-2):

$$G = \frac{S_{UABS}}{S_{tot}} \qquad (6\text{–}2)$$

The terms S_{UABS} and S_{tot} represent the sum of the users' throughput obtained by the UAV only and by the entire network respectively, that is when both TBSs and UABSs are considered. This, together with the percentage of served users in the service area, lead to represent the network Key Performance Indicators (KPI). Subsequently, performance is computed to study the difference between channel estimation through known models and vs. a previously calculated value of PL over a REM database. Note that PL evaluations influence not only the channel gain for each user but also the UABSs' trajectory design through sum throughput estimation. The cluster cardinality K is not given as a fixed value but computed depending on the network load. In fact, it holds $K=N_{uu}/N_{uc}$, where N_{uu} is the number of unsatisfied users and N_{uc} represents the average number of users per cluster for each time unit.

The main outcomes of this research activity on trajectory optimisation are summarised in the following two figures, Figure 5-3 and Figure 5-4, which simulate a traffic load where an average number of more than 3000 users are asking for service.

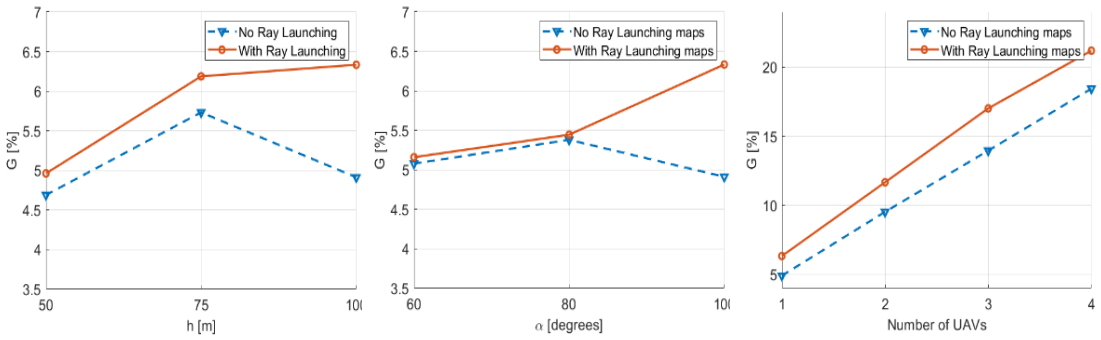

(a) Varying altitude (b) Varying aperture angle (c) Increasing number of UABSs

Figure 5-3: Throughput gain of a flying UABS while varying UABS parameters, © 2020 IEEE

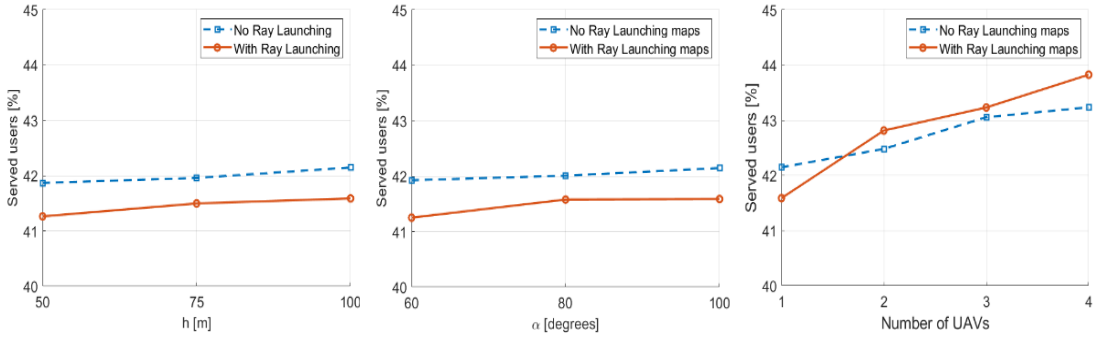

(a) Varying altitude (b) Varying aperture angle (c) Increasing number of UABSs

Figure 5-4: Percentage of served users while varying UABS parameters, © 2020 IEEE

These pictures include two curves representing the simulation results for the different channel models. Figure 5-3 shows the network performance in terms of throughput gain, while Figure 5-4 in terms of the percentage of served users within the service area, when both TBSs and drones are available.

In general, Figure 5-3 is the set of plots proving a higher difference in performance between the two computations for channel propagation. In particular, it is possible to see up to 1.5% throughput gain improvement in network performance while varying both aperture angle and UABS height. Moreover, in the case of multiple UABSs, the gap between the two model results increases the gain of up to 5%. This is reasonable because the increased number of links in the network, due to more aerial stations, sharpens the difference.

In all simulation runs, the statistical model provides the worst-case scenario, but the trend of the two curves is similar except for small (with respect to the absolute value) statistical variations. This result shows that, as expected from a correct RL development and a fair statistical ATG channel, the two applied propagation models behave in a comparable manner. Having the same network trend also proves the implementation accuracy, as a similar network behaviour was anticipated.

One may also note the maximum created by simulation with statistical models in Figure 5-3 a) and b). While a maximum for the altitude was expected because of the trade-off between distance and LOS probability, one for the aperture angle was not. In this case, statistical models indicate an optimal trade-off in choosing both the altitude and the

radiation angle, that the RL model shows it is not applicable for the scenario of Bologna city centre. This trade-off should be instead with different values, and the results from statistical models may be misleading and altering the network planning made by a mobile operator. However, please note that the metric analysed here is in terms of overall network throughput, which is not a fairness metric among different users, but helps in understanding the efficacy of the system model versus applied costs.

CHAPTER 6. PRELIMINARY EXPERIMENTAL MEASUREMENTS

This chapter is aimed at investigating the characterization of low-altitude A2G propagation in urban areas, as introduced in section 6.1 - where the presence of buildings has a strong impact on propagation, as already anticipated in the previous chapters via simulations. This is achieved by means of a test bench described in section 6.2 and real measurements, outlined in section 6.3 and section 6.4, with focus on the channel characteristics at two mm-wave frequencies - 27 and 38 GHz - that are quite popular for having been recently allocated to 5G systems. Measurements have been carried out - and related in-field data collected - during the few available time slots after the 2020 Italian national lockdown period for COVID-19 and for this reason trials cannot be considered as extensive.

6.1. CHALLENGES IN REAL MEASUREMENTS

Several experimental investigations have been carried out for the characterization of air-to-ground (A2G) propagation, especially in the last few years [66]. Among the recent studies, several of them addressed rural or open-field propagation [73] [74] while only few have actually addressed A2G propagation in urban areas [75]-[77], most probably due to the intrinsic difficulties in flying a UAV. In such studies, the analysis is mainly focused on large-scale parameters such as path-loss, fading statistics and spatial correlations.

Existing studies – including those carried out in university campuses - are limited to UHF or sub-mmWave frequencies, and to the best knowledge, none of them investigated

the double-directional characteristics of the A2G channel, probably due to the problems related to mounting and operating directive antennas. Nevertheless, directive antennas at mm-wave frequencies can be relatively small and thus can help to overcome power-budget limitations typical of UAV-aided communications. However, a thorough knowledge of the directional characteristics of the channel at both link-ends will be required to design and operate such systems.

Of the many possible locations to run the trials and the experimental measurements, it was decided to select (Figure 6-1):

- A country cottage in *Mongardino* village, near Bologna for Outdoor to Indoor (O2I) measurements. Not only the cottage belongs to the University of Bologna, and thus it minimises the need for authorisations, but it also ensures minimum risk for people around during UAV mission since the area is not well inhabited.
- A residential area in *Imola* city, with a specific street full of buildings for Roof to Street (R2S) measurements. This street, although placed among a maze of residential roads, can be easily closed during the UAV mission while ensuring to the pilot full sight control of the UAV operations.

Figure 6-1: Map of Northern Italy, Bologna and Imola locations (blue dots)

6.2. TOOLS AND INSTRUMENTS

Air-to-ground channel measurements have been carried out in an urban environment (Figure 6-2) at millimetre frequencies. In the frame of this PhD thesis only preliminary

results at mm-wave frequencies - 27 GHz and 38 GHz - will be reported since revisions are still in progress and some measurements might need to be repeated, adjusted or simply to be confirmed by further runs due to some unusual reported behaviours.

Figure 6-2: UAV flying in front of building blocks during the different research missions

The experimental equipment was made of an air- and a ground-station (Figure 6-3), shortly outlined in the following subsections.

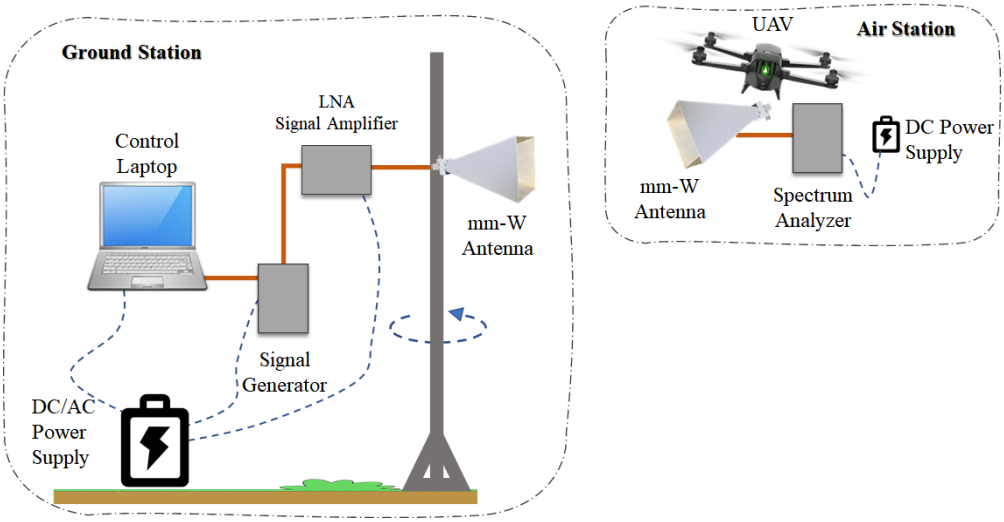

Figure 6-3: Measurement set-up, mobile or fixed configuration

Some information about the UAV piloting features and the software tools for data processing are also included in the following subsections 6.2.1 - 6.2.3

6.2.1 Air-station

The air station is made of a custom quadcopter equipped with a GPS plus Real-Time Kinematic (RTK) localization/navigation system, a specular link-end including a directive horn antenna and a mm-wave portable spectrum-analyser, while an automatic gimbal is used on the same UAV for 3D steering capabilities (Figure 6-4). The UAV clearly represents the backbone of the air-station. The quadcopter drone has a maximum weight of 4 kg (including measurement setup), specifically conceived and customized for wireless channel measurement. The four rotating propellers are supplied by 380W electric motors placed at the corners of the UAV structure. Both the propellers and the drone frame are made of carbon fibre to reduce weight while granting sufficient mechanical strength. A metal slid is present on the bottom side to let the UAV safely rest on ground, whereas the top side hosts the telemetry and the remote-control units and the GPS receiver. Real Time Kinematic (RTK) can be enabled in order to increase positioning accuracy. Electrical motors and the other devices are supplied by 6s Li-Ion batteries, corresponding to a maximum flight time equal to about 20 minutes.

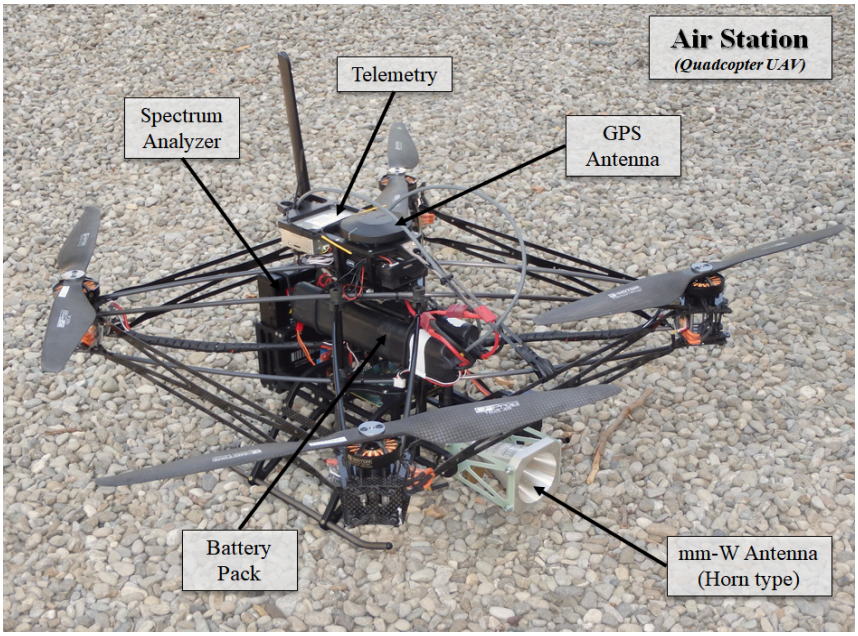

Figure 6-4: Air Station, including details

On-board equipment for millimetre-wave communications consists of a SAF Tehnika J0SSAP14 compact spectrum analyser (SA) operating in the 24-40GHz band with a sweep

speed of 0.5 s at a 100MHz span [78]. Received signals are provided to the SA by either a conical horn or an omnidirectional antenna, with gain respectively equal to 21dB and 3dB. The elevation of the directive antenna can be automatically set and controlled by means of a servocontrol. The total weight of the mm-wave equipment amounts to about 0.5 kg. The mm-wave SA is powered by dedicated batteries to save the drone battery life.

6.2.2 Ground Station

The ground station (Figure 6-5) consists of a mobile cart with an antenna and a mm-wave generator. Antenna is rotated in the azimuth or elevation planes at the ground station using a rotating positioner, according to the specific trial in progress. While the antenna is of a directive type (i.e. horn antenna) on board of the drone, the antenna on the mobile/fixed ground station can be either directional or omnidirectional. It is up to the specific trial in progress to drive this choice. At ground level, the millimetre-wave link is completed by a SAF Tehnika J0SSAG14 compact signal generator (SG), with a maximum output power equal to 5dBm [79]. The intensity of the transmitted signal is then boosted by means of a SAGE Ka-band power amplifier having a gain equal to about 20dB. Depending on the specific need, the amplifier can feed the same antennas already introduced for the air station.

Figure 6-5: Mobile cart, equipped with omni-antenna, laptop, signal generator and power supply

In order to carry out directional channel measurements, the horn antenna can be steered in the azimuth domain by means of a software controlled Yaesu g-450 rotating positioner.

A power inverter connected to a 24V car battery provides the ground equipment with the necessary power supply.

6.2.3 Control firmware and data processing

Although a pilot must be always present in clear sight of the UAV for safety reasons, the UAV flights have been planned beforehand by means of the "QGroundControl" application [80]. Every flying mission basically consists of a sequence of "waypoints" the UAV moves to and hovers on, plus a list of target points to steer the horn antenna towards, when needed. At the end of each mission, the flight data – including the temporal variations in the UAVs position and steering direction – are available in a specific telemetry file. In order to match the different UAV position/pointing with the measured received signal strength intensity, both the SA and the drone control boards are synchronized to the Coordinated Universal Time.

Finally, propagation markers like power angle / delay profile, angle and delay spread, blockage loss, path loss exponent etc. can be extracted from the measured and telemetry data by means of ad hoc Matlab scripts.

6.3. OUTDOOR TO INDOOR PROPAGATION

A great benefit of UAV-Assisted wireless networks against terrestrial mobile networks is the absence or reduced impact of shadowing for high elevation angles, i.e high flying altitudes. Based on this, it is obvious that UAV-Assisted wireless networks can be successfully used for urban outdoor coverage. However, there is a question of whether they can also provide mobile or wireless services inside the buildings, i.e when the user is no longer walking or standing in the streets - as assumed so far.

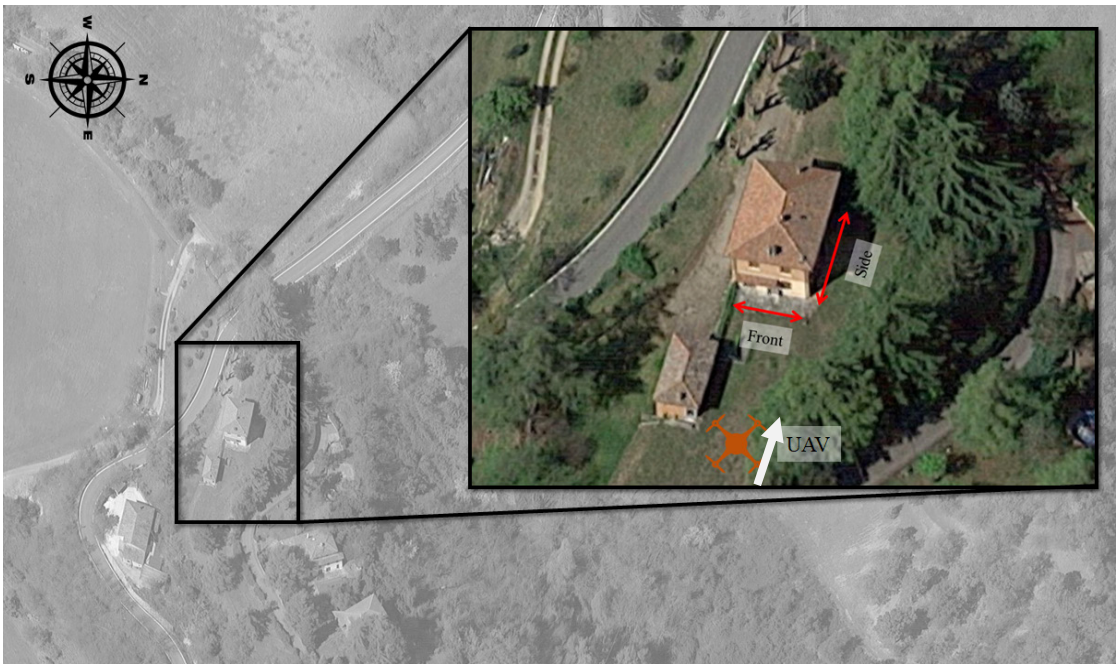

Figure 6-6: Country cottage in Mongardino – Bologna, used for O2I measurements. The white arrow shows the direction of transmission from the UAV towards the front of the building.

Figure 6-7: External view of the cottage in Mongardino. Dashed lines and label identify the path followed by the ground station on the cart. Please note that checkpoints A/F and B/E are on the side directly hit by the UAV signal.

To this end, it was interesting the evaluation of the Building Penetration Loss (BPL). The penetration loss is usually defined as the difference between the mean signal strength received outside at the foot of the building and the mean signal strength inside the same building. To collect the necessary measurements, the air station was hovering and transmitting around 30 m from the front wall ("far drone" label) of the building and at a height of 30m AGL, as seen in the previous pictures.

The ground station, equipped with an omnidirectional antenna, scanned the perimetral walls of the building (very close to the walls) forwards and backwards, on the loop around the building from checkpoint 'A' to 'C' and from 'D' to 'F'. The same path was followed for 27 GHz and 38 GHz transmitting frequencies. To acquire more data related to drone distance and elevation angle with regard to the building, the air station was then moved closer, to around 15 m ("near drone"), and the same measurements were repeated again. Figure 6-8 and Figure 6-9 show the received signal strength (RSS) in dBm as function of time/sample.

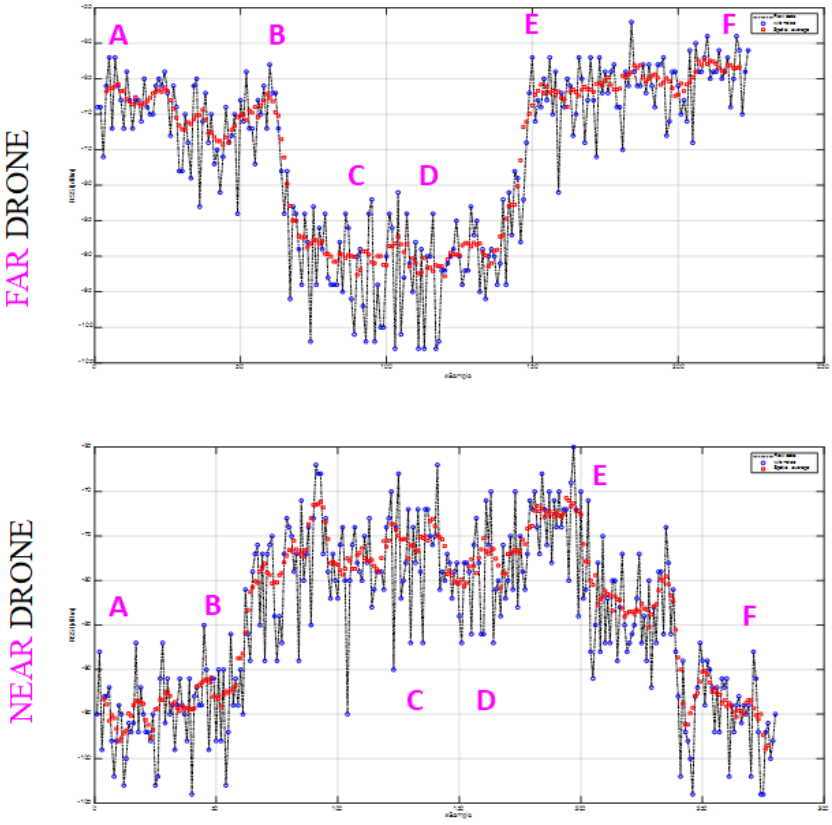

Figure 6-8: Received Outdoor power levels (RSS in dBm) at 27 GHz vs. time/sample

By cross-referencing the UTC time to the actual position of the ground station cart, it was possible to provide markers on the same figures to better identify the position with respect to the building. By reading the same figures it is possible to see the way the cart moved from one checkpoint end ('A') to the other one ('C) and then the way it came back (from 'D' to 'F') while the drone was far away from the building. Similarly, the same route was repeated while the drone was closer to the building. Blue dots represent the power samples connected by a dashed black line; red dots represent the trend as averaged by a moving window of 6 consecutive points. Although not expected, differences reported in received outdoor power levels between the front (checkpoints A/E, B/F) and the side of the building (C/D) seem to be mainly related to the "Far/Near" drone positions. There appear to be some anomalies that should be further investigated, also in accordance with the actual position of the drone and the radiation diagram of the antennas which should be both checked and confirmed in the next measurement runs.

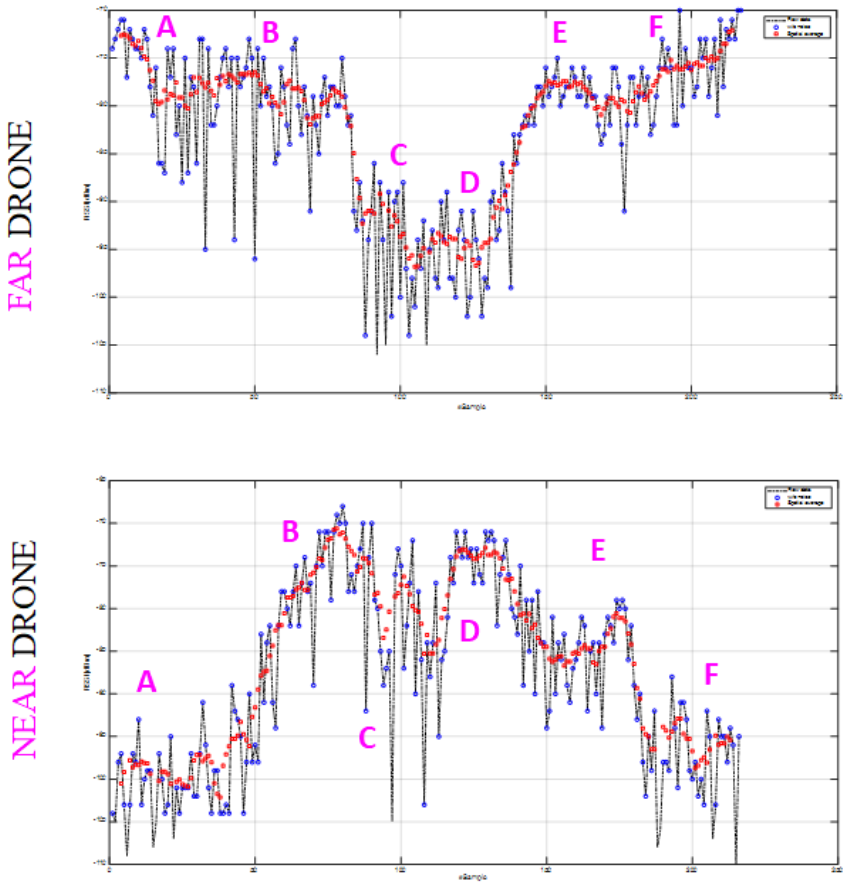

Figure 6-9: Received Outdoor power levels (RSS in dBm) at 38 GHz vs. time/sample

The following two tables summarise the collected data, statistics and values for the outdoor measurements:

TABLE 6-1: STATISTICS FOR OUTDOOR RECEPTION (FAR DRONE)

FAR DRONE	**27 GHz**	**38 GHz**
Nr. of samples	224	217
Overall mean value (noise incl.)	-67,67	-77,65
% of values > noise (-105dBm)	100	98,6
Mean value (after denoising)	-67,67	-77,59
Mean value (after spatial filtering) [dBm]	-67,8	-77,66

TABLE 6-2: STATISTICS FOR OUTDOOR RECEPTION (NEAR DRONE)

NEAR DRONE	**27 GHz**	**38 GHz**
Nr. of samples	280	216
Overall mean value (noise incl.)	-77,14	-78,57
% of values > noise (-105dBm)	100	95,37
Mean value (after denoising)	-77,14	-78,37
Mean value (after spatial filtering) [dBm]	-77,66	-78,45

The same ground station cart was then moved inside the building, around the first floor. Data were collected again starting from the kitchen, then moving to the bedroom and finally stopping in the living room. The first-floor plan and pictures of the three rooms can be seen in Figure 6-10 and Figure 6-11 respectively.

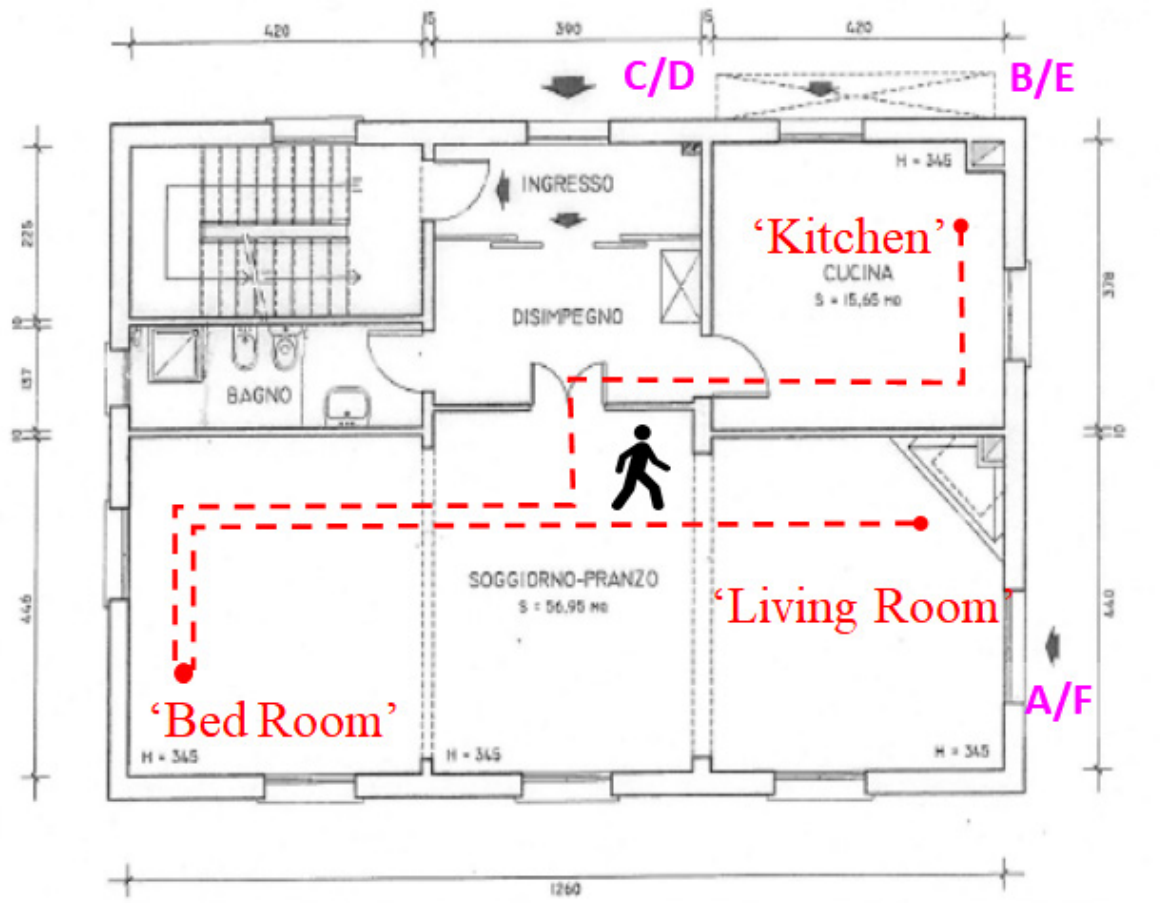

Figure 6-10: House plan, first floor – including route and checkpoints

Figure 6-11: Living room (left-hand side), kitchen (centre) and bedroom (right-hand side) on the first floor

Figure 6-12 and Figure 6-13 show the received signal strength (RSS) in dBm as function of time/sample. By cross-referencing the UTC time to the actual position of the ground station cart, it was possible to provide markers to identify the rooms. Again. by reading the same figures it is possible to see the way the cart moved from one end ('Kitchen') to the other one ('Living room') and then the way it came back (from 'Living Room' to 'Kitchen') while the drone was far away from the building. Similarly, the same

route was repeated while the drone was closer to the building, thus increasing the elevation angle.

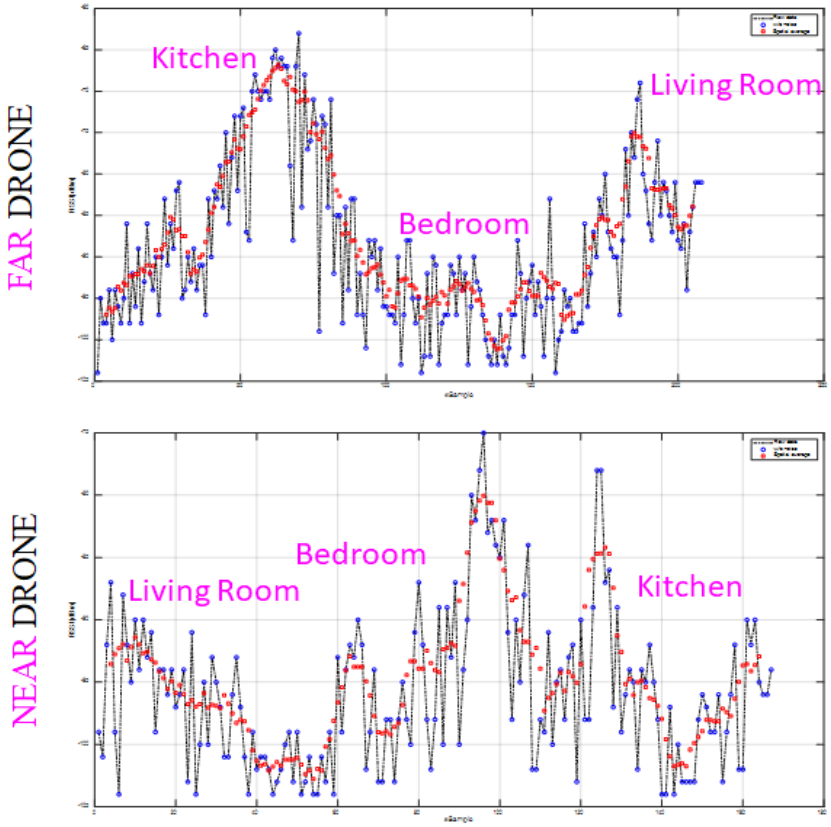

Figure 6-12: Received Indoor power levels (RSS in dBm) at 27 GHz, First floor vs. time/sample

TABLE 6-3: STATISTICS FOR INDOOR RECEPTION (FAR DRONE) – FIRST FLOOR

FAR DRONE	**27 GHz**	**38 GHz**
Nr. of samples	208	161
Overall mean value (noise incl.)	-77,14	-91,55
% of values > noise (-105dBm)	100	77,6
Mean value (after denoising) dBm	-77,01	-90,48
Mean value (after spatial filtering) [dBm]	-77,59	-91,95

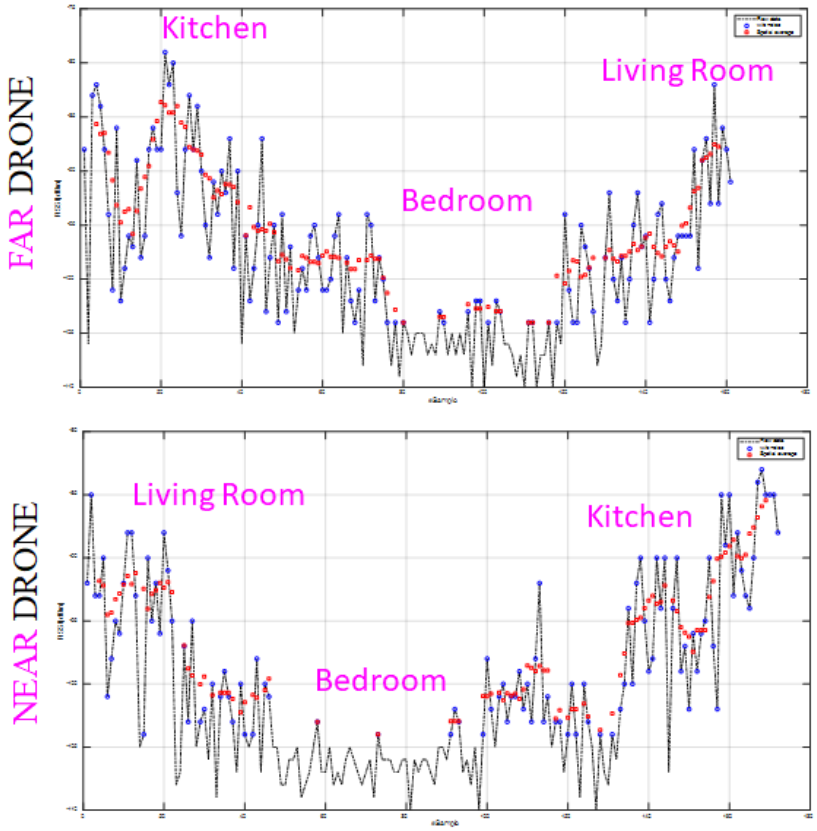

Figure 6-13: Received Indoor power levels (RSS in dBm) at 38 GHz, First floor vs. time/sample

TABLE 6-4: STATISTICS FOR INDOOR RECEPTION (NEAR DRONE) - FIRST FLOOR

NEAR DRONE	**27 GHz**	**38 GHz**
Nr. of samples	167	172
Overall mean value (noise incl.)	-89,61	-94,33
% of values > noise (-105dBm)	100	61,62
Mean value (after denoising) dBm	-89,61	-92,34
Mean value (after spatial filtering) [dBm]	-90,67	-95,13

The ground station cart was then moved to the second floor where a similar room layout was found as it can be seen from Figure 6-14 and Figure 6-15.

Figure 6-14: Bedroom (left-hand side), Balcony (centre) and studio (right-hand side) on the second floor

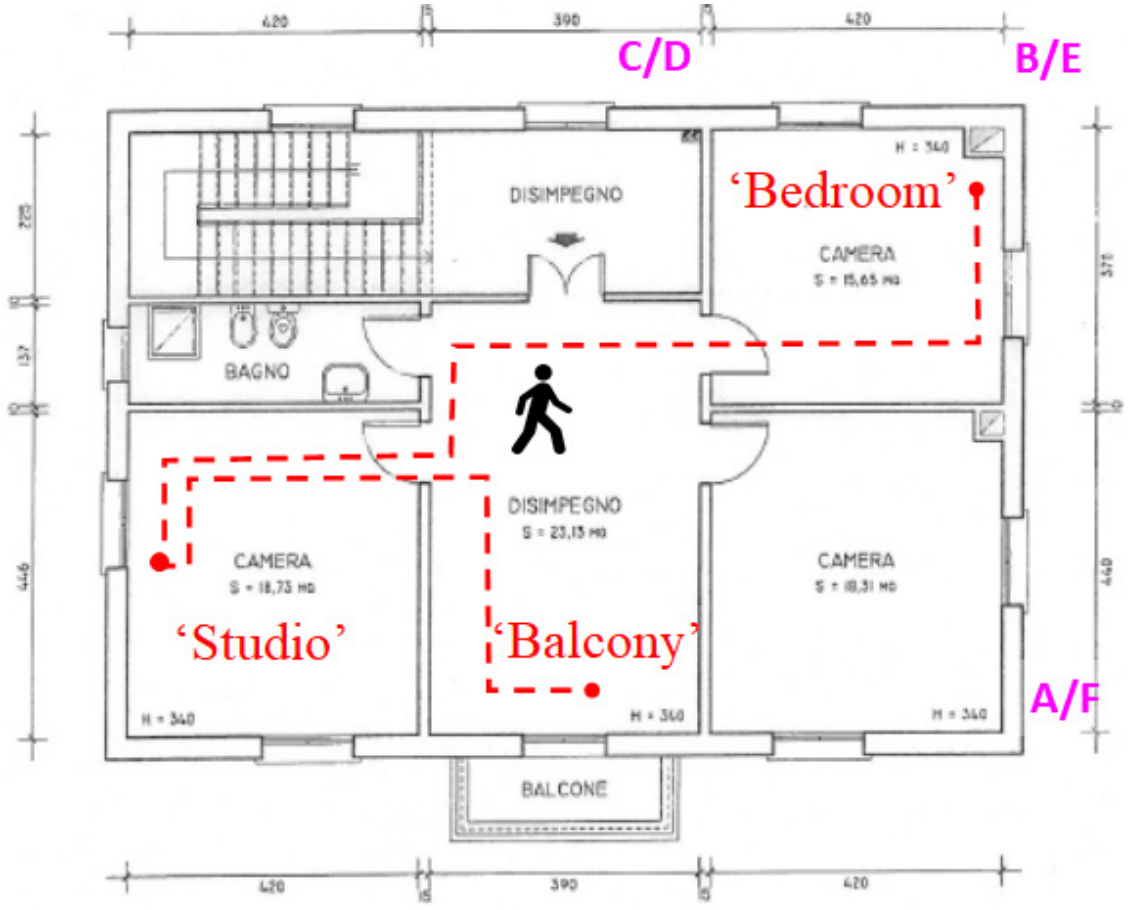

Figure 6-15: House plan, second floor – including route and 1st floor checkpoints

The following two tables summarise the collected data, statistics and values for the indoor measurements:

TABLE 6-5: STATISTICS FOR INDOOR RECEPTION (FAR DRONE) - SECOND FLOOR

FAR DRONE	**27 GHz**	**38 GHz**
Nr. of samples	180	159
Overall mean value (noise incl.)	-79,93	-80,82
% of values > noise (-105dBm)	80	75,42
Mean value (after denoising) dBm	-78,97	-79,60
Mean value (after spatial filtering) [dBm]	-80,26	-80,3

TABLE 6-6: STATISTICS FOR INDOOR RECEPTION (NEAR DRONE) - SECOND FLOOR

NEAR DRONE	**27 GHz**	**38 GHz**
Nr. of samples	186	192
Overall mean value (noise incl.)	-84,80	-98,19
% of values > noise (-105dBm)	88	68,23
Mean value (after denoising) dBm	-84,25	-96,76
Mean value (after spatial filtering) [dBm]	-84,94	-97,4

The following tables show the preliminary BPL calculated for two different drone positions and two different frequencies.

TABLE 6-7: BPL FOR "FAR DRONE" CONDITION

FAR DRONE	**27GHz**	**38 GHz**
BPL @ First Floor [dBm]	9,79	14,29
BPL @ Second Floor [dBm]	12,46	N/A (*)

TABLE 6-8: BPL FOR "NEAR DRONE" CONDITION

NEAR DRONE	**27GHz**	**38 GHz**
BPL @ First Floor dBm	13,01	16,68
BPL @ Second Floor dBm	7,28	N/A (*)

(*) Not Available

While most of the preliminary results at 27 GHz seem to be going in the direction of the outcomes in [82] and thus can be accepted with a reasonable confidence level, results at 38 GHz on the contrary might be misleading and need further investigation and understanding. Pending points to be clarified are related to the BPL differences between the two frequencies as well as the ones between the two cottage floors. In case of "FAR" drone, the BPL value at the second floor makes no sense and it is so far "Not Available" (N/A). Similarly, in case of "NEAR" drone, the same BPL shows a value outside the expected range and against any theoretical prediction, with the need to be sooner repeated. At the same time, the actual dependency of the BPL as a function of the drone and mobile cart positions should be also investigated. A possible – preliminary – explanation that might justify the many differences among the various path loss could be due to low elevation angles, where there is a high probability that the signal is getting across more walls inside the building (or through the roof), together with the specific radiation diagram coming from the air/ground antennas in conjunction with other minor propagation effects

related to the higher frequency range. While waiting for the trials to be repeated at a better time, both BPL values have not been included in TABLE 6-7 and TABLE 6-8.

6.4. ROOF TO STREET PROPAGATION

In this scenario, represented in Figure 6-16 and Figure 6-17, the drone is hovering above streets and buildings of Imola, Italy at a fixed position, with the RX horn antenna oriented towards the centre of the street canyon, while the ground station with TX is placed on the farther side of the street canyon: the LOS path is therefore obstructed by the left side of the street canyon (building 1, Figure 6-18).

In this case, the horn antenna is used at the TX ground station: in particular, the antenna is fixed to a horizontal mast pole which rotates during the measurement, in order to get a Power-Angle Profile at the TX on the Vertical plane, i.e. a Power-Elevation Profile (PEP). Results are shown in Figure 6-18, where the red curve corresponds to the low-altitude case (19 m), and blue curve to medium-altitude case. In the plots, the 0° angle to corresponds to the TX antenna pointed vertically towards the sky, and the angle increases clockwise, i.e. when the antenna rotates towards the building behind the ground station (Building 2), with 15° step.

Figure 6-16: Building #1 in Imola for roof to street (R2S) analysis

Figure 6-17: Front view of the same building #1 in Imola, Italy

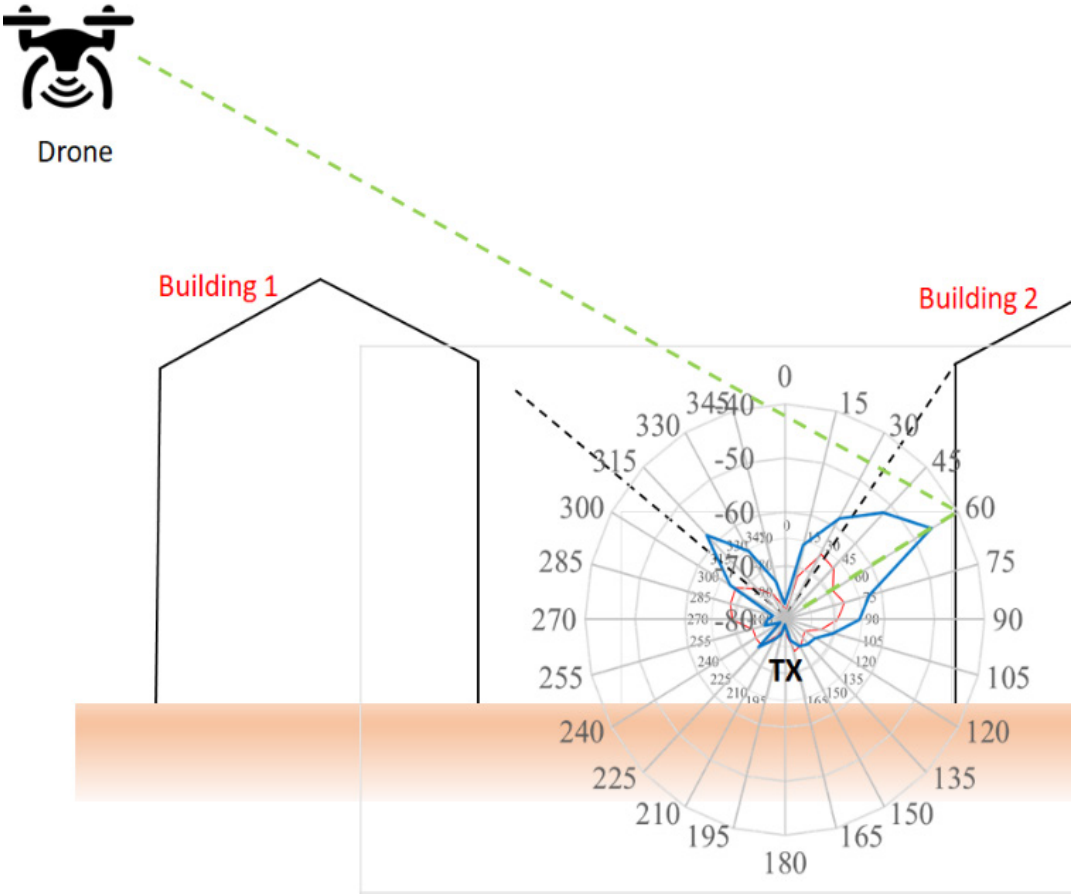

Figure 6-18: Power-Elevation Profiles at TX in the "Air-to-street" NLOS scenario, for 2 different drone altitudes: 19 m (red curve) and 50 m (blue curve) at 27 GHz, © 2021 IEEE

Looking at the blue curve, it is possible to clearly identify a dominant contribution at 60° departure angle: this contribution appears to be compatible with a specular reflection (green dashed line in Fig. 5) on the main façade of Building 2, i.e. the building behind the ground station. This contribution is about 10 dB stronger than the one provided by the minimum-length path, corresponding to a diffraction on the horizontal roof edge (315° departure angle in blue curve). Reflection/scattering on the building behind TX appears then to be one of the main mechanisms for the signal to propagate from the street-canyon to the air (and viceversa), in agreement with previous studies [81].

Looking at the red curve (19 m altitude), power-levels are on average 15 dB lower than in the previous case: this is due to less favourable conditions for the signal to propagate from the street canyon to the air. In such a case, the geometry is not compatible with specular reflections on the building walls surrounding TX: the PEP plot has two relative maxima with similar intensity, at 35° and 310° (black dashed lines in Fig. 5), which appears to be caused by diffraction on roof edges, or scattering from roof drainpipes.

Ambiguity unfortunately increases among the data set collected at 38 GHz, as it can be seen in Figure 6-19. As a matter of fact, minimum and maximum within the PEP differ than those seen at 27 GHz, while it was expected to see only an attenuated version. Furthermore, different acquisition dates – as a function of the post-lockdown period – increases the ambiguity and makes it difficult to trace back the possible error source or the search for a reasonable explanation.

Figure 6-19: Power-Elevation Profiles at TX in the "Air-to-street" NLOS scenario, for 2 different drone altitudes: 19 m (orange curve) and 50 m (blue curve) at 38 GHz. Drone position is not shown but is hovering above building #1 as in **Figure 6-18:** Power-Elevation Profiles at TX in the "Air-to-street" NLOS scenario, for 2 different drone altitudes: 19 m (red curve) and 50 m (blue curve) at 27 GHz, © 2021 IEEEFigure 6-18.

This means that there are further propagation mechanisms to be investigated and checked before drawing any conclusion on the R2S matter.

Unfortunately, the presented interesting results are not definitive, because only partial GIS information about the residential area were available at the time of the trials; in addition, very few runs with the UAV have been performed due to pandemic restriction. Nevertheless, this motivates to repeat the trials and cross-check the acquired data as part of the upcoming research activities.

CHAPTER 7. CONCLUSIONS AND FUTURE WORKS

The features of incoming UAV-Assisted wireless networks for 5G and beyond have been outlined and introduced *(CHAPTER 1.)*, motivating the need to have flexible and fast solutions in case of emergency or increased traffic demand.

The evaluation of UAV-Assisted network steams from the design and study of a patch antenna, in single and array configuration, highlighting the advantages and the drawbacks of this solution on board of UAVs, especially when the antenna involves innovative materials like a closed-cell rigid foam based on PMI chemistry *(CHAPTER 2.)*.

New frequency bands, especially those at 26 and 70 GHz, are currently under implementation, opening new challenges for the wireless community. Novel propagation and channel modelling issues were investigated by means of a Discrete Environment-Driven Ray Launching Algorithm, relaying on the flexibility that the tool can give to the network planner for Air-to-ground narrowband propagation. In addition to flexibility, we have investigated the performances of ray-launching in terms of computation time and the related speed-ups among different NVIDIA GPU cards used as test cases. We have demonstrated the benefit of GPU parallelization as a way to accelerate ray launching field computation. This shows the potential benefit of GPUs for electromagnetic simulations, and especially for deterministic field strength predictions. This also shows that NVIDIA gaming GTX cards should not be automatically dismissed, and they can be a good choice under specific simulation cases, instead of more expensive Tesla cards *(CHAPTER 3.)*.

Probability of LOS, path loss exponent, shadowing characteristics as well as the impact of different propagation mechanisms have been explored for several drone hovering altitudes, directive and non-directive antennas as well as transmitting frequencies, thus giving a full overview to the subject for three different urban scenarios. Narrowband analysis has proved that both path loss exponent and shadowing standard deviation reduces with both the UAV altitude and the on-board antenna aperture. Path loss exponents turn out to be remarkably greater than 2 to for flying heights up to 150m. Ray-launching simulations can easily provide insight into propagation mechanism and actual values for field prediction at ground level, like the power brought to the receivers by the direct path (when present) or indirect ones or even combinations of them. Diffraction appears as the leading propagation mechanism at lower frequencies, while scattering at higher frequencies for the larger aperture of the UAV antenna, whereas most of the power is likely to be conveyed through the direct path for greater directivity. Anyway, the intensity of the direct field hardly exceeds the 50%-60% of the total power, thus meaning multipath propagation is not negligible on the average *(CHAPTER 4.)*.

First application of ray launching simulations comes from study of UABs trajectory optimisation, where it was proposed a model obtained from a network having a priori knowledge of the REM in its service area to both outline UABSs trajectories and make efficient RRM; then achieved results were compared with a model from the literature of the A2G channel. Results show the presence of a difference between simulations with RL and statistical models, as expected. The gap can demonstrate the significance of having RL accuracy in a realistic scenario, where the use of resources changes based on how strong is the A2G link. In this way, it is possible to demonstrate in a realistic scenario the significance of having RL accuracy in terms of propagation evaluation, since the use of radio resources may vary depending on how strong is the A2G link. Still, if there is no database storage availability, the network performance given by statistical models might be satisfactory *(CHAPTER 5.)*.

As a second application, the research activity summarised in this dissertation ended with some preliminary experimental measurements, carried out with a real UAV in an urban

environment. Investigating the impact of the different electromagnetic interactions on the A2G channel through in field measurement is an overwhelming task, as UAVs could hardly carry the necessary heavy equipment like channel sounders and processing hardware, not to mention the logistics needed to set-up the measurement campaign for O2I and R2S propagation *(CHAPTER 6.)*.

Moving from the theoretical simulations, i.e. RL runs on a powerful workstation, to actual in-field measurements – or validation of the same data - proved to be quite challenging. It should be said that collecting measurements coming from the field has never been an easy task, regardless of the involved technology, but using an UAV in an urban environment, definitely raises the stakes and it needs to be carefully planned and constantly monitored. On top of this, it must be noted that this preliminary set of data have been collected - at different times and with multiple constraints - only during the few available time slots after the 2020 Italian national lockdown for COVID-19.

Unfortunately, not all the in-field measurements have been satisfactory so far while other data need to be further evaluated or post-processed to get further insights on the air to ground channel for next generation mobile systems, especially for 27 and 38 GHz. This might extend this research activity to future works where additional simulations, as well as optimised antenna arrays, might be investigated and validated by means of further in-field measurements. At the same time, GPU architectures are progressing and improving under the wave of Artificial Intelligence (AI) and Big Data (BD). This allows the use and the benchmark of even more powerful GPU card in the next future for enhanced RL applications.

APPENDIX

This section provides additional pictures to further detail and integrate the results provided in Chapter 4 for the three urban environments under evaluation [83]. In detail, each multipath contribution is plotted as a function of UAV altitude and transmitting frequency:

BOLOGNA

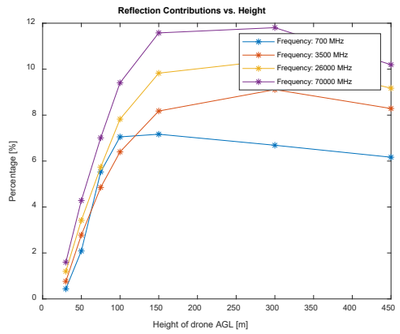

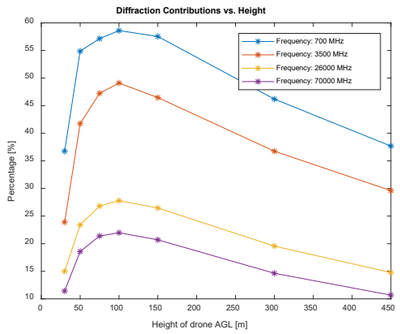

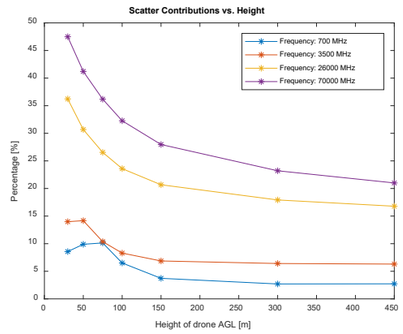

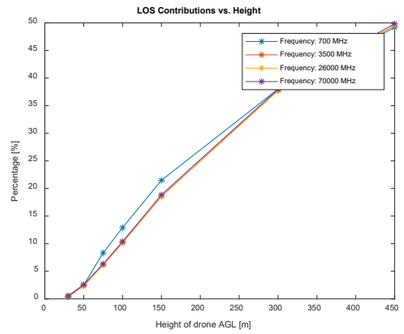

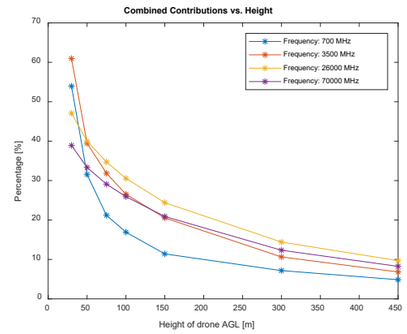

MUNICH

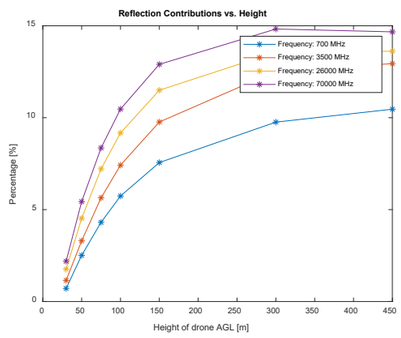

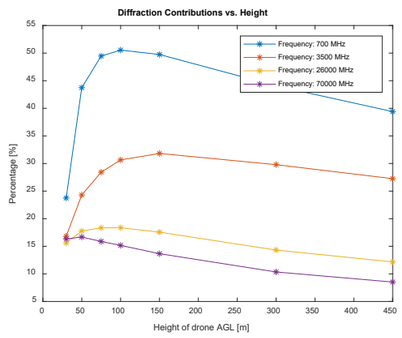

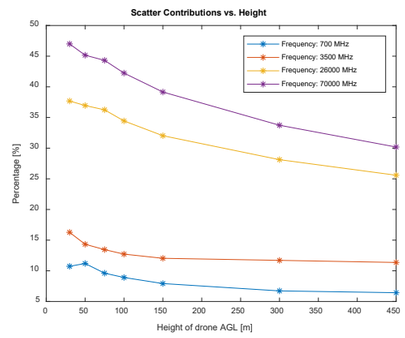

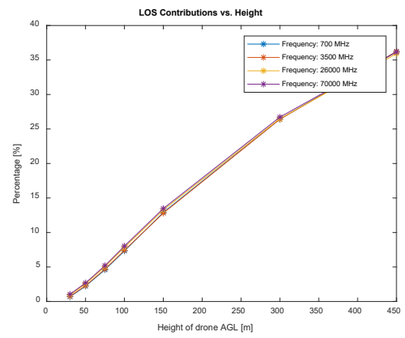

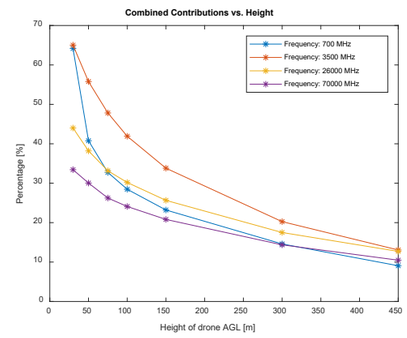

SAN FRANCISCO

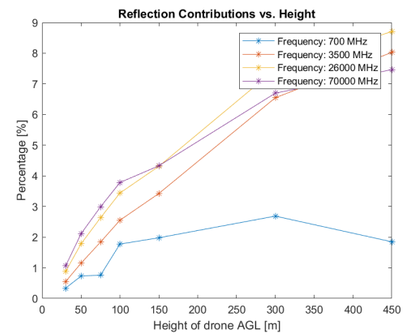

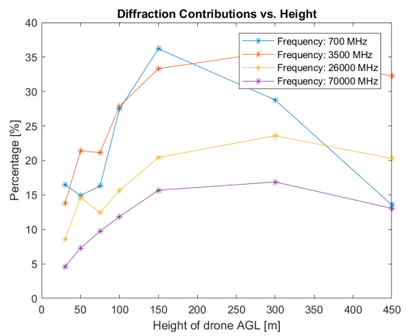

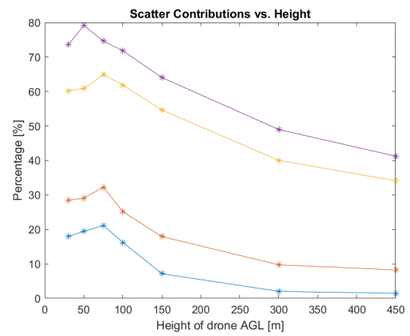

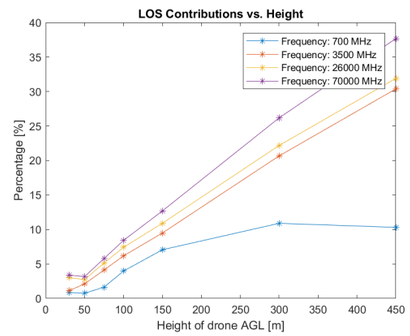

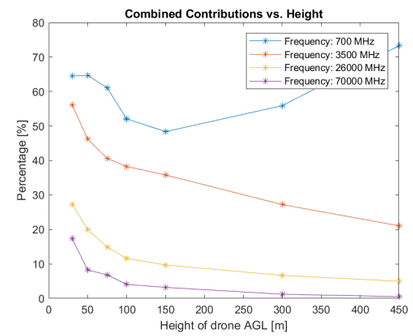

BIBLIOGRAPHY

[1] K. Namuduri, S. Chaumette, J. H. Kim, and J. P. Sterbenz, UAV Networks and Communications. Cambridge University Press, 2017.

[2] D. Joshi, "Commercial unmanned aerial vehicle (UAV) market analysis industry trends, companies and what you should know," Business Insider, 2017.

[3] S. D. Intelligence, "The global UAV payload market 2017–2027," 2017.

[4] Lucintel, "Commercial Drone Market Report: Trends, Forecast, and Competitive Analysis", ID#5003592, 2021

[5] K. P. Valavanis, G. J. Vachtsevanos "Handbook of Unmanned Aerial Vehicles", Dordrecht Springer ©2015 Springer, Cham.

[6] D. W. Matolak and R. Sun, "Unmanned Aircraft Systems: Air-Ground Channel Characterization for Future Applications", IEEE Vehic. Tech. Mag., vol.10, no. 2, June 2015, pp. 79–85.

[7] US Dept. of Transportation. "Unmanned aircraft system (UAS) service demand 2015-2035: literature review and projections of future usage", Technical Report, v. 1.0, DOT-VNTSC-DoD- 13-01, February 2014.

[8] Idries ; N. Mohamed ; I. Jawhar ; F. Mohamed ; J. Al-Jaroodi "Challenges of developing UAV applications: A project management view", 2015 International Conference on Industrial Engineering and Operations Management (IEOM), 3-5 March 2015, Dubai, United Arab Emirates

[9] Y. Li, L. Cai, "UAV-Assisted Dynamic Coverage in a Heterogeneous Cellular System", in IEEE Network, Volume: 31, Issue: 4, July-August 2017, pp. 56 – 61

[10] Z. Becvar, M. Vondra, P. Mach, J. Plachy, D. Gesbert, "Performance of Mobile Networks with UAVs: Can Flying Base Stations Substitute Ultra-Dense Small Cells?", in European Wireless 2017, 23th European Wireless Conference, Proceedings of, May 2017

[11] Y. Zeng, R. Zhang, and T. J. Lim, "Wireless communications with unmanned aerial vehicles: opportunities and challenges," IEEE Commun. Mag., vol. 54, no. 5, pp. 36–42, 2016.

[12] S. Chandrasekharan, K. Gomez, A. Al-Hourani, S. Kandeepan, T. Rasheed, L. Goratti, L. Reynaud, D. Grace, I. Bucaille, T. Wirth, and S. Allsopp, “Designing and implementing future aerial communication networks,” IEEE Commun. Mag., vol. 54, no. 5, pp. 26–34, May 2016.

[13] Z. Xiao, P. Xia, and X. Xia, “Enabling UAV cellular with millimeterwave communication: potentials and approaches,” IEEE Commun. Mag., vol. 54, no. 5, pp. 66–73, May 2016.

[14] K. Gomez, A. Hourani, L. Goratti, R. Riggio, S. Kandeepan, and I. Bucaille, “Capacity evaluation of Aerial LTE base-stations for public safety communications,” in 2015 European Conference on Networks and Communications (EuCNC), 2015, pp. 133–138.

[15] T. Long, M. Ozger, O. Cetinkaya and O. B. Akan, "Energy Neutral Internet of Drones," in IEEE Communications Magazine, vol. 56, no. 1, pp. 22-28, Jan. 2018.

[16] “Roadmap for the integration of civil remotely-piloted aircraft systems into the European aviation system,” EUROCONTROL, Brussels, Belgium, Tech. Rep., 2013. [Online]. Available: https://publicintelligence.net/eu-rpa-roadmap/

[17] Ranjan, B. Panigrahi, H. K. Rath, P. Misra, A. Simha, and H. B. Sahu, “A study on pathloss model for UAV based urban disaster and emergency communication systems,” in 2018 Twenty Fourth National Conference on Communications (NCC), Feb 2018, pp. 1–6.

[18] Z. Yang, L. Zhou, G. Zhao, and S. Zhou, “Channel model in the urban environment for unmanned aerial vehicle communications,” in 12th European Conference on Antennas and Propagation (EuCAP 2018), April 2018, pp. 1–5.

[19] L. Zhou, Z. Yang, G. Zhao, S. Zhou, and C. Wang, “Propagation characteristics of air-to-air channels in urban environments,” in 2018 IEEE Global Communications Conference (GLOBECOM), Dec 2018, pp. 1–6.

[20] [17] J. Zeleny, M. Kvicera, P. Valtr, F. Perez-Fontan, and P. Pechac, “State propagation channel model for 2 GHz UAV links in cluttered environment,” in 12th European Conference on Antennas and Propagation (EuCAP 2018), April 2018, pp. 1–5.

[21] Y. Shi, R. Enami, J. Wensowitch, and J. Camp, ``Measurement-based characterization of LOS and NLOS drone-to-ground channels," in Proc. IEEE Wireless Commun. Net. Conf. (WCNC), Barcelona, Spain, Apr. 2018, pp. 1_6.

[22] R. Amorim, P. Mogensen, T. Sorensen, I. Z. Kovacs, and J. Wigard, ``Pathloss measurements and modelling for UAVs connected to cellular networks," in Proc. IEEE 85th Veh. Tech. Conf. (VTC Spring), Sydney, NSW, Australia, Jun. 2017, pp. 1_6.

[23] E. Zöchmann, K. Guan and M. Rupp, "Two-ray models in mmWave communications," 2017 IEEE 18th International Workshop on Signal Processing Advances in Wireless Communications (SPAWC), Sapporo, 2017, pp. 1-5..

[24] J. Yu, Y. Zeng, R. Zhang, “UAV-Aided Offloading for Cellular Hotspot”, IEEE Trans. on Wirel. Comm., vol. 17, No. 6, June 2018, pp. 3988-4001;

[25] E. Damosso, L. M. Correia, “COST Action 231: Digital Mobile Radio Towards Future Generation Systems: Final Report”, European Commission, 1999

[26] J. Walfish, H L. Bertoni, “A Theoretical Model of UHF Propagation in Urban Environments”, IEEE Trans. Antennas and Propagation, vol. AP-38, 1988.

[27] M. Hata, “Empirical formula for propagation loss in land mobile radio services”, IEEE Trans. Antennas and Propag., vol. 29, no. 3, pp. 317- 325, 1980.

[28] N. Goddemeier, K. Daniel, and C. Wietfeld, “Coverage evaluation of wireless networks for unmanned aerial systems,” in GLOBECOM Workshops (GC Wkshps), 2010 IEEE. IEEE, 2010, pp. 1760–1765.

[29] Al-Hourani, S. Kandeepan, and A. Jamalipour, “Modeling air-to ground path loss for low altitude platforms in urban environments,” in Global Communications Conference (GLOBECOM), 2014 IEEE. IEEE, 2014, pp. 2898–2904.

[30] W. Khawaja, O. Ozdemir, and I. Guvenc, “UAV air-to-ground channel characterization for mmWave systems,” in 2017 IEEE 86th Vehicular Technology Conference (VTC-Fall), Sep. 2017, pp. 1–5.

[31] J. S. Lu, E. M. Vitucci, V. Degli-Esposti, Franco Fuschini, Marina Barbiroli, Jerome A. Blaha, Henry L. Bertoni, “A Discrete Environment-Driven GPU-Based Ray Launching Algorithm”, IEEE Transactions on Antennas and Propagation Year: 2019, Volume: 67, Issue: 2, Pages: 1180 – 1192

[32] Q. Feng, J. McGeehan, E. K. Tameh, and A. R. Nix, “Path loss models for air-to-ground radio channels in urban environments,” in Vehicular Technology Conference, 2006. VTC 2006-Spring. IEEE 63rd, vol. 6. IEEE, 2006, pp. 2901–2905.

[33] M. J Arpaio, E.M. Vitucci, M. Barbiroli, V. Degli-Esposti, D. Masotti, F. Fuschini, “Narrowband Characteristics of Air-to-Ground Propagation for UAV Assisted Networks in Urban Environments By Means of Fast Ray-Launching Simulations”, 2020 IEEE 91st Vehicular Technology Conference (VTC2020-Spring), Antwerp, Belgium, 25-28 May 2020.

[34] M J. Arpaio; E M. Vitucci; M Barbiroli; V. Degli Esposti; D Masotti; F Fuschini, “Ray-Launching Narrowband Analysis of UAV-to-Ground Propagation in Urban Environment”, in: 2019 International Symposium on Antennas and Propagation, ISAP 2019 - Proceedings, Institute of Electrical and Electronics Engineers Inc., 2019, pp. 1 – 3

[35] Z. Yun and M. F. Iskander, "Ray Tracing for Radio Propagation Modeling: Principles and Applications," in IEEE Access, vol. 3, pp. 1089-1100, 2015.

[36] P. Pigin, “Emerging mobile WiMax antenna technologies”, IET Communication Engineer, October/ November 2006.

[37] Maximilian James Arpaio, Franco Fuschini, Enrico Maria Vitucci, Vittorio Degli-Esposti, Marina Barbiroli, Diego Masotti “Lightweight Microstrip Patch Array for Broadband UAV Applications over 5G networks”, Proceedings of the 2019 Conference on Microwave Techniques (COMITE), Pardubice, Czech Republic, IEEE, 2019, pp. 1 – 5.

[38] S. Mignardi, R. Verdone, “On the Performance Improvement of a Cellular Network Supported by an Unmanned Aerial Base Station”, 2017 29th International Teletraffic Congress (ITC 29), Year: 2017

[39] H. Sajjad, W.T. Sethi, K. Zeb, A. Mairaj, “Microstrip patch antenna array at 3.8 GHz for WiMax and UAV applications”, 2014 International Workshop on Antenna Technology: Small Antennas, Novel EM Structures and Materials, and Applications (iWAT)

[40] Wen-Shan Chen, Yung-Chi Lin, “Design of 2×2 Microstrip Patch Array Antenna for 5G C-Band Access Point Applications”, 2018 IEEE International Workshop on Electromagnetics: Applications and Student Innovation Competition (iWEM), 2018

[41] S. Dweik, S. Deif, W. Sadeh, O. A. Rawashdeh, D. N. Aloi, M. S. Sharawi, “A planar antenna array with integrated feed network for UAV applications”, The 8th European Conference on Antennas and Propagation (EuCAP 2014), 2014, Pages: 1855 – 1858

[42] K. Mousskhani, A. Ghorbani, “A modified broadband transmission line model for rectangular patch antennas”, 2008 International Conference on Microwave and Millimeter Wave Technology, 2008, Volume: 3, Pages: 1041 – 1043

[43] M. S. Sharawi, D. N. Aloi, O. A. Rawashdeh, “Design and Implementation of Embedded Printed Antenna Arrays in Small UAV Wing Structures”, IEEE Transactions on Antennas and Propagation, 2010, Volume: 58, Issue: 8, Pages: 2531 - 2538

[44] Z. Liu, Y. Zhang, Z. Qian, Z. P. Han and W. Ni, "A Novel Broad Beamwidth Conformal Antenna on Unmanned Aerial Vehicle," in IEEE Antennas and Wireless Propagation Letters, vol. 11, pp. 196-199, 2012.

[45] Z. Yun, M. F. Iskander,“ Ray Tracing for Radio Propagation Modelling: Principles and Applications ”, IEEE Access, Volume 3, pp 1089 – 1100, July 2015.

[46] N. Kinayman,” Parallel Programming with GPUs: Parallel Programming Using Graphics Processing Units with Numerical Examples for Microwave Engineering”, IEEE Microwave Magazine, 102 – 115, Volume 14, Issue 4 , June 2013.

[47] J. D. Owens, D. Luebke, N. Govindaraju, M. Harris, J. Kruger, A. E. Lefohn, T. J. Purcell, "A survey of general-purpose computation on graphics hardware", Proc. Eur. Assoc. Comput. Graph., pp. 21-51, Aug. 2005.

[48] Hidic, D. Zubanovic, A. Hajdarevic, A. Huseinovic, N. Nosovic, “Attempt of unbiased comparison of GPU and CPU performance in common scientific computing”, 2012 IX International Symposium on Telecommunications (BIHTEL), Sarajevo, Bosnia & Herzegovina, 25-27 Oct. 2012.

[49] S. W. Keckler, W.J. Dally, B. Khailany, M. Garland, D. Glasco, “GPUs and the future of parallel computing”, IEEE Micro Volume 31, Issue: 5, Sept.-Oct. 2011.

[50] V. Degli-Esposti, F. Fuschini, E.M. Vitucci, G. Falciasecca, "Measurement and modelling of scattering from buildings," in IEEE Transactions on Antennas and Propagation, vol. 55, no. 1, pp. 143-153, Jan 2007.

[51] E. M. Vitucci, V. Degli-Esposti, F. Fuschini, J. S. Lu, M. Barbiroli, J. N. Wu, M. Zoli, J. J. Zhu, and H. L. Bertoni, “Ray Tracing RF Field Prediction: An Unforgiving Validation”, International Journal of Antennas and Propagation, Hindawi, Vol. 2015, pp. 1 – 11, Aug. 2015.

[52] V. Degli-Esposti, V.-M. Kolmonen, E. M. Vitucci, F. Fuschini, P. Vainikainen, “Analysis and ray tracing modelling of co- and cross-polarization radio propagation in urban environment,” Proceedins of 2nd European Conference on Antennas and Propagation (EuCAP 2007), Edinburgh, UK, 11-16 November 2007.

[53] M J. Arpaio; E M. Vitucci, F Fuschini, “A Comparative Study of the Computation Efficiency of a GPU-Based Ray Launching Algorithm for UAV-Assisted Wireless Communications”, Applied Computational Electromagnetics Society (ACES) Journal, No.12, December 2020, Volume 35, pp. 1456 - 1462.

[54] NVIDIA Corporation Whitepaper, “NVIDIA’s Next Generation, CUDA Compute Architecture: Kepler GK110/210 Family”, 2012.

[55] NVIDIA Corporation Whitepaper, “NVIDIA’s Next Generation, CUDA Compute Architecture: Pascal GP100 Family”, 2017.

[56] NVIDIA Corporation Whitepaper, “NVIDIA’s NVIDIA Turing GPU Architecture: Graphics Reinvented”, 2019.

[57] The MathWorks, Inc., “Matlab 2017B User Guide: on-line help”, referenced resources, 2016.

[58] NVIDIA Corporation, Developer’s zone, “NVIDIA CUDA Toolkit 10.2.89: CUDA Toolkit Documentation”, November 2019.

[59] N. Matloff, “Parallel Computing for Data Science: With Examples in R, C++ and CUDA”, June 4, 2015 Chapman and Hall/CRC Pub., June 2015.

[60] Reaño, F. Silla, “Performance Evaluation of the NVIDIA Pascal GPU Architecture: Early Experiences”, 2016 IEEE 18th International Conference on High Performance Computing and Communications, Sydney, Australia, 12-14 Dec. 2016.

[61] Z. Dai; R. J. Watson, “Accelerating a ray launching model using GPU with CUDA”, 12th European Conference on Antennas and Propagation (EuCAP 2018), London, UK, 9-13 April 2018.

[62] M. Ujaldon, “Using GPUs for Accelerating Electromagnetic Simulations”,ACES Journal Paper, Number 4, Volume 25, year 2010.

[63] T. Rappaport, “Wireless Communications: Principles and Practice”, 2nd ed. Prentice Hall PTR, 2002.

[64] J.D. Parsons, “The Mobile Radio Propagation Channel”, Wiley & Sons 2000.

[65] R. Amorim, H. Nguyen, P. Mogensen, I. Z. Kovács, J. Wigard and T. B. Sørensen, "Radio Channel Modeling for UAV Communication Over Cellular Networks," in IEEE Wireless Communications Letters, vol. 6, no. 4, pp. 514-517, Aug. 2017.

[66] W. Khawaja, I. Guvenc, D. W. Matolak, U. Fiebig and N. Schneckenburger, "A Survey of Air-to-Ground Propagation Channel Modeling for Unmanned Aerial Vehicles," in IEEE Communications Surveys & Tutorials, vol. 21, no. 3, pp. 2361-2391, 2019.

[67] CISCO, C.V. Forecast, “Cisco visual networking index: Global mobile data traffic forecast update 2016-2021”, (2017).

[68] S. Mignardi, C. Buratti, R. Verdone, “On the impact of radio channel over rem-aware UAV-aided mobile networks”, 22nd International ITG Workshop on Smart Antennas, 2018, pp. 1–6.

[69] Al-Hourani, S. Kandeepan, S. Lardner, “Optimal lap altitude for maximum coverage”, IEEE Wireless Communications Letters 3 (6) (2014) 569–572.

[70] Denkovski ; V. Atanasovski ; L. Gavrilovska ; J. Riihijärvi ; P. Mähönen, “Reliability of a radio environment Map: Case of spatial interpolation techniques”, 2012 7th International ICST Conference on Cognitive Radio Oriented Wireless Networks and Communications (CROWNCOM), Stockholm, 2012, pp. 248-253.

[71] S. Mignardi, R. Verdone, “Joint path and radio resource management for UAVs supporting mobile radio networks”, 2018 17th Annual Mediterranean Ad Hoc Networking Workshop (MedHoc-Net), 2018, pp. 1–7.

[72] Silvia Mignardi, Maximilian James Arpaio, Chiara Buratti, Enrico Maria Vitucci, Franco Fuschini, Roberto Verdone, “Performance Evaluation of UAV-Aided Mobile Networks by Means of Ray Launching Generated REMs”, International Telecommunication Networks and Application Conference (ITNAC), Melbourne, Australia, 25-27 November 2020.

[73] W. Khawaja, O. Ozdemir, F. Erden, I. Guvenc and D. W. Matolak, "Ultra-Wideband Air-to-Ground Propagation Channel Characterization in an Open Area," in IEEE Transactions on Aerospace and Electronic Systems (early access), 2020.

[74] W. Khawaja, O. Ozdemir, F. Erden, I. Guvenc and D. W. Matolak, "UWB Air-to-Ground Propagation Channel Measurements and Modeling Using UAVs," 2019 IEEE Aerospace Conference, Big Sky, MT, USA, , pp. 1-10,m 2019.

[75] J. Zeleny, F. Pérez-Fontàn and P. Pechac, "Initial Results from a measurement campaign for low elevation angle links in different environments," 2015 9th European Conference on Antennas and Propagation (EuCAP), Lisbon, pp. 1-4. 2015

[76] M. Bucur, T. Sorensen, R. Amorim, M. Lopez, I. Z. Kovacs and P. Mogensen, "Validation of Large-Scale Propagation Characteristics for UAVs within Urban Environment," 2019 IEEE 90th Vehicular Technology Conference (VTC2019-Fall), Honolulu, HI, USA, pp. 1-6, 2019.

[77] M. Lopez, T. B. Sorensen, P. Mogensen, J. Wigard and I. Z. Kovacs, "Shadow Fading Spatial Correlation Analysis for Aerial Vehicles: Ray Tracing vs. Measurements," 2019 IEEE 90th Vehicular Technology Conference (VTC2019-Fall), Honolulu, HI, USA, pp. 1-5, 2019.

[78] https://spectrumcompact.com/

[79] https://spectrumcompact.com/sg-compact/

[80] http://qgroundcontrol.com/

[81] V. Degli-Esposti, F. Fuschini, D. Guiducci, “A study on roof-to-street propagation”, in Proc. Of International Conference on Electromagnetics in Advanced Applications (ICEAA 2003), Turin, Italy, pp. 45-47, 2003.

[82] R. Rudd, X. Meng, V. Ocheri, D. Wu and M. Nekovee, "Joint statistics of urban clutter loss and building entry loss at 3.5 GHz and 27 GHz - from measurement to modelling," 2020 14th European Conference on Antennas and Propagation (EuCAP), Copenhagen, Denmark, 2020, pp. 1-5.

[83] Arpaio, Maximilian James; Vitucci, Enrico M.; Barbiroli, Marina; Degli-Esposti, Vittorio; Masotti, Diego; Fuschini, Franco, “A Multi-Frequency Investigation of Air-To-Ground Urban Propagation Using a GPU-based Ray Launching Algorithm”, 2021 IEEE ACCESS Journal Article

LIST OF PUBLICATIONS

This PhD thesis reflects and summarises the research activity carried out in the last 3 years. The content used for this dissertation, including most of the figures and tables, is based on the publications listed below issued in the frame of my research activity but for which the relative publisher reserves now the copyright on the content.

CONFERENCE PROCEEDINGS

Maximilian James **Arpaio**, Franco Fuschini, Enrico Maria Vitucci, Vittorio Degli-Esposti, Marina Barbiroli, Diego Masotti "*Lightweight Microstrip Patch Array for Broadband UAV Applications over 5G networks*", Proceedings of the 2019 Conference on Microwave Techniques (COMITE), Pardubice, Czech Republic, IEEE, 2019, pp. 1 – 5. © 2019 IEEE

Maximilian James **Arpaio**, Enrico Maria Vitucci, Marina Barbiroli, Vittorio Degli-Esposti, Diego Masotti, Franco Fuschini "*Ray-Launching Narrowband Analysis of UAV-to-Ground Propagation in Urban Environment*", Proceedings of the 2019 International Symposium on Antennas and Propagation (ISAP), Xi'An, P.R China, IEEE, 2019, pp. 1 – 4. © 2019 IEEE

Arpaio, Maximilian James; Vitucci, Enrico M.; Barbiroli, Marina; Degli-Esposti, Vittorio; Masotti, Diego; Fuschini, Franco, "*Narrowband Characteristics of Air-to-Ground Propagation for UAV Assisted Networks in Urban Environments By Means of Fast Ray-Launching Simulations*", Proceedings of the 2020 IEEE 91st Vehicular Technology Conference (VTC2020-Spring), IEEE, 2020, pp. 1 – 5. © 2020 IEEE

Silvia Mignardi, Maximilian James **Arpaio**, Chiara Buratti, Enrico Maria Vitucci, Franco Fuschini, Roberto Verdone, "*Performance Evaluation of UAV-Aided Mobile Networks by Means of Ray Launching Generated REMs*", International Telecommunication Networks and Application Conference (ITNAC), Melbourne, Australia, 25-27 November 2020. © 2020 IEEE

E.M. Vitucci, V. Semkin, M. J. **Arpaio**, M. Barbiroli, F.Fuschini, C. Oestges, V. Degli-Esposti, "*Experimental Characterization of Air-to-ground Propagation Channel at mm-Wave Frequencies in Dense Urban Environment*" European Conference on Antenna and Propagation (EuCap 2021) [waiting for publication]. © 2021 IEEE. © 2021 IEEE

JOURNAL ARTICLES

Arpaio, Maximilian James; Vitucci, Enrico M.; Barbiroli, Marina; Degli-Esposti, Vittorio; Masotti, Diego; Fuschini, Franco, "*A Multi-Frequency Investigation of Air-To-Ground Urban Propagation Using a GPU-based Ray Launching Algorithm*", IEEE ACCESS Journal Article doi: 10.1109/ACCESS.2021.3070832. © 2021 IEEE

Arpaio, Maximilian James; Vitucci, Enrico M.; Fuschini, Franco, "*A Comparative Study of the Computation Efficiency of a GPU-Based Ray Launching Algorithm for UAV-Assisted Wireless Communications*", ACES Journal Article vol. 35, no. 12, pp. 1456-1462, Dec. 2020 © 2020 ACES SOCIETY

CURRICULUM VITAE

Maximilian James Arpaio received the Master degree in Telecommunications Engineering from the University of Parma in 2005 with an experimental thesis on the design of an antenna for Digital Audio Broadcasting (DAB) applications. In 2007 he attended a specialization course in Wind Engineering and aerodynamics at the Department of Aerospace Engineering of the Polytechnic of Milan, during which he studied the wind load of blunt bodies applied to radio and television transmitting antenna systems. He received his Post graduate Master in Project Management (MPM) from the Faculty of Economics of the University of Verona in 2012, presenting a thesis on communication in multicultural projects. After nearly 15 years of industrial experience in the field of telecommunications and project management, spanning from antenna for radio-television broadcasting to air-navigation systems and airport solution, with a strong background on international projects, in 2017 he decided to join the University of Bologna, Italy as a PhD student.

His current research interests span from the electromagnetic design of antenna solutions to the radio channel modelling of next generation mobile systems (5G) for UAVs assisted wireless networks. He has been collaborating for many years with various Italian universities by promoting technical seminars and scientific collaborations.

STUDIORUM
LIBERTAS